Stem Cell-Based Modeling of Early Human Neural Development

by

Xufeng Xue

A dissertation submitted in partial fulfillment
of the requirements for the degree of
Doctor of Philosophy
(Mechanical Engineering)
at the University of Michigan
2020

Doctoral Committee:

Associate Professor Jianping Fu, Chair
Associate Professor Benjamin Allen
Associate Professor Allen Liu
Professor K. Sue O'Shea

Xufeng Xue

xufeng@umich.edu

ORCID: 0000-0002-9379-8589

Acknowledgements

I would like to first express my deepest gratitude to my advisor Prof. Jianping Fu for his mentoring and guidance during my entire PhD study. I am always inspired by Prof. Fu's passion and rigorous attitude for research, and this would continue to motivate me as an independent researcher in the future. I thank him for his hands-off advising style and continuous support to my work, which allows me to explore different research areas and develop my creativity independently. I truly appreciate his genuine care towards my career path and helping me building connections.

Besides my advisor, I am truly grateful for all my mentors and collaborators. I would like to thank the rest of my thesis committee, Prof. Allen Liu, Prof. K. Sue O'Shea, and Prof. Benjamin Allen for their interest in my work, taking time to meet with me, providing valuable feedback and insightful suggestions on my research. I would also like to thank my collaborators Prof. Cheri Deng, Dr. Xiaowei Huang, Dr. Tugba Topal, Dr. Zhenzhen Fan, Dr. Shiying Liu, Eric Hobson and Chun-Yen Sung for our memorable and meaningful work together. It's amazing to have so many wonderful collaborators and this really made my research life much more pleasant and enjoyable.

I also sincerely thank my fellow lab mates: Dr. Koh Meng Aw Yong, Dr. Zeta Yu, Dr. Yubing Sun, Dr. Yue Shao, Dr. Shinuo Weng, Dr. Yi Zheng, Dr. Zida Li, Xiang Li, Jianming Sang, Yuanyuan Zheng, Feng Lin, Sajedeh Esfahani, Agnes Resto Irizarry, Sicong Wang, Samuel Byung-Deuk Lee, I would like to thank them for helping me to get started in this lab,

sharing knowledge and skills with me, and providing generous help and insightful suggestions to my research. I would also thank Prof. Allen Liu, Prof. Katsuo Kurabayashi and lab members of them: Kenneth Kwun Yin Ho, Dr. Shue Wang, Yujing Song and Meng-Ting Chung, et al. for sharing the equipment, knowledge and expertise with me.

In the end, I would like to thank my parents and wife for their endless love, unconditional support. I thank my parents for their trust to let me to make my own life decisions and their encouragement to help me overcome difficult times. I hope they live happy and healthy and I hope I could spend more with them in the future. I thank my wife for taking care my life. I couldn't achieve this dissertation without your love and support.

Table of Contents

List of Figures

List of Tables

List of Appendices

Abstract

Neurulation is a key embryonic developmental process that gives rise to the formation of the neural tube (NT), the precursor structure that eventually develops into the central nervous system (CNS). Understanding the molecular mechanisms and morphogenetic events underlying human neurulation is important for the prevention and treatment of neural tube defects (NTDs) and neurodevelopmental disorders. However, animal models are limited in revealing many fundamental aspects of neurulation that are unique to human CNS development. Furthermore, the technical difficulty and ethical constraint in accessing neurulation-stage human embryos have significantly limited experimental investigations of early human CNS development.

In this dissertation, I leveraged the developmental potential and self-organizing property of human pluripotent stem cells (hPSCs) in conjunction with 2D and 3D bioengineering tools to achieve the development of spatially patterned multicellular tissues that mimic certain aspects of the early human neurulation, including neural induction and dorsal-ventral (DV) patterning of NT.

In the first section, I report a micropatterned hPSC-based neuroectoderm model, wherein pre-patterned geometrical confinement induces emergent patterning of neuroepithelial (NE) and neural plate border (NPB) cells, mimicking neuroectoderm patterning during early neurulation. My data support the hypothesis that in this hPS cell-based neuroectoderm patterning model, two tissue-scale morphogenetic signals, cell shape and cytoskeletal contractile force, instruct NE /

NPB patterning *via* BMP-SMAD signaling. This work provides evidence of tissue mechanics-guided neuroectoderm patterning and establishes a tractable model to study signaling crosstalk involving both biophysical and biochemical determinants in neuroectoderm patterning.

In the second section, I report a human NT development model, in which NT-like tissues, termed NE cysts, are generated in a bioengineered neurogenic environment through self-organization of hPSCs. DV patterning of NE cysts is achieved using retinoic acid and/or Sonic Hedgehog, featuring sequential emergence of the ventral floor plate, p3 and pMN domains in discrete, adjacent regions and dorsal territory that is progressively restricted to the opposite dorsal pole.

These hPS cell-based in vitro models are important alternatives to animal models to study the self-organizing principles involved in autonomous patterning during human neurulation. These models could also be leveraged for developing high-throughput toxicological studies and drug screening platforms for prevention and treatment of neural tube defects.

Chapter 1

Introduction

Neurulation is a key embryonic developmental process that gives rise to neural tube (NT), the precursor structure that eventually develops into the central nervous system (CNS). Neurulation occurs soon after the gastrulation of the embryo, during which the epiblast resolves into a trilaminar germ disc structure containing the ectoderm, mesoderm and endoderm [1]. Neurulation is initiated by a neural induction process, during which the ectoderm is specified into a spatially patterned multicellular tissue containing the neural plate (NP) and the non-neural ectoderm (NNE, prospective epidermis) separated by the neural plate border [2, 3]. After neural induction, the NP folds towards the dorsal side of the embryo and fuses to form the tubular NT, enclosing a fluid-filled lumen (**Figure 1-1**) [4]. The development of the NT continues with the differentiation of distinct classes of neuronal progenitor cells located at defined positions within the NT along both the anterior-posterior (AP) and dorsal-ventral (DV) axes. Specification of neuronal fates in the NT is directed by secreted inductive factors (*i.e.*, morphogens) released from surrounding embryonic tissues. These inductive signals are transduced through intracellular signaling events and genetic networks to activate distinct transcriptional factors that restrict the progressive development and specification of progenitor cells in the NT towards different classes of neuronal and glial subtypes [5-7]. Disruption of NT development leads to NT

defects (NTDs), one of the most common birth defects, affecting over 300,000 births each year worldwide [8]. Many neurodevelopmental disorders such as autism spectrum disorder and Down's syndromes are also due to dysregulation of early CNS development [9, 10]. Understanding the molecular mechanisms and morphogenetic events underlying human neurulation is thus important for the prevention of NTDs and other neurodevelopmental disorders. Here I briefly summarize our current understanding of the developmental principles underlying the early neural development, with a focus on neural induction, NPB specification and DV patterning of NT.

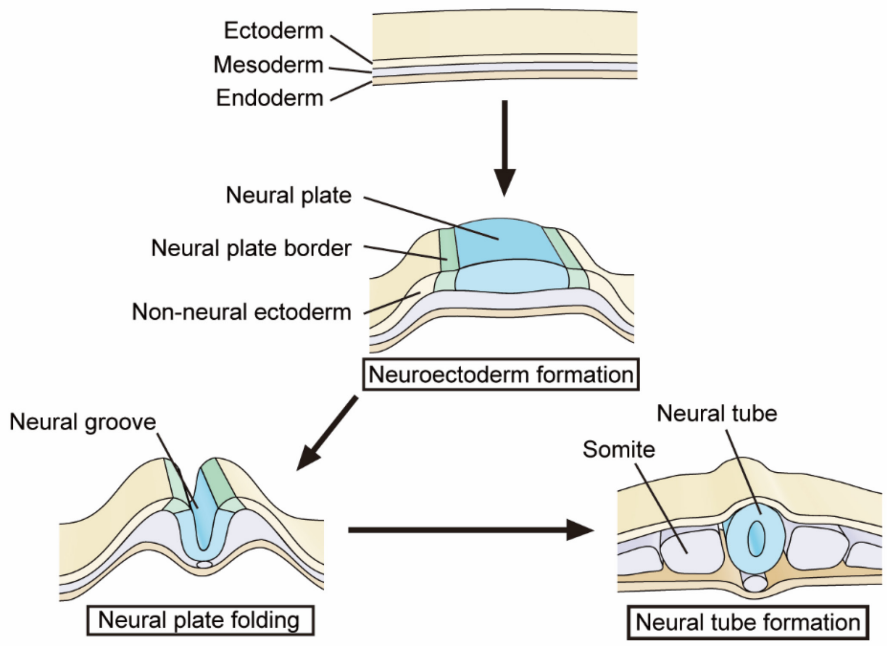

Figure 1-1 Schematics of neurulation in vivo. After gastrulation, ectoderm becomes specified to give rise to non-neural ectoderm (skin), neural plate border and neural plate. This process is called neuroectoderm formation or neural induction. Then the neural plate bends towards the dorsal side of the embryo and forms neural groove. The closure of neural groove forms a tubular structure: neural tube.

1.1 Current understanding of neurulation

1.1.1 Neural induction

Neural induction is the first step of the development of nervous system, during which ectoderm cells formed spatially patterned neuroepithelial (NE) cells, NPB cells and epidermis (skin). The first work elucidating the mechanism of neural induction was conducted by Spemann and Mangold in 1920s [11]. In this famous experiment, tissue from dorsal lip of the blastopore in amphibian embryos were transplanted to another gastrula stage amphibian embryo. Interestingly, the recipient embryo developed a secondary nervous system surrounding the transplanted cells. This study suggested that dorsal lip (later called organizer) provides inductive signals that specify neighbor ectoderm cells into neural fate. The analogous structures that are capable to induce neural development of adjacent ectoderm were later found in other species including chick and mouse [12, 13]. The neural inductive effect of organizer was further confirmed by in vitro culture of embryonic tissue. When animal cap (ectoderm in *Xenopus*) in blastula stage *Xenopus* embryos was isolated and cultured by itself, it developed into epidermis tissue. But when cultured together with dorsal mesoderm tissue that includes organizer, animal cap explants developed into neural tissue [14, 15].

In 1990s, several studies in *Xenopus* have reveal the molecular nature of the inductive signals emitted from organizer region. Although intact animal cap explants from blastula stage embryos gave rise to epidermis when cultured in vitro, overexpression of the negative form of the receptors that bind activin or BMP inhibited epidermal differentiation and promoted neural differentiation [16-19]. Dissociation of animal cap explants into single cells led to neural tissue even in the absence of organizer cells, suggesting that signaling between ectoderm cells may inhibit neural differentiation [20]. Neural differentiation of dissociated animal cap was inhibited if the dissociated cells were cultured with BMP4 protein or if the effectors of BMP signaling such as Msx1, Smad1 or Smad5 were ectopically expressed in the embryos [17, 21-23].

Moreover, in gastrula stage *Xenopus* embryos, *BMP* mRNA was found to be repressed in neural plate but expressed in epidermis [21, 24]. These experiments suggest that BMP inhibitors secreted from organizer region induced neural differentiation of ectoderm. Consistently, several BMP antagonists including Noggin, Chordin and Follistatin were found to be expressed in *Xenopus* organizer cells [25-27]. And these proteins inhibited the epidermal differentiation and induced neural differentiation of intact animal cap explants [25-27]. These studies further support that neural induction was caused by the inhibition of BMP signaling. Collectively, all these results led to the finding of "default model" of neural induction, which proposes that ectodermal cells have a default tendency to differentiate into neural cells and BMP signaling could inhibit neural differentiation and induce epidermal differentiation. In amphibian embryos, ectodermal cells in the prospective neural plate region developed into neural tissue at gastrula stage in response to BMP antagonists produced by organizer, while high BMP signaling in prospective epidermal regions induced the cells to differentiate into epidermis.

As in amphibians, similar grafting experiments have identified that chick and mouse node as the neural inducer [12, 13]. However, studies on chick and mouse have challenged the default model and uncovered new signaling pathway including FGF and WNT signaling in regulating neural induction. It is found that node is not required in neural induction, as a neural plate still formed when node at gastrula stage was ablated in chick and mouse embryo [28, 29]. This suggest that neural induction may be caused by other mechanism besides signals emitted from the node. In chick, although BMP signaling was inhibited in neural plate, downregulation of p-Smad1, a downstream effector of BMP signaling, occurs later than the expression of neural plate markers SOX2 and SOX3, indicating BMP signaling is not required for inducing neural cells but rather maintaining the neural fate [30-32].

FGF signaling. It's now generally accepted that FGF signaling is required at blastula stage for neural induction in amphibian and chick embryos [33-39]. In chick embryo, *fgf3* mRNA is expressed in medial epiblast cells (prospective neuroectoderm) at blastula stage. Inhibition of FGF signaling led to upregulation of BMP mRNA expression in medial epiblast, and the cells differentiated into epidermis instead of neural cells [39]. FGF signaling could also affect the transcriptional activity of BMP signaling. In particular, FGF signaling could phosphorylate Smad1 in the linker region and inhibit Smad1 transcription activity [40]. Studies also showed that the neural inductive effect of FGF signals also acts independently on its ability to regulate BMP signaling. Inhibition of FGF signaling at pre-gastrula stage chick embryos led to the loss of neural tissue, but epidermis formed normally. BMP inhibition using BMP antagonist, rescued neural differentiation of chick medial epiblast cells exposed to low but not high concentration of FGF inhibitors [37, 38]. Consistently, BMP antagonists cannot induce neural fate of *Xenopus* animal cap if a negative FGF receptor is overexpressed [37]. Collectively, the results suggest that FGF signaling functions during neural induction through both BMP-dependent and BMP-independent manner.

WNT signaling. WNT signaling has been shown to induce epidermis and inhibit neural fate by regulating the response of ectodermal cells to FGF signaling in chick [41]. In chick blastula embryo, medial epiblast tissue (prospective neural plate) didn't express *Wnt3A* and *Wnt8C* mRNA, whereas lateral epiblast tissue (prospective epidermis) expressed both *Wnt3A* and *Wnt8C*. β-catenin, downstream target of WNT signaling, was detect in the nuclei of lateral epiblast but not medial epiblast in chick gastrula embryo. WNT3A and WNT8C proteins inhibited neural differentiation and promoted epidermal differentiation of medial epiblast in blastula epiblast explants and whole chick embryo culture, even in the presence of FGF proteins.

Also, rescue of neural differentiation in medial epiblast cells by BMP inhibitors are dependent on the concentration of added WNT proteins or FGF inhibitors. At low concentration of WNT or FGF inhibitors, BMP antagonist rescued neural differentiation, but at high concentration of WNT or FGF inhibitors, medial epiblast cells still differentiated into epidermis instead of neural cells in the presence of BMP antagonist [41]. Collectively, these results indicate that WNT signaling regulate neural and epidermal fate specification in chick blastula embryo, possibly through regulating the response of cells to FGF signaling (**Figure 1-2**). Medial epiblast cells express FGFs but not WNTs, and thus FGF signaling induced neural fate through BMP-dependent and BMP-independent manner. Lateral epiblast cells express FGFs and WNTs. WNT signaling blocks the response of epiblast cells to FGFs, and thus *Bmp* genes are expressed. BMP signaling promotes epidermal fate.

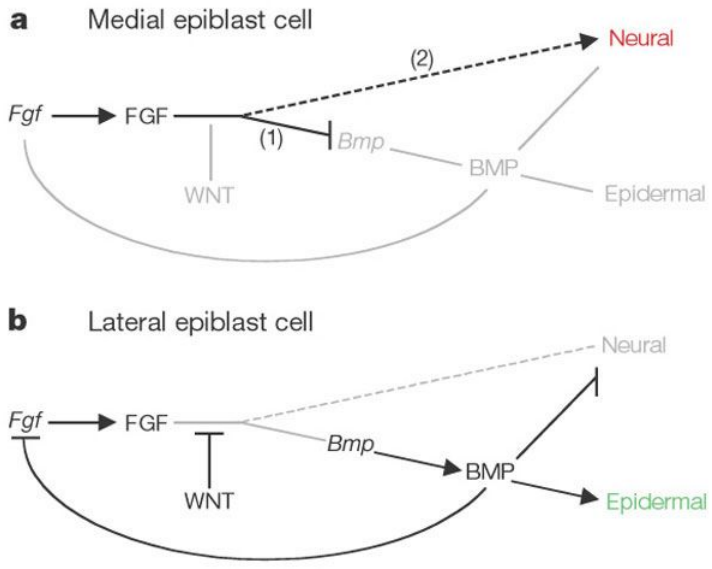

Figure 1-2 Interactions between FGF, WNT and BMP signaling pathways for neural induction in chick embryo. (a) Medial epiblast cells express FGFs but not WNTs. FGF signaling is shown to induce neural fate through BMP-dependent (solid line from FGF) and BMP-independent (dashed line from FGF) manner. (b) Lateral epiblast cells express FGFs and WNTs. WNT signaling blocks the response of epiblast cells to FGFs, and thus *Bmp* genes are expressed. BMP signaling promotes epidermal fate and represses *Fgf* expression. Adapted with permission from reference [41].

1.1.2 Neural plate border specification

NPB region appears soon after neural induction between NP and NNE. NPB cells further differentiate into neural crest cells as the NT closes [42]. Neural crest cells segregate from the dorsal side of the NT and migrate through the embryos to generate a variety of cell types in the peripheral nervous system [43]. Currently there are no markers expressed in the entire NPB region. Pax3/7, Msx, Zic family proteins are expressed in NPB region in a combinatorial manner [44-48]. The specification of NPB depends on signals from its surrounding environment. In this section I briefly summarize our current understanding of NPB specification. I will first introduce the inductive tissues and then summarize the major signaling pathways involved in NPB specification.

Explants co-culture in vitro and grafting experiments in vivo have identified the importance of NP/mesoderm and NP/NNE interaction in regulating the NPB specification. In *Xenopus* and chick, grafting ectoderm into lateral epidermis in vivo induced NPB cells at the boundary between two tissues and NPB cells were generated from both tissues [49, 50]. In vitro juxtaposition of neural and NNE tissue led to similar results [49, 50]. The in vitro combination of ectoderm and paraxial/intermediate mesoderm also led to the induction of NPB from ectoderm tissue in both *Xenopus* and chick [51, 52]. In *Xenopus*, it has been identified that the dorsolateral marginal zone (DLMZ, mesoderm in *Xenopus*) as the source of NPB inductive signaling at the gastrula stage [51, 53]. However, chick medial epiblast explants at pre-gastrulation stage can differentiate into Pax7+ NPB borders in isolation from other tissues in the absence of neural and early mesoderm markers, suggesting neither mesoderm nor NP are required for NPB induction [54-56]. This also indicate that the requirement of mesoderm tissue is species-specific, and signals within ectoderm is sufficient to induce NPB in chick.

Current model of NPB specification suggests the crucial role of BMP concentration. BMP signaling gradient, visualized by phospho-Smad1/5/8 staining, is establish at the ectoderm during early gastrulation in chick, fish and frog embryos in vivo [32, 57, 58]. At gastrula-stage, BMP4 appears to act as a morphogen by providing positional information in regulating ectoderm patterning, with low BMP activity for NP development, intermediate BMP activity for NPB development, and high BMP activity for NNE development [59, 60]. However, modulation of BMP signaling in whole embryo and explants is inefficient to induce NPB [61]. NP tissue can be induced to differentiate into NPB cells by activation of FGF and WNT signaling, suggesting the involvement of FGF and WNT signaling in specifying NPB [61-64]. Multiple WNT proteins are expressed in the ectoderm and restricted to the NNE [41]. Several FGFs are expressed in the paraxial/intermediate mesoderm [53, 62]. In chick, induction of NPB required an early activation of WNT signaling followed by later activation of BMP signaling, while simultaneously activation of both signaling induced epidermis fate [55]. In contrast, in *Xenopus*, WNT signals need to be inhibited for NPB induction [65]. These results suggest that the integration of WNT and BMP signals in NPB specification is species-specific. FGF signaling is known to negatively regulate BMP signaling [39]. FGF signaling and BMP signaling overlapped in the NPB region, where FGF signaling is required to inhibit epidermis differentiation and BMP signaling inhibits neural differentiation. A balance between these two signaling leads to the specification of NPB [56, 66].

1.1.3 Neural tube dorsal-ventral patterning

After neural induction, NP folds toward the dorsal side of the embryo to form NT. The specification of neural fate along AP and DV axes leads to the generation of various neurons and glial cells that compose the CNS. The initial position within the NT dictates the local

environment of progenitor cells and directs the neural fate specification. Spinal cord, the anatomically simplest region in CNS, has been used as a model to study the mechanism of NT DV patterning. The developing spinal cord includes five ventral domains (p3, pMN, p2, p1, p0) and six dorsal domains (dP1-6) (**Figure 1-3**) [6, 7, 67]. The DV patterning of spinal cord is determined by the signals secreted from two opposite signal centers: BMP and WNT secreted from epidermis and roof plate in regulating dorsal NT patterning, Sonic hedgehog (SHH) secreted from notochord and floor plate in regulating ventral NT patterning. In this section I briefly summarize our current understanding in how these signaling pathways regulate NT DV patterning.

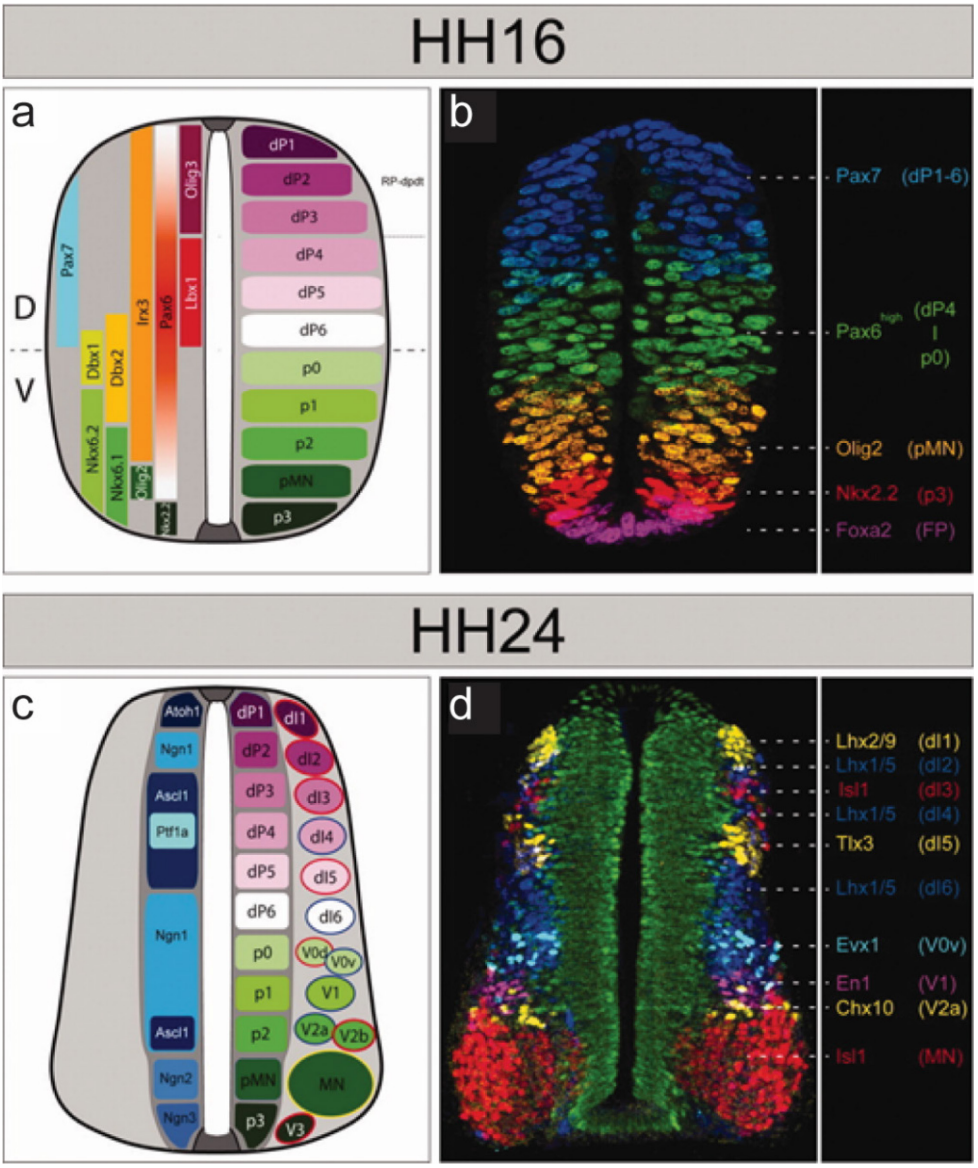

Figure 1-3 Dorsal–ventral patterning of chick developing spinal cord at different stages. (a&b) Schematic representation and a reconstruction of immunostainings of transversal section of a chick neural tube at stage Hamburger and Hamilton (HH) 16 (51–56 h of development, 26–28 somites). (c&d) Schematic representation and a reconstruction of immunostrainings of a transversal section of a chick neural tube at stage HH24 (4 days of development). Adapted with permission from reference [6].

BMP signaling. Before neural tube closure, BMP2, BMP4, and BMP7 begin to be expressed in the chick and mouse epidermal ectoderm [68, 69]. BMP signaling from epidermis is required for the induction of roof plate, which serves as a secondary source of BMP signals to

induce dorsal interneurons [68, 70]. Roof plate induced dorsal NT markers such as PAX3 and MSX when cultured with intermediate NT [68]. Several studies have indicated that BMP signaling is required for dorsal neural tube development. BMP ligands promoted the generation of dI1 and dI3 dorsal neural progenitors in chick neural tube explants in a concentration-dependent manner [68, 71]. Mice lacking two type-1 BMP receptors (ALK3 and ALK6) showed impaired dorsal NT development, with dI1 missing, dI2 reduced and dI3 unchanged, suggesting that different dorsal domains required different level of BMP signaling, with more dorsal-located domains requiring higher BMP activity [72]. These results suggest BMP acts as a morphogen to instruct dorsal NT cell fate in a concentration-dependent manner.

SHH signaling. *Shh* begins to be expressed in the notochord and then induces its own expression in the overlaying floor plate. The timing of ventral NT domain emergence in relation to *Shh* expressed in notochord and floor plate has been carefully examined in mouse NT [73]. In mouse embryo, every somite is emerged around every 90-120 minutes, thus Somitogenesis is used as a convenient temporal indicator. OLIG2 (a marker of pMN domain) was first expressed in the most ventral region of NT at the six-somite stage in a few cells. At eight-somite stage, cells in the most ventral region of NT expressed NKX2.2 (a marker of p3 domain) and lost their expression of OLIG2, and the expression of OLIG2 expanded more dorsally. FOXA2+ (a marker for floor plate) cells were also detected in the eight-somite stage embryo, suggesting the onset of FOXA2 expression is between six-somite and eight-somite stage, but high-level expression of FOXA2 was not evident until the 13-somite stage. SHH secreted by the floor plate appeared at the 16-somite stage, shortly after high-level FOXA2 expression was established in ventral NT (**Figure 1-4**). These results indicate that patterning of ventral NT progenitor domains is establish

by the eight- to ten-somite stage as a result of SHH signaling from the notochord, before SHH expression from the floor plate.

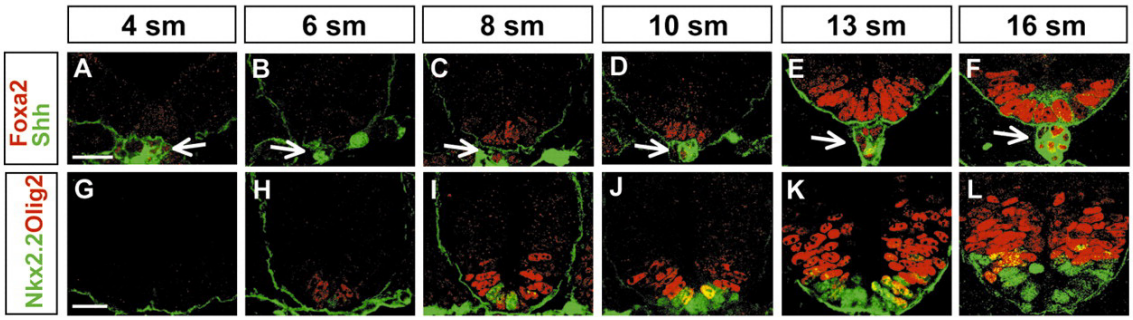

Figure 1-4 Sequential expression of Shh, Foxa2, Nkx2.2 and Olig2 in mouse neural tube around E8.5. (A-L) Immunostaining images of neural tube sections for indicated markers at different somite (sm) stages. Arrows indicate notochord. Scale bar: 25 μm. Adapted with permission from reference [73].

SHH signals by binding to its receptor Patched (Ptc), a transmembrane protein. In the absence of SHH, Ptc inhibits a second transmembrane protein, Smoothened (Smo). The binding of Shh to Ptc relieves Smo inhibition, which in turn leads to the activation of GLI transcription factors, the activator Gli1 and Gli2 and the repressor Gli3. Activation of GLI transcription factors controls the transcription of Shh target genes, such as the homeobox (*Nkx2.2*, *Nkx6.1*, *Nkx6.2*, *Pax6*) and bHLH (*Olig2*) encoding genes [67, 74]. Similar with BMP, SHH also acts as a morphogen to regulate the cell fate in the ventral NT. It is now accepted that the graded SHH signaling activity is mediate by a gradient of Gli activity in ventral neural tube. The level of Gli activity is sufficient to recapitulate the patterning effect of graded SHH signaling [75, 76]. In addition to the level, the duration of Gli activity also plays a role in regulating the cells' response to SHH signaling and ventral cell fate. Ventrally expressed genes take a longer time of Gli activation to be induced than more dorsally expressed genes [75, 77]. To explain how cells integrate the level and duration of SHH signaling, a "temporal adaption" model was proposed by

Dessaud et al. in 2007 [77]. They first found that Gli activity in ventral NT cells gradually decreased when the cells were exposed to a constant amount of SHH, and the duration of Gli activation was proportional to SHH concentration. Duration and concentration of extracellular SHH ligands were transduced into the duration and activity of intracellular Gli activity. And the induction a specific DV domain required the maintenance of Gli activity above a threshold for a period.

1.2 Human pluripotent stem cells: a new paradigm for modeling human development

Due to interspecies divergence, animal models are limited in revealing many fundamental aspects of development principles that are unique to human CNS development. Furthermore, the technical difficulty and ethical constraints in accessing neurulation-stage human embryos have significantly limited experimental investigations of early human CNS development and development of human CNS disease models. Recently, human pluripotent stem cells (hPSCs), including embryonic stem cells (hESCs) and induced pluripotent stem cells (hiPSCs), provide a new paradigm for studying human development and disease modeling [78-82].

Significant progress has been achieved in directed differentiation of hPSCs into specific neuronal subtypes by modulating dynamic chemical signals active in the early embryo [83]. Importantly, self-assembled 3D aggregate cultures of hPS cells have been successfully developed to generate brain organoids with cell types and cytoarchitectures that resemble certain aspects of the embryonic human brain [79, 84, 85]. The most widely used protocol to generate brain organoids is serum-free culture of embryoid body-like aggregates (SFEBq). Yoshiki Sasai and colleagues have developed brain organoids to recapitulate the development of cortical tissue and

optic cup morphogenesis [78, 86]. Lancaster et al. developed a modified SFEBq method to generate cerebral organoids using hPSCs. The cerebral organoids contain discrete brain regions including dorsal cortex, ventral forebrain, retina, hippocampus, and midbrain, and hindbrain. Interestingly, Lancaster et al. modeled critical disease-specific phenotypes of microcephaly using patient-derived hiPSCs using cerebral organoids [79]. Qian et al. developed a miniature spinning bioreactor, SpinΩ, to generate brain region-specific organoids, including forebrain, midbrain and hypothalamic organoids [87]. Recently, Orly Reiner and colleagues have recapitulated the human brain wrinkling by culturing brain organoid in a confined environment [84]. Brain organoids have emerged as novel model systems to investigate human brain development and disorders at the molecular, cellular, structural and functional levels.

However, it is worth noting that although hPSCs have been extensively applied to modeling organogenesis, at the time of initiation of this dissertation, it remains undetermined whether hPSCs can be guided to self-organize into spatially patterned structures to model neural induction. And only a few studies have been done to model NT patterning using mouse and human PSCs. Elly Tanaka has done pioneering work to use mouse ESC to model NT DV patterning (**Figure 1-5**) [88]. When cultured in Matrigel or synthetic PEG gel under neural induction condition, mouse ESCs differentiated into NE cells and self-organized into 3D cystic structure, termed NE cysts, with apical surfaces facing the central lumen. NE cysts maintained a default dorsal identity and were responsive to different inductive signals, including smoothened agonist (SAG) for ventralization and retinoid acid (RA) for posteriorization. More interestingly, global treatment of RA induced DV patterning of NE cysts. Time lapse study of DV marker expression demonstrated that FOXA2 expression preceded SHH in one pole of cysts, followed by OLIG2, a marker for motor neuron progenitors. I want to point out that the time course of

SHH, FOXA2 and OLIG2 expression is not consistent with mouse embryo development in vivo. In mouse ventral neural tube patterning, SHH secreted from notochord works as a morphogen to induce FOAX2 and OLIG2 expression [73]. Ranga et al. developed a fully defined synthetic ECM matrix and found that matrix rigidity, degradability, and ECM composition affects both early apical-basal polarity and late dorsal-ventral patterning [89]. Optimizing ECM components and rigidity increased the efficiency of DV patterning of NE cysts.

A recent work reports 3D induction of dorsal, intermediate, and ventral spinal cord-like tissue from human PSCs in a free-floating culture condition by regulating SHH signaling (**Figure 1-5**) [90]. Although global cell fate patterning is not achieved in this spinal cord-like tissue, they observed local cell fate patterning. Multiple localized roof plate-like structures with LMX1+ roof plate cells surrounded by MSX1/2+ dorsal neural progenitor cells emerged in single dorsal spinal cord tissue. Multiple localized patterning of ventral cell fate with spatially aligned floor plate/p3/pMN structures similar to in vivo spinal cord development was observed in single ventral spinal cord tissue. However, this work fails to recapitulate correct apical-basal polarity observed in neural tube, with apical surface facing outside the structure. Similar apical-basal polarity has also been reported in other organoids structure from hPSCs in free-floating culture condition [91, 92].

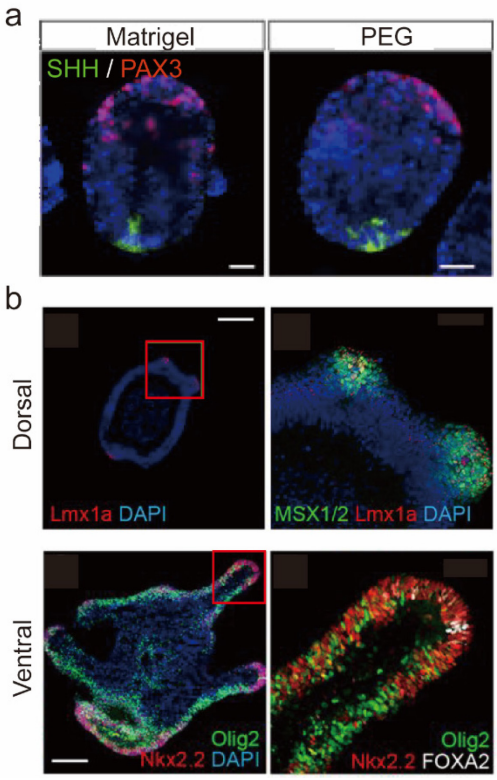

Figure 1-5 In vitro models of dorsal-ventral patterning of the neural tube. (a) DV-patterned neuroepithelial cysts derived from mouse ES cells cultured in Matrigel and synthetic PEG gels. Scale bar, 20 μm. Adapted with permission from Reference [88]. (b) Human PS cell-derived dorsal and ventral spinal cord-like tissues. Scale bar, 200 μm. Adapted with permission from Reference [90].

1.3 Research topics and dissertation outline

In this dissertation, I leveraged the developmental potential and self-organizing properties of hPS cells in conjunction with 2D and 3D bioengineering tools to develop spatially patterned multicellular tissues that mimic early human neurulation process, including neural induction and DV patterning of the NT. These hPS cell-based in vitro models are important alternatives to animal models to study the self-organizing principles involved in autonomous patterning during human neurulation.

In **chapter 2**, I developed a novel hPSC-based developmental model for human neural induction. By providing geometrical confinement using microcontact printing, hPS cells differentiate and self-organize into spatially organized NE and NPB cells, mimicking neuroectoderm patterning during early neurulation.

In **chapter 3**, leveraging the hPSC-based neural induction models developed in chapter 2, I implemented various mechanical stimulation and characterization tools such as polydimethylsiloxane (PDMS) micropost array and cell stretching device in the neural induction model to study the interaction and crosstalk between mechanical cues and classic developmental signaling such as BMP signaling to regulate NE and NPB lineage bifurcation. I found that increased cell shape and contractile force at the colony periphery result in nuclear accumulation and transcriptional activation of p-SMAD 1/5, which in turn up-regulates NPB specifier genes including *PAX3*, *SOX9* and *SOX10*. Confined cell shape with limited contractile force at the colony center leads to nuclear exclusion of p-SMAD 1/5 and NE differentiation.

In **chapter 4**, I report a biomimetic 3D culture system mimicking the in vivo neurogenic niche for the development of a hPSC-based, DV patterned human NT development model. The biomimetic 3D culture incorporates some key in vivo neurogenic niche elements, including a 3D basal lamina extracellular matrix (ECM) to provide a permissive extracellular environment and a soft tissue bed to reconstruct the mechanical environment of the neuroepithelium during neurulation. This 3D biomimetic culture system allows for convenient manipulations of the dynamic interplay between chemical and biophysical signals that are critical for the cellular morphogenetic events and progressive neuronal fate specification during DV patterning of NT-like tissues derived from hPSCs. Development of the biomimetic 3D culture system, together

with extrinsic exogenous biochemical signals delivered at precise timing and concentration, allowed me to apply hPSCs to achieve the development of a human NT development model with DV patterning.

Finally, in **chapter 5,** I summarize this dissertation work and provide perspectives on future efforts in incorporating advanced bioengineering tools to generate controllable experimental systems with hPSCs to advance knowledge of human neurulation and use such systems for disease modelling and high-throughput screening.

Chapter 2

Self-Organized Neuroectoderm Patterning by Human Pluripotent Stem Cells

The major content of this chapter is reproduced from my previously published paper: "Mechanics-guided embryonic patterning of neuroectoderm tissue from human pluripotent stem cells." in Nature materials, 2018 [93].†

2.1 Introduction

Neural induction, as an evolutionarily conserved developmental event, initiates the neurulation process by patterning the ectoderm into spatially organized NP, NPB, and NNE regions (**Figure 2-1**). Accompanying progressive cell fate specifications during neural induction, morphogenetic events occur as the ectoderm becomes thickened in the dorsal region to form pseudostratified, columnar neuroepithelial (NE) cells in the prospective NP domain [94]. Classic studies of animal models have revealed the importance of integrated signaling networks involving NODAL, BMP, FGF and WNT signaling to regulate neural induction [2, 3, 40, 95]. In particular, graded BMP signaling has been identified to guide ectoderm patterning, with high BMP signaling promoting NNE differentiation, low BMP activity required for NP formation, and

† Research presented in this chapter has received assistance from Dr. Yubing Sun (cell culture, design differentiation assay), Ms. Agnes Resto-Irizarry (imaging processing), and Mr. Ye Yuan (Cell migration assay). I would also like to thank Dr. Jianping Fu for his supervision and Dr. Allen Liu for his comments on the research presented in this chapter.

intermediate BMP promoting NPB development [22, 96]. A balance between FGF and BMP signaling is also important for establishing and maintaining the NPB region [31]. Recent studies further demonstrate the role of WNT signaling in refining the boundary between NP and NNE by regulating the ectoderm's response to BMP and FGF signaling [41, 55].

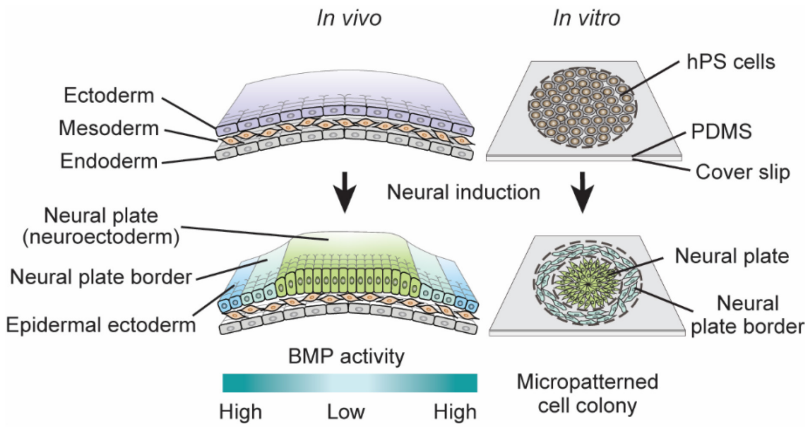

Figure 2-1 Schematic of neural induction in vivo and in vitro. During neural induction *in vivo*, cells in the ectoderm form the neural plate (NP, or neuroectoderm), neural plate border (NPB) and epidermal ectoderm. Neural induction of circular hPS cell colonies leads to autonomously patterned neuroectoderm tissues, with NP cells at colony central region and NPB cells at colony periphery.

Human pluripotent stem cells (PSCs), including embryonic stem cells (ESCs) and induced pluripotent stem cells (iPSCs), due to their pluripotency and unlimited self-renewal capacity, provide a new paradigm for studying human development and disease modeling [78-82]. Although extensive studies have been performed to differentiate hPSCs into a variety of neuron subtypes, neural induction occurs with dynamic fate patterning and complicated morphogenetic events; studying human neural induction requires in vitro models that recapitulate spatiotemporal ectodermal lineage specification and patterning and key morphogenetic events. Recently, our lab and others have demonstrated that by controlling and colony shape and size, geometrical confinement could induce spatially organized cell fate patterning of hPS cells,

mimicking embryonic patterning including gastrulation and neurulation in vivo [80, 93, 97-102]. Here I developed a novel hPS cell-based developmental model of human neural induction. By providing geometrical confinement using microcontact printing, hPS cells differentiate and self-organize into spatially organized NE and NPB cells, mimicking neuroectoderm regionalization during early neurulation.

2.2 Materials and Methods

2.2.1 Culture medium

PluriQ™ Human Cell Conditioned Medium was purchased from MTI-GlobalStem. It supports feeder-free growth of hPS cells [103].

Growth medium contained DMEM/F12 (GIBCO), 20% KnockOut Serum Replacement (KSR; GIBCO), 0.1 mM β-mercaptoethanol (GIBCO), 2 mM glutamax (GIBCO), 1% non-essential amino acids (GIBCO), and 4 ng mL^{-1} human recombinant basic fibroblast growth factor (bFGF; GlobalStem).

Neural induction medium: To promote neural induction, TGF-β inhibitor SB 431542 (10 μM; Cayman Chemical) and BMP4 inhibitor LDN 193189 (500 nM; Selleckchem) were supplemented into the growth medium. At day 3, WNT activator CHIR99021 (3 μM; Cayman Chemical) was added to the medium and was withdrawn at day 4.

Motor neuron (MN) differentiation medium consists of N2B27 medium supplemented with retinoic acid (RA, 1 μM; Stemcell Technologies) and smoothened agonist (SAG, 500 nM; Stemcell Technologies). N2B27 medium contained 1:1 mixture of DMEM/F12 and neurobasal

medium (GIBCO), 1% N2 supplement (GIBCO), 2% B-27 supplement (GIBCO), 2 mM glutamax and 1% non-essential amino acids.

Neural crest (NC) cell differentiation medium contained N2B27 medium supplemented with CHIR99021 (3 μM).

All culture medium was pre-equilibrated at 37 °C and 5% CO_2 before use.

2.2.2 Cell culture.

The H1 hES cell line (WA01, WiCell; NIH registration number: 0043) was cultured on mitotically inactive mouse embryonic fibroblasts (MEFs; GlobalStem) using growth medium with daily medium exchange. The H9 hES cell line (WA09, WiCell; NIH registration number: 0062), provided by Dr. Deborah L. Gumucio, was maintained in a standard feeder-free culture system using mTeSR1 medium (Stemcell Technologies) and lactate dehydrogenase-elevating virus (LDEV)-free hES cell-qualified reduced growth factor basement membrane matrix Geltrex™ (Thermo Fisher Scientific; derived from Engelbreth-Holm-Swarm tumors similarly as Matrigel®) per the manufacturers' instructions. A hiPS cell line, a gift from Dr. Paul H. Krebsbach, was cultured on poly[2-(methacryloyloxy)ethyl dimethyl-(3-sulfopropyl)ammonium hydroxide] (PMEDSAH) coated tissue culture dishes in human cell conditioned medium (MTI-GlobalStem) as described previously[104]. The hiPS cell line was derived from human foreskin fibroblasts by over-expression of *OCT4*, *SOX2*, *KLF4*, and *c-MYC* using Sendai virus constructs (Invitrogen).

H1 hES cells were passaged every 5 d using the STEMPRO EZPassage Disposable Stem Cell Passaging Tool (Invitrogen). Before passaging, differentiated cells were removed manually

using a modified pasteur pipette under a stereomicroscope (Olympus). Cells were rinsed briefly with PBS and treated with TrypLE Select (Invitrogen) for 2 min to release MEFs. Cells were rinsed briefly again with PBS before all cells, including hES cells and remaining MEFs, were collected using a cell scraper (BD Biosciences). To remove contaminating MEFs, all cells were transferred onto a 60-mm tissue culture dish (BD Biosciences) coated with gelatin (Sigma) and incubated for 45 min. MEFs attach to the dish while hES cells remain in suspension. hES cells in suspension were collected and centrifuged, and the resulting cell pellet was re-dispersed in growth medium supplemented with Y27632 (10 μM; Enzo Life Sciences) before cell seeding. For passaging H9 hES and hiPS cells, cells were dossociated using TrypLE Select before cell seeding. The detailed cell culture methods are in **Appendix A**.

All protocols for the use of hPS cell lines have been approved by the Human Pluripotent Stem Cell Research Oversight Committee at the University of Michigan. All cell lines were authenticated as karyotypically normal by Cell Line Genetics (Madison WI). All cell lines tested negative for mycoplasma contamination (LookOut Mycoplasma PCR Detection Kit, Sigma-Aldrich).

2.2.3 Microcontact printing.

Soft lithography was used to generate patterned PDMS stamps from negative silicon molds that were made using conventional microfabrication techniques including photolithography and deep reactive-ion etching (DRIE), as described previously[105]. These PDMS stamps were then applied for generating micropatterned hPS cell colonies and patterned single hPS cells using microcontact printing as described previously[105]. Briefly, to generate micropatterned hPS cell colonies and patterned single hPS cells on flat PDMS surfaces, round

glass coverslips with a diameter of 18 mm (Fisher Scientific) were spin coated (Spin Coater; Laurell Technologies) with a thin layer of PDMS prepolymer containing PDMS base monomer and curing agent (10:1 *w* / *w*; Sylgard 184, Dow-Corning) before the PDMS layer was thermally cured by baking at 110 °C for at least 24 hr. In parallel, PDMS stamps were immersed in a vitronectin solution (20 μg mL^{-1}; Trevigen) for 1 hr before blowing dry under nitrogen. It has been reported that vitronectin supports self-renewal of hPS cells[106]. Vitronectin-coated PDMS stamps were then placed in conformal contact with UV ozone-treated, surface-oxidized PDMS layers on coverslips (ozone cleaner; Jelight), to facilitate vitronectin transfer from stamps to coverslips. After PDMS stamps were removed, coverslips were sterilized by briefly immersing them in 100% and 70% ethanol (Fisher Scientific). Protein adsorption to PDMS surfaces not coated with vitronectin was prevented by immersing coverslips in 0.2% Pluronics F127 NF solution (BASF) for 30 min. Coverslips were rinsed with PBS and transferred to standard 12-well tissue culture plates for cell seeding. For micropatterned hPS cell colonies, PDMS stamps containing circular patterns with diameters of 300, 400, 500 and 800 μm were used. For patterned single hPS cells with defined cell shapes, PDMS stamps containing circular patterns with diameters of 25 and 45 μm were used.

2.2.4 Stencil micropatterning.

Stencils were prepared by punching through-holes into PDMS membranes using a 500 μm biopsy puncher (Fisher Scientific). To generate PDMS membranes, a thin layer of PDMS prepolymer containing PDMS base monomer and curing agent (10:1 *w* / *w*) was spun on a silicon wafer at 400 rpm for 90 sec before the PDMS layer was thermally cured by baking at 60 °C for at least 24 hr. The PDMS membrane was then peeled from the silicon wafer before punching through-holes into the PDMS membrane. Coverslips were incubated in a vitronectin solution (20

μg mL^{-1}) at room temperature for 1 hr before the PDMS stencil was attached to the vitronectin-coated coverslip. The coverslip with the PDMS stencil on top was then ready for cell seeding.

2.2.5 Immunocytochemistry.

Cells were fixed with 4% paraformaldehyde (Electron Microscopy Sciences) for 15 min and then permeabilized with 0.1% Triton X-100 (Roche Applied Science) for 20 min at room temperature. Primary antibodies (listed in **Appendix B**) were used and detected by goat-anti mouse Alexa Fluor 488 and/or goat-anti rabbit Alexa Fluor 546 secondary antibodies. Alexa Fluor 555 conjugated phalloidin (Invitrogen) was used for visualization of actin microfilaments. To visualize nuclei, cells were stained with 4,6-diamidino-2- phenylindole (DAPI; Invitrogen).

2.2.6 Image analysis.

Fluorescence images were recorded using either an inverted epifluorescence microscope (Zeiss Axio Observer Z1; Carl Zeiss MicroImaging) equipped with a monochrome charge-coupled device (CCD) camera or a spinning disc confocal microscope (Olympus). For image analysis of micropatterned hPS cell colonies, fluorescence images were first cropped using a custom-developed MATLAB program (MathWorks) to a uniform circular size (as defined by the colony size) with pattern centroids aligned. Please note that due to intrinsic heterogeneous cell seeding, some multilayered cellular structures would inevitably appear in micropatterned cell colonies. These multilayered colonies were excluded from data analyses. Fluorescence intensity of each pixel on cropped images was then normalized by the maximum intensity identified on each image. These images were stacked to obtain average intensity maps. To normalize fluorescence intensities of cell lineage markers by DAPI intensity, the intensity of cell lineage markers for each pixel of images was divided by corresponding DAPI intensity. These DAPI-

normalized images were stacked together to obtain average DAPI-normalized intensity maps. To plot average intensity as a function of distance from colony centroid, average intensity maps of circular hPS cell colonies were first divided into 100 concentric zones with equal widths. The average pixel intensity of each concentric zone was then calculated and plotted against the mean distance of the concentric zone from colony centroid. From average intensity plots of cell lineage markers, values of the full width at half maximum (FWHM) were determined as the difference between the two radial positions at which the average fluorescence intensity of individual markers is equal to half of its maximum value. The FWHM for average DAPI intensity plots was decided by first calculating the half width at half maximum (HWHM), which was determined as the radial position at which the average DAPI intensity is equal to half of its maximum value at colony centroid. FWHM for average DAPI intensity plots was then calculated as double the HWHM.

Colony thickness and nucleus orientation of hPS cell colonies were determined manually with ImageJ using confocal images showing *X-Z* sections of hPS cell colonies stained for N-CADHERIN. Normalized nucleus dimension was further calculated as the ratio of the height to width of a circumscribed rectangle bounding the nucleus. Projected cell areas were quantified with the CellProfiler program using immunofluorescence images showing ZO-1 staining. Nuclei stained by DAPI was used for identification of each cell as primary objects in CellProfiler. ZO-1 staining images were first filtered to remove background before segregating using a propagation method to determine cell areas. To determine projected cell area for central and peripheral zones of hPS cell colonies, a binary circular mask with a diameter of half of the actual pattern diameter was used to crop original hPS cell colony images. Cells falling on the mask boundary were excluded from quantification. Immunofluorescence images showing p-SMAD 1/5 staining were

analyzed manually using ImageJ. Cells with nuclear p-SMAD 1/5 were identified as those showing dominant nuclear fluorescence and absence of cytoplasmic fluorescence. Conversely, cells with cytoplasmic p-SMAD 1/5 were identified as those showing absence of nuclear fluorescence. To quantify the spatial distribution of BMP-SMAD activation, circular colonies were divided into 4 concentric zones with equal widths. The percentage of cells with nuclear p-SMAD 1/5 in each zone was then calculated and plotted against the distance from the colony centroid.

2.2.7 Tracking cell migration and unbiased random walk model.

On day 0 before cell seeding, hPS cells were labeled with CellTracker Red CMTPX Dye (ThermoFisher Scientific) for 30 min. Labeled hPS cells were mixed with unlabeled cells at a ratio of 1:7 before the cell mixture was seeded onto coverslips containing micropatterned circular adhesive islands. From day 2 (t = 0 hr) to day 4, live cell imaging was conducted using an inverted epifluorescence microscope (Zeiss Axio Observer Z1) enclosed in an environmental incubator (XL S1 incubator, Carl Zeiss MicroImaging) maintaining the cell culture at 37 °C and 5% CO_2. Both bright field and fluorescence images were recorded every 20 min for a total of 41 hr. All time-lapse images were reconstructed using the image processing software Image-Pro Plus to generate TIFF stacks for cell migration tracking. For each image, peripheries of each individual CellTracker labeled cells were marked manually. Positions of cell centroids were then identified from each image to calculate end-to-end cell displacement D and radial displacement during cell migration as a function of time. For radial displacement calculations, cells were divided into two groups based on their radial positions relative to the colony centroid at t = 0 hr (R_0) ('central': $0 \leq R_0 \leq 100$ μm; 'peripheral': $100 < R_0 \leq 200$ μm). If labeled hPS cells divided

during cell migration tracking, one of the daughter cells was randomly selected to continue tracking.

An unbiased random walk model was used to model cell migration during emergent neuroectoderm patterning in micropatterned circular hPS cell colonies. In this model, cells are assumed to move randomly without any preferred migration direction. Cell centroids at each time step *n* (denoted here as $\vec{D}_n$) can be calculated as $\vec{D}_n = \vec{D}_{n-1} + AV\vec{\gamma}$, where A is a random variable following a uniform distribution on [0, 1] and $\vec{\gamma}$ is a random unit direction vector. Parameter V denotes the maximum cell centroid displacement at each time step, and it can be obtained through least square fitting for experiment data of mean square end-to-end cell displacement D^2 using the expression $D^2 = V^2 t / 4$.

2.3 Results and discussion

Here, I sought to develop micropatterned hPS cell colonies on two-dimensional substrates to model neural induction. Microcontact printing was utilized to generate vitronectin-coated, circular adhesive islands with a diameter d = 400 μm on flat poly-dimethylsiloxane (PDMS) surfaces coated on glass coverslips. H1 hES cells were plated as single cells at 20,000 cells cm^{-2} on adhesive islands to establish micropatterned colonies with a defined circular shape and size. A differentiation medium supplemented with the dual SMAD inhibitors, SB 431542 (SB, TGF-β inhibitor; 10 μM) and LDN 193189 (LDN, BMP4 inhibitor; 500 nM), was applied for neural induction[107] (**Figure 2-2**). The β-catenin stabilizer CHIR 99021 (CHIR, 3 μM), a WNT activator, was also supplemented for cell culture (**Figure 2-2)** as it promotes NPB cell

specification under neural induction condition established by the dual SMAD inhibitors[108, 109].

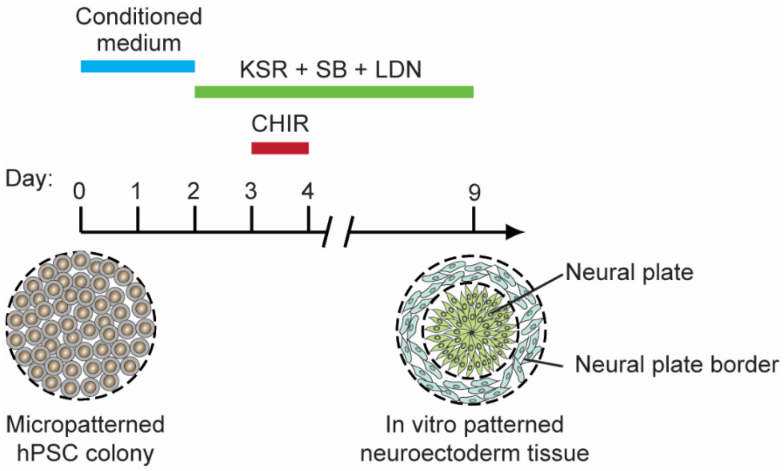

Figure 2-2 Neural induction protocol. Micropatterned hPSC colonies are first cultured in PluriQ™ Human Cell Conditioned Medium (MTI-GlobalStem) for two days before switching to neural induction medium on day 2. Dual SMAD inhibitors SB 431542 (10 µM) and BMP4 inhibitor LDN 193189 (500 nM) were supplemented into the growth medium. At day 3, WNT activator CHIR99021 (3 µM) was added to the medium and was withdrawn at day 4.

While cells distributed uniformly on adhesive islands 24 hr after initial cell plating, neural induction resulted in differentiating cells gradually accumulating in colony central area, leading to a significantly greater cell density at colony center than periphery (**Figure 2-3 a**). Cell density was further analyzed based on DAPI fluorescence intensity. The full width at half maximum (FWHM) for spatial distributions of DAPI intensity decreased continuously from 336 µm at day 1 to 240 µm at day 9 (**Figure 2-3 b**). Confocal images further showed that micropatterned colonies at day 7 remained as a monolayer. Strikingly, quantitation of colony thickness and nucleus shape revealed that, at this point, cells exhibited a gradual change of cell shape from a columnar phenotype with columnar nuclei at colony center to a cuboidal morphology with rounded nuclei at colony periphery (**Figure 2-3 c-e**), consistent with characteristic neuroectoderm thickening during neural induction *in vivo*[94, 110].

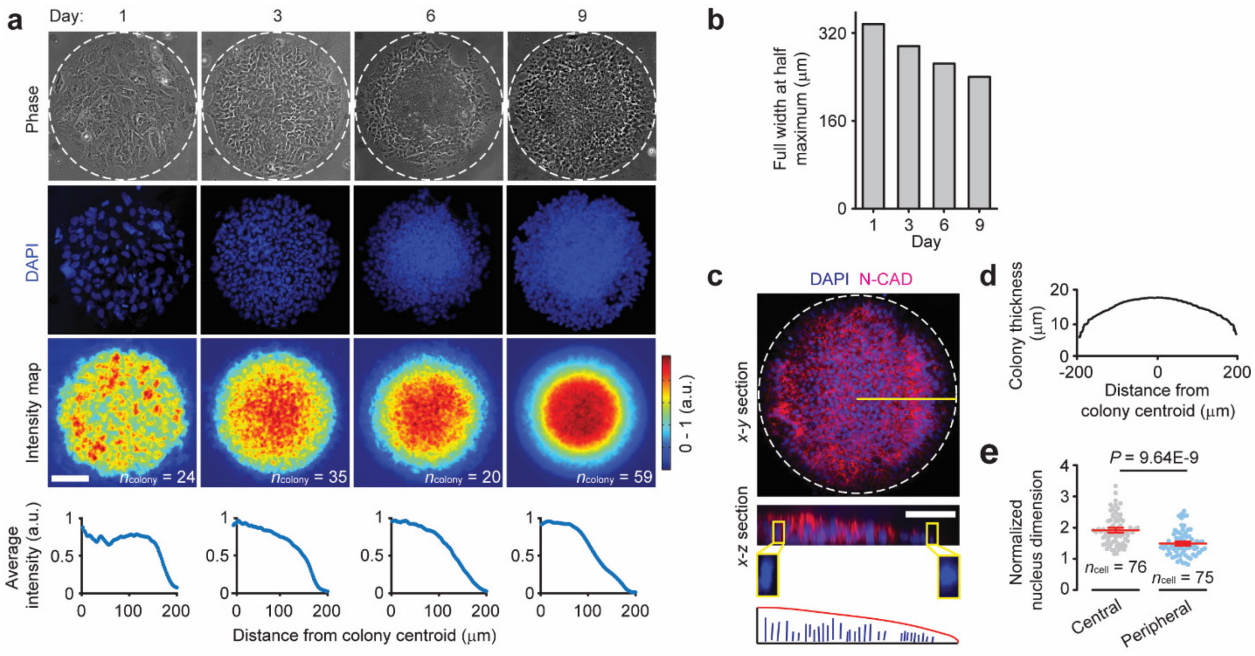

Figure 2-3 Morphology characterization during self-organized neuroectoderm patterning in circular hPS cell colonies. (a) Representative phase contrast and fluorescence images showing cell morphology and nuclei (stained by DAPI), respectively, at different days. White dashed lines mark the colony periphery. Experiments were repeated three times with similar results. Average intensity maps and plots show spatial distributions of DAPI intensity. Number of colonies analyzed were pooled from n = 3 independent experiments. Data were plotted as the mean. Scale bar, 100 μm. (b) Bar plot of full width at half maximum for average normalized DAPI intensity curves in A. (c) Representative confocal micrographs showing colonies at day 7 stained for N-CADHERIN. Zoomed-in images show nucleus shape at colony center and periphery. Experiments were repeated twice with similar results. Bottom plot shows colony outline (red curve) and nucleus orientation (blue arrows). Scale bars, 50 μm. (d&e) Colony thickness (d) and normalized nucleus dimension (e) at day 7 (see Methods). Colony thickness and nucleus dimension were plotted as the mean and the mean ± s.e.m., respectively, with data pooled from n = 2 independent experiments and 12 colonies. P value was calculated using unpaired, two-sided Student's *t*-test.

Importantly, PAX6$^+$ neuroepithelial (NE) cells, the neural progenitor in the NP, were found preferentially localized at the colony center on day 9, whereas PAX3$^+$, ZIC1$^+$ and MSX1$^+$ NPB cells were concentrated at the colony periphery, forming a concentric ring-shaped tissue sheet consistent with neuroectoderm patterning and proper regionalization of NE and NPB cells (**Figure 2-4**). Interestingly, the concentric zone of PAX3$^+$ cells at colony periphery exhibited a smaller zone width, as characterized by FWHM for spatial distribution of PAX3 intensity (92 μm), compared with concentric zones of ZIC1$^+$ (128 μm) and MSX1$^+$ (175 μm) cells,

respectively (**Figure 2-4**). This observation is consistent with *in vivo* findings that ZIC1^{+} cells also exist in the neurogenic placode regions [111]. Emergent patterning of neuroectoderm tissues with proper autonomous regionalization of NE and NPB cells was also achieved using another hES cell line (H9) and a human induced pluripotent stem (hiPS) cell line under the default neural induction condition (**Figure 2-5**).

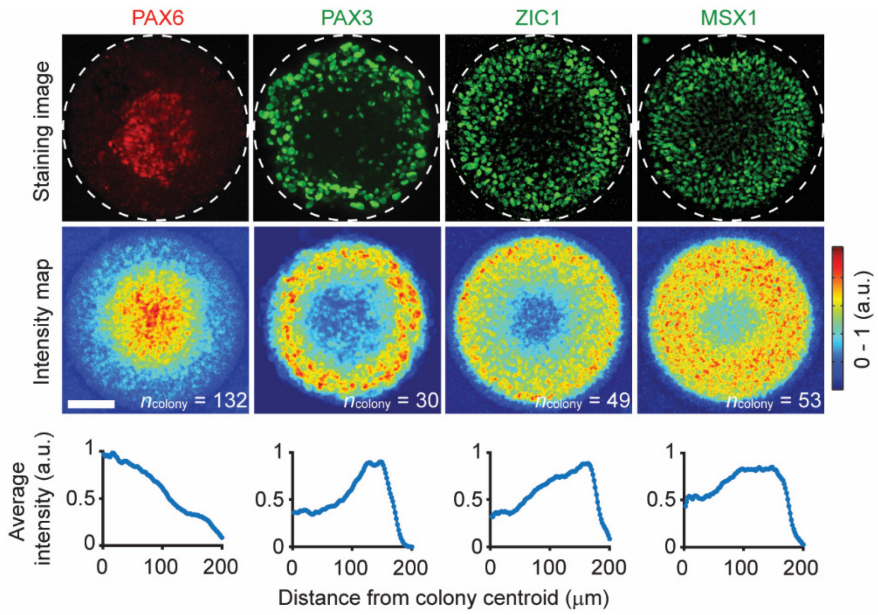

Figure 2-4 Cell fate patterning of self-organized of hPS cell-derived neuroectoderm tissue. Representative immunofluorescence micrographs showing colonies at day 9 stained for neuroectoderm marker PAX6 and NPB markers PAX3, ZIC1 and MSX1. White dashed lines mark colony periphery. Average normalized DAPI intensity maps and plots are shown (see **Methods**). Experiments were repeated three times with similar results. Number of colonies analyzed were pooled from $n = 3$ independent experiments. Data were plotted as the mean. Scale bar, 100 μm.

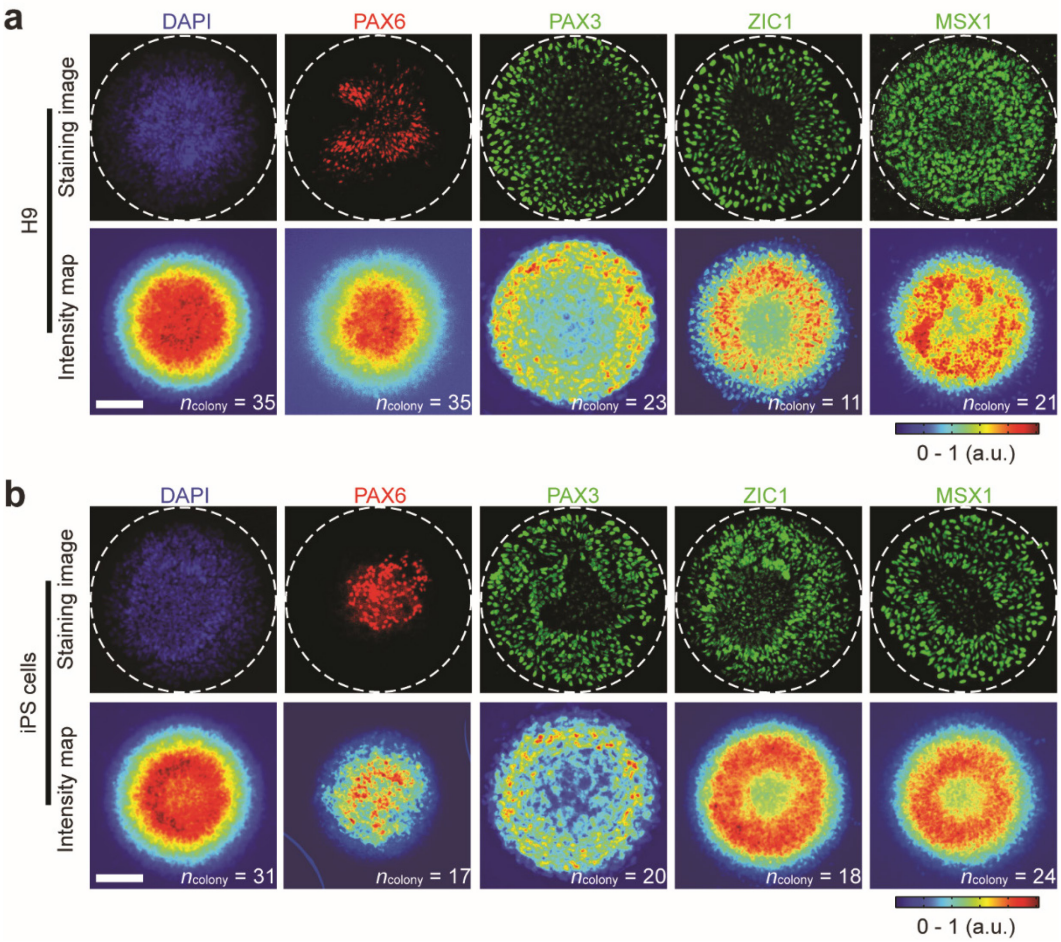

Figure 2-5 Self-organized neuroectoderm patterning from micropatterned circular colonies of different hPS cell lines. (**a**) H9 hES cell line. (**b**) A hiPS cell line. In **a** & **b**, representative immunofluorescence micrographs and average intensity maps are shown for colonies at day 9 stained for neuroepithelial cell marker PAX6 and neural plate border marker PAX3, ZIC1 and MSX1. DAPI counterstained nuclei. White dashed lines mark colony periphery. Experiments were repeated three times with similar results. Number of colonies analyzed were pooled from $n = 3$ independent experiments. Data were plotted as the mean. Scale bars, 100 μm. hPS cells were plated on day 0 at 20,000 cells cm^{-2} onto circular adhesive patterns with a diameter of 400 μm.

To confirm the differentiation potentials of neuroectoderm tissues after neural induction, they were cultured continuously under a motor neuron (MN) differentiation medium[112] or a neural crest (NC) differentiation medium[108, 109] (**Figure 2-6 a**). On day 0, a thin PDMS membrane containing circular through holes ($d = 500$ μm) was placed onto vitronectin-coated coverslips before seeding hPS cells. hPS cells were treated with neural induction medium till day 9. On day 9, the PDMS membrane was peeled from coverslips, and culture medium was

switched to MN differentiation medium containing N2B27, retinoic acid (RA, 1 μM) and the smoothened agonist (SAG, 500 nM), or to NC cell differentiation medium containing N2B27 and CHIR 99021 (CHIR, 3 μM). Importantly, on day 16, only putative NE cells at the colony central region could differentiate into $OLIG2^+$ MN progenitor cells, whereas only putative NPB cells at the colony periphery were capable of differentiating into $AP2\alpha^+$ and $SOX10^+$ NC cells (**Figure 2-6**).

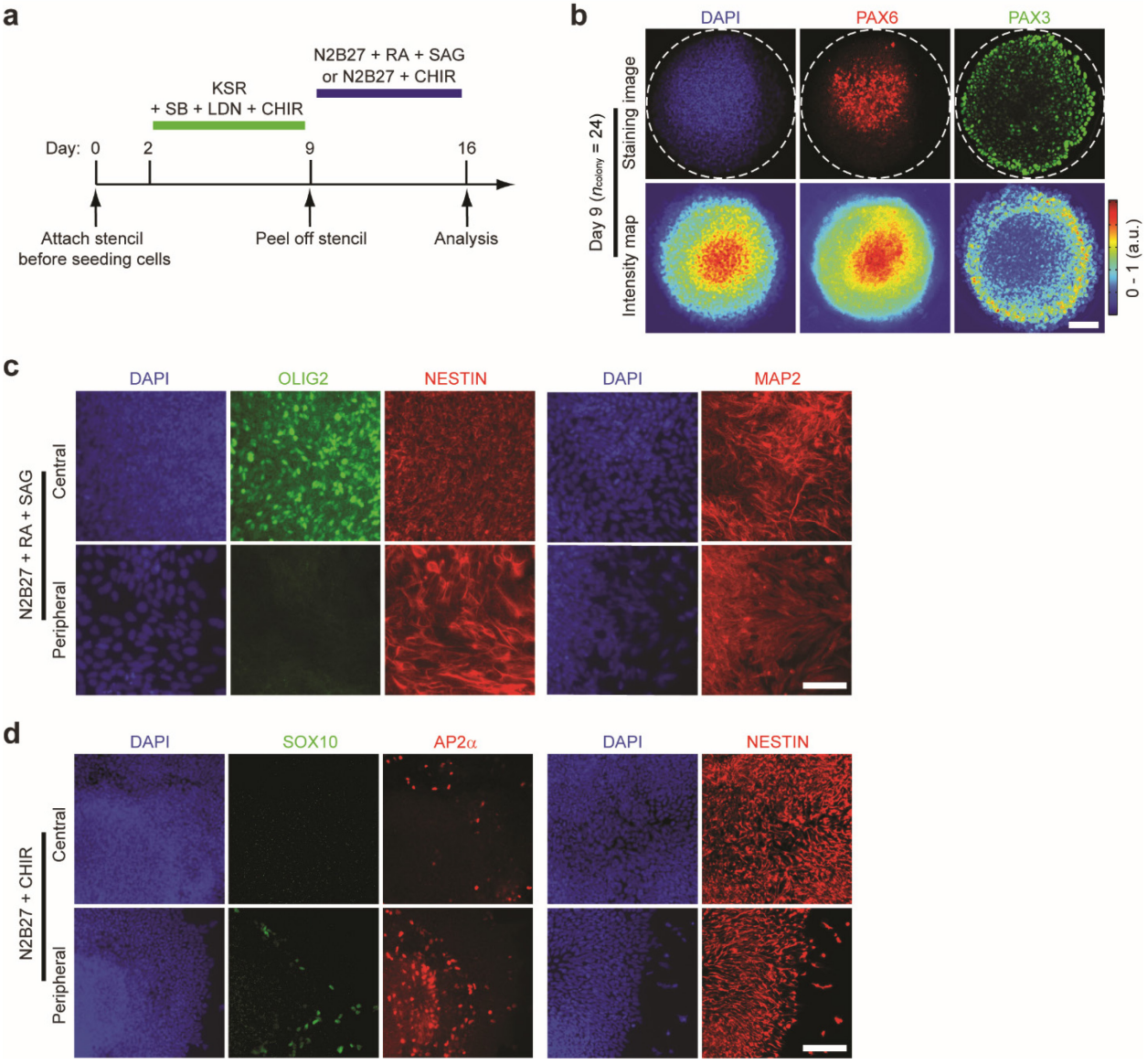

Figure 2-6 Differentiation potential of neuroepithelial (NE) and neural plate border (NPB) cells. (**a**) Schematic showing differentiation of NE cells towards motor neuron (MN) or differentiation of NPB cells towards neural crest (NC) cells using PDMS stencils. (**b**) Representative immunofluorescence micrographs and average intensity maps showing PAX6 and PAX3 staining at day 9. DAPI counterstained nuclei. White dashed lines mark colony periphery. Experiments were repeated three times with similar results. Number of colonies analyzed were pooled from $n = 3$ independent experiments. Data were plotted as the mean. Scale bar, 100 µm. (**c**) Representative immunofluorescence micrographs showing central and peripheral zones of cell colonies cultured in MN differentiation medium at day 16 stained for MN progenitor marker OLIG2 and pan-neuronal markers NESTIN and MAP2. DAPI counterstained nuclei. Scale bar, 50 µm. (**d**) Representative immunofluorescence micrographs showing central and peripheral zones of cell colonies cultured in NC cell differentiation medium at day 16 stained for NC cell marker AP2α and SOX10 and pan-neuronal marker NESTIN. DAPI counterstained nuclei. Scale bar, 50 µm.

hPS cells were plated on day 0 at 20,000 cells cm^{-2}. For **c** & **d**, experiments were repeated twice with similar results.

We next sought to examine the effect of colony size on self-organized neuroectoderm patterning. To this end, circular adhesive islands with diameters *d* of 300, 400, 500 and 800 μm were fabricated and compared. Neural induction resulted in the emergence of concentric, ring-shaped neuroectoderm tissues with proper regionalization of NE and NPB cells at day 9 for all colonies (**Figure 2-7**). Interestingly, the $PAX6^+$ NE circular pattern size and the concentric zone width of $PAX3^+$ NPB cells, as characterized by FWHM for spatial distributions of PAX6 and PAX3 intensities, respectively, appeared relatively constant for colony diameters *d* between 300 - 500 μm (**Figure 2-7 a, b & d**). Notably, neural induction for colony diameter *d* = 800 μm led to marked cell accumulation at the colony periphery on day 9, coinciding with a notable number of $PAX3^+$, $ZIC1^+$, and $MSX1^+$ NPB cells at colony central region (**Figure 2-7 c**). The underlying mechanism(s) leading to different cell distributions in micropatterned colonies with *d* = 800 μm remains unclear, and likely involves secondary tissue morphogenesis under such sub-optimal culture conditions [113].

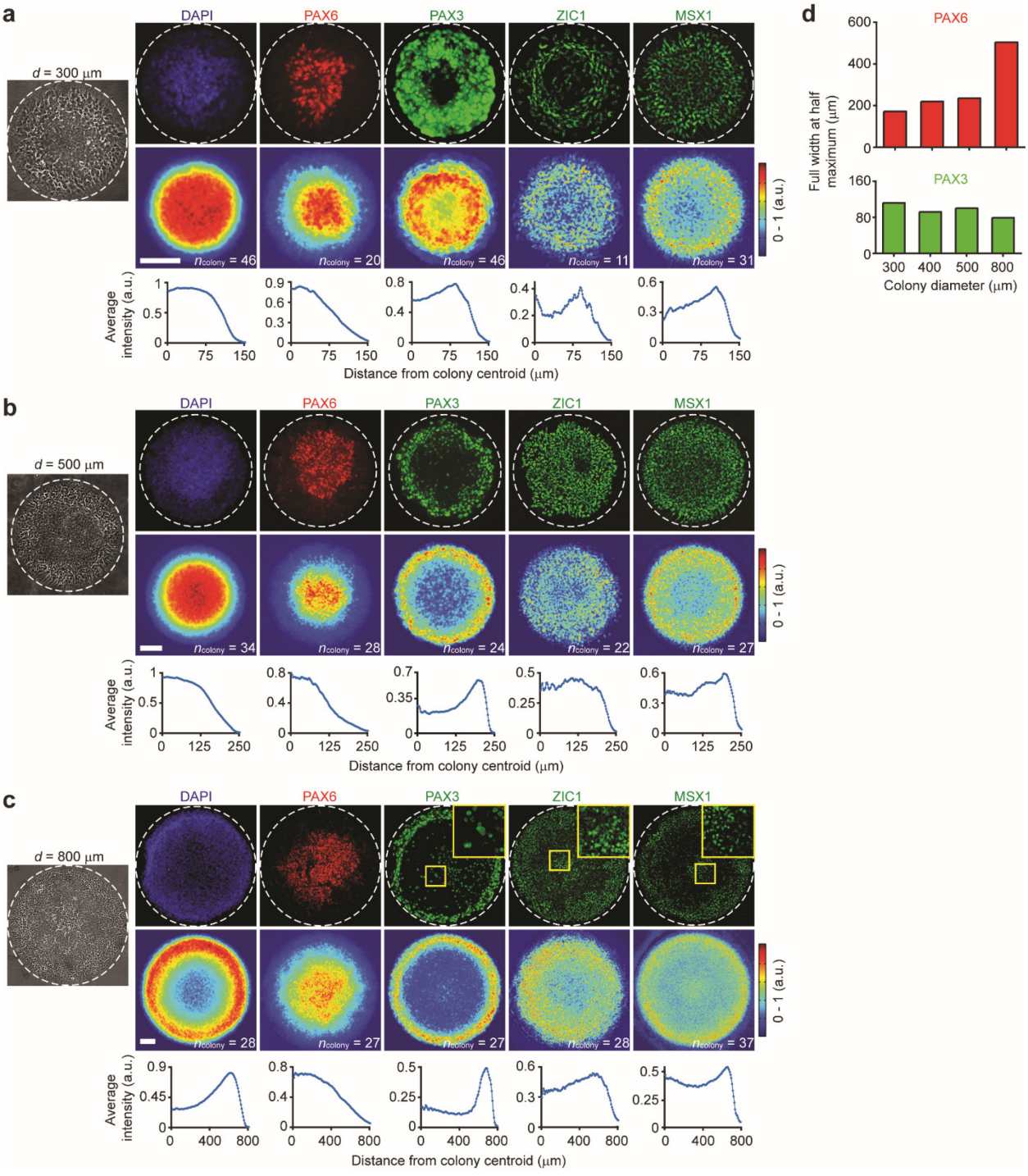

Figure 2-7 Effect of colony size on self-organized neuroectoderm patterning. (**a-c**) Representative phase contrast and immunofluorescence micrographs and average intensity maps showing cell colonies of different diameters (**a**: $d = 300$ μm; **b**: $d = 500$ μm; **c**: $d = 800$ μm) at day 9 stained for neuroepithelial marker PAX6 and neural plate border (NPB) markers PAX3, ZIC1 and MSX1 as indicated. DAPI counterstained nuclei. White dashed lines mark colony periphery. Zoomed-in

images in **c** are shown for boxed regions at colony central areas. Experiments were repeated three times with the similar results. Number of colonies analyzed were pooled from $n = 3$ independent experiments. Bottom plots show average fluorescence intensity of individual markers as a function of distance from colony centroid. Data were plotted as the mean. Scale bars, 100 μm. (**d**) Bar plots showing full width at half maximum (FWHM) for average normalized fluorescence intensity curves of PAX6 and PAX3 in **a-c**, respectively, as a function of colony diameter. hPS cells were plated on day 0 at 20,000 cells cm^{-2}.

We further examined neuroectoderm patterning in circular colonies with $d = 400$ μm under two other initial cell seeding density conditions (5,000 cells cm^{-2} and 30,000 cells cm^{-2}). A seeding density of 5,000 cells cm^{-2} led to abnormal neuroectoderm regionalization. Even though a notable number of $PAX6^+$ NE cells appeared at the colony center, $PAX3^+$, $ZIC1^+$ and $MSX1^+$ NPB cells were evident across entire colonies without distinct spatial patterning (**Figure 2-8 a**). Plating cells at 30,000 cells cm^{-2} led to development of multilayered cellular structures by day 9, even though $PAX3^+$ NPB cells still appeared and formed a single peripheral layer enveloping colony top surface (**Figure 2-8 b**). Overall, we identified micropatterned circular colonies with $d = 300$ - 500 μm and an initial cell seeding density of 20,000 cells cm^{-2} as the most suitable condition for *in vitro* modeling of neural induction (referred to henceforth as the 'default neural induction' condition).

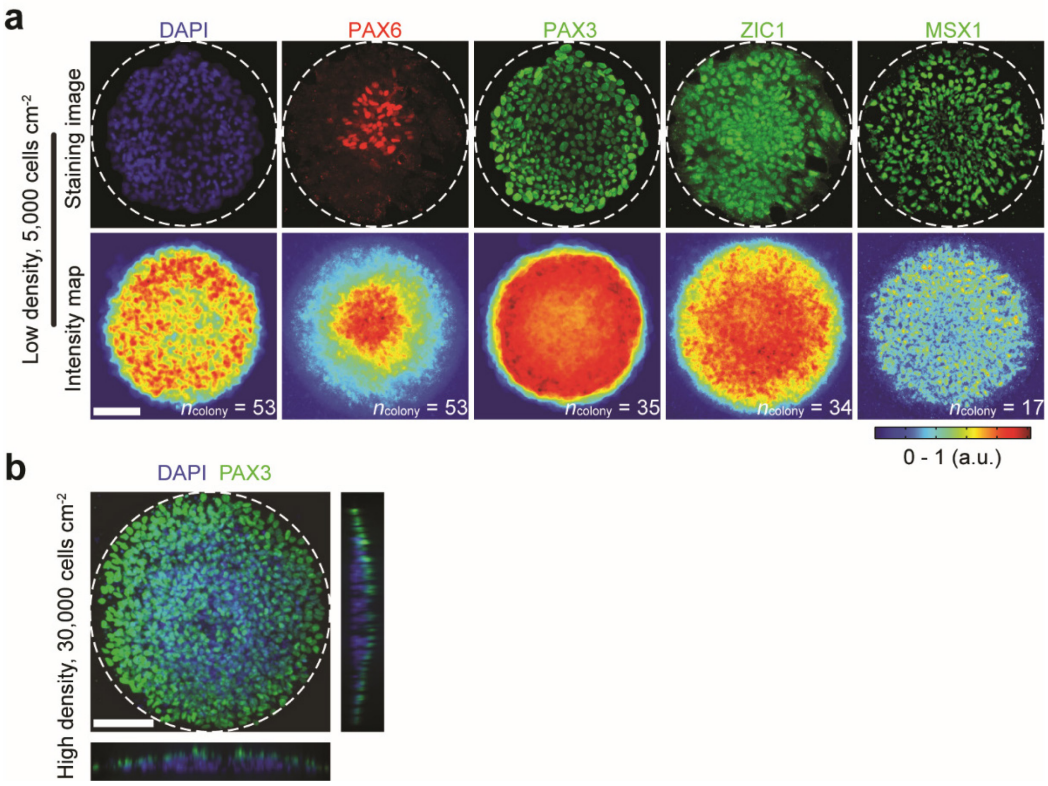

Figure 2-8 Effect of cell seeding density on self-organized neuroectoderm patterning. (**a**) Representative immunofluorescence micrographs and average intensity maps for cell colonies at day 9 when hPS cells were plated on day 0 at a low density of 5,000 cells cm^{-2}. Colonies were stained for neuroepithelial marker PAX6 and neural plate border (NPB) markers PAX3, ZIC1 and MSX1 as indicated. DAPI counterstained nuclei. White dashed lines mark colony periphery. Experiments were repeated three times with similar results. Number of colonies analyzed were pooled from $n = 3$ independent experiments. Data were plotted as the mean. Scale bar, 100 μm. (**b**) Representative confocal images demonstrating spatial distribution of $PAX3^+$ NPB cells in cell colonies at day 9 when hPS cells were plated on day 0 at a high density of 30,000 cells cm^{-2}. Experiments were repeated three times with similar results. Scale bar, 100 μm. hPS cells were seeded at day 0 on circular adhesive patterns with a diameter of 400 μm.

We further conducted live-cell assays to examine the dynamics of NPB patterning using a SOX10::EGFP bacterial artificial chromosome hES cell reporter line (H9)[108]. SOX10 is a specifier gene for NC induction at the NPB in vertebrates[114]. Surprisingly, under the default neural induction condition, GFP^+ cells emerged first at colony periphery on day 6 and continuously increased its number there through day 7 and day 8 (**Figure 2-9**). This observation was further corroborated by immunofluorescence analysis to examine initial appearances and

spatial distributions of $PAX6^+$ NE and $PAX3^+$ NPB cells, respectively, in micropatterned colonies at different days (**Figure 2-10**). $PAX3^+$ NPB cells were first observed at the colony periphery on day 4, while $PAX6^+$ NE cell were first observed at colony center on day 6. Together, the time course of expression of the NPB markers PAX3 and NC marker SOX10 in micropatterned hES cell colonies is consistent with mouse embryo development *in vivo*[114-116].

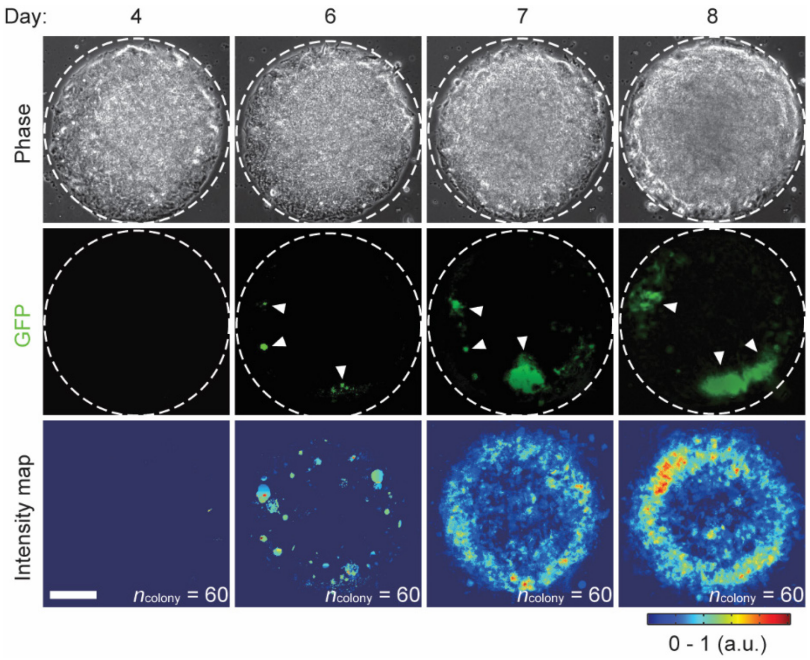

Figure 2-9 Dynamic expression of SOX10 during self-organized neuroectoderm patterning. Representative phase contrast and fluorescence images and average intensity maps from live cell assays using SOX10:EGFP hES cells. White dashed lines mark colony periphery. White arrowheads mark GFP^+ cells at colony border on day 6. Experiments were repeated three times with similar results. Number of colonies analyzed were pooled from $n = 3$ independent experiments. Data were plotted as the mean. Scale bars in **b-d**, 100 μm.

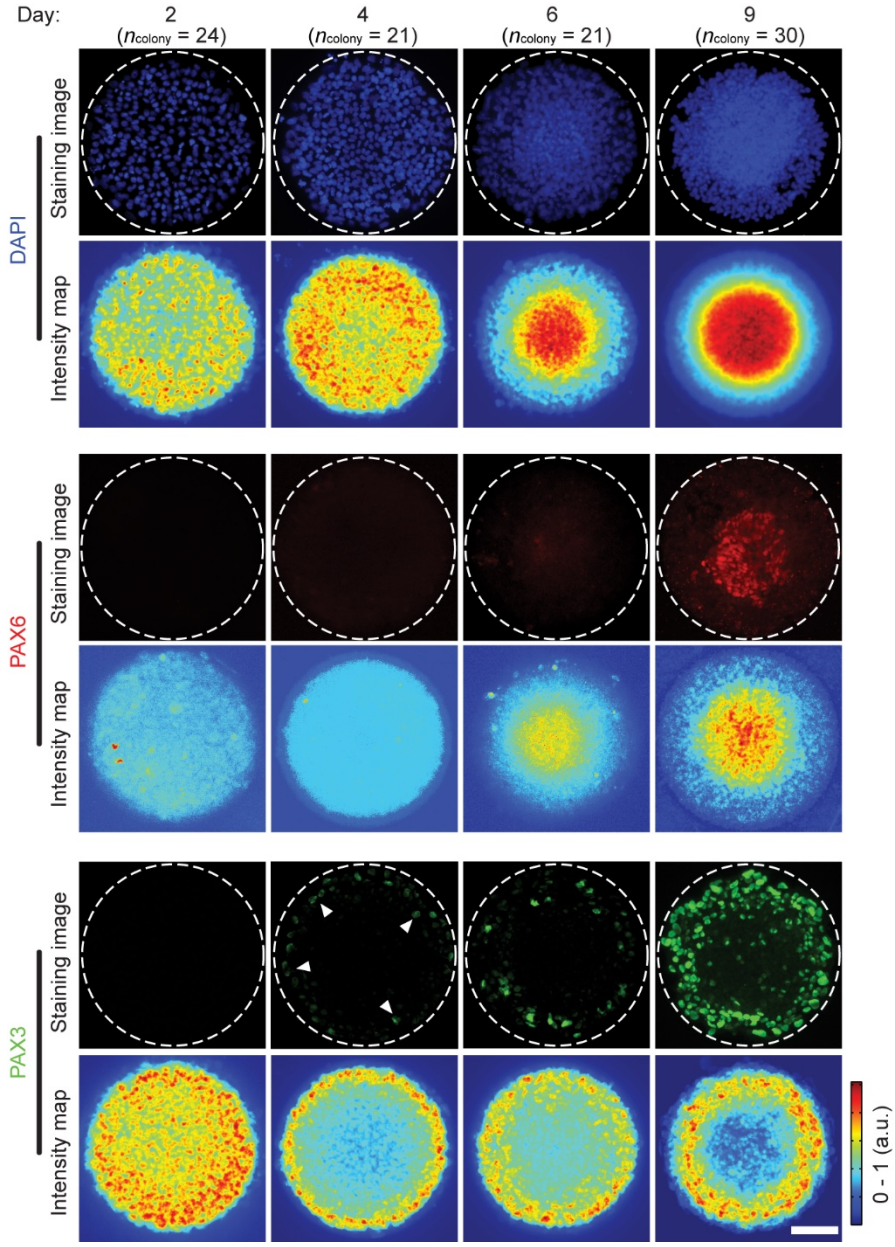

Figure 2-10 Dynamic expression of cell lineage markers during self-organized neuroectoderm patterning. Cells were stained for the neuroepithelial marker PAX6 and the neural plate border (NPB) marker PAX3 at day 2, 4, 6, and 9. DAPI counterstained nuclei. White dashed lines mark colony periphery. White arrowheads mark appearance of $PAX3^{+}$ NPB cells at colony border on day 4. Experiments were repeated three times with similar results. Average intensity maps show spatial distributions of marker intensities. Number of colonies analyzed were pooled from $n = 3$ independent experiments. Data were plotted as the mean. Scale bar, 100 μm.

To examine a possible role of cell sorting in neuroectoderm patterning, live-cell imaging was conducted for tracking cell migratory behaviors between day 2 - 4 in micropatterned colonies. Our results revealed that migration of cells, regardless whether located at colony central or peripheral regions, was very limited under the default neural induction condition, with an average radial displacement < 20 μm between day 2 - 4 (**Figure 2-11**). Furthermore, cell migratory behaviors could be simulated well using an unbiased random walk model (**Figure 2-11).** Thus, cell sorting was unlikely responsible for emergent regional neuroectoderm patterning in micropatterned colonies. Together, our data support that autonomous regionalization of NE and NPB cells during emergent neuroectoderm patterning can be attributed to cell fate-determinant, position-dependent information perceived by differentiating cells that dictates bifurcation dynamics of NE and NPB lineage commitments.

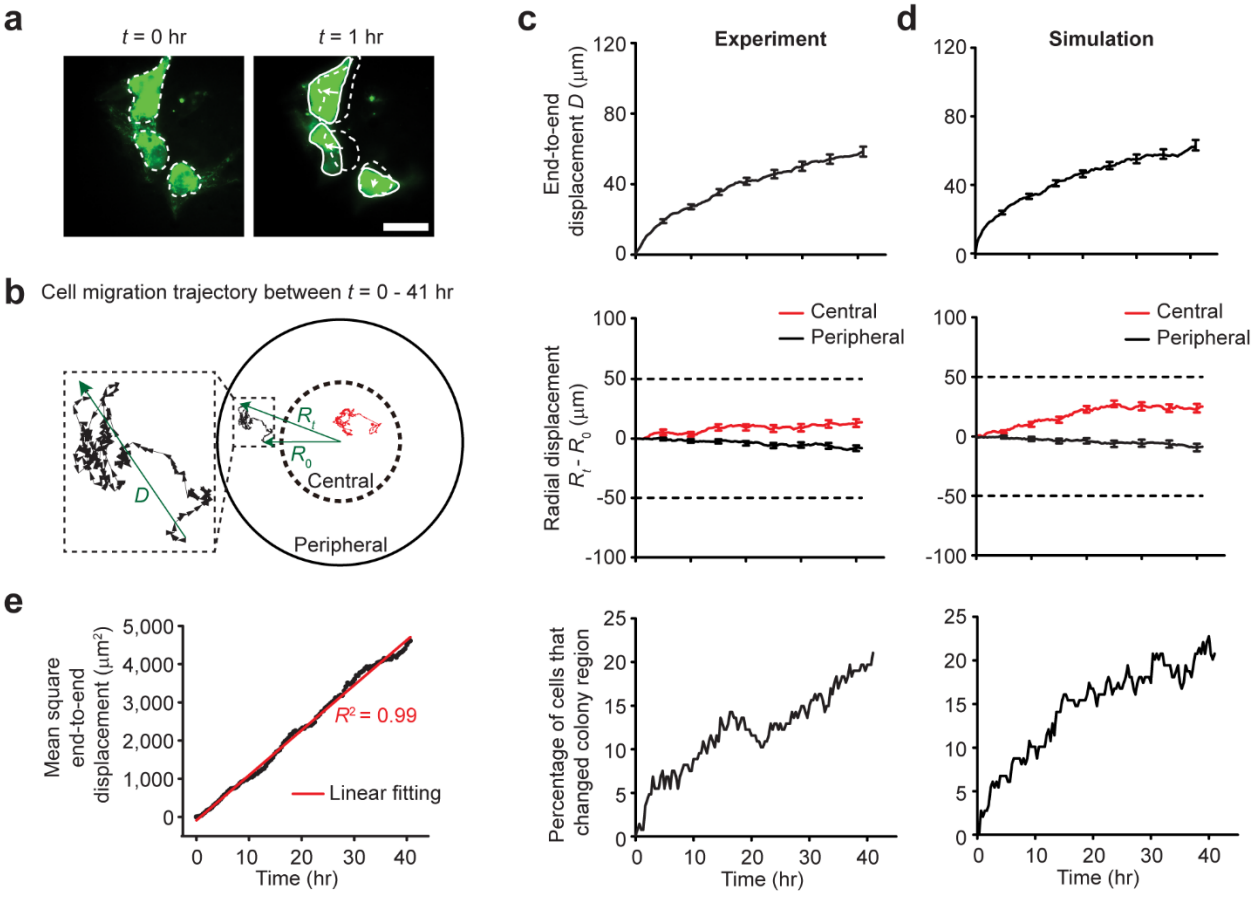

Figure 2-11 Cell migration during neuroectoderm patterning. Migration of CellTracker labeled hPS cells was recorded every 20 min starting from day 2 (t = 0 hr) till day 4 (t = 41 hr). If labeled cells divided during tracking, one of daughter cells was randomly selected for continuous tracking. (**a**) Fluorescence micrographs showing CellTracker labeled cells at t = 0 hr and t = 1 hr. White dashed and solid lines mark cell boundaries at t = 0 hr and t = 1 hr, respectively. White arrows mark cell displacements. Scale bar, 40 μm. (**b**) Migration trajectories for two individual cells in colony central (red) and peripheral (black) regions, respectively, between t = 0 - 41 hr. D denotes end-to-end cell displacement, and R_t denotes cell radial position from colony centroid. R_t - R_0 represents radial displacement during cell migration. (**c&d**) Experimental (**c**) and simulation (**d**) results showing end-to-end displacement D, radial displacement R_t - R_0, and percentage of cells switching between 'central' and 'peripheral' regions as a function of time. For radial displacement, cells were divided into two groups based on their radial positions at t = 0 hr (R_0) ('central': $0 \leq R_0 \leq$ 100 μm; 'peripheral': 100 < $R_0 \leq$ 200 μm). The slight difference in radial displacement R_t - R_0 between 'central' and 'peripheral' cells was due to geometric confinement from colony boundary preventing cells from passing across. n_{cell} = 153 from n = 2 independent experiments with n_{colony} > 15 per experiment. Data were plotted as the mean ± s.e.m. (**e**) Mean square end-to-end displacement D^2 as a function of time. Red curve shows linear fitting.

The micropatterned hPS cell culture system, even though efficient for deriving neuroectoderm tissues with proper NE / NPB regionalization, does not contain non-neural ectoderm or mesenchymal tissues, which may play important roles in instructing neuroectoderm tissue formation *in vivo* [95, 117, 118]. Nonetheless, there are well documented tissue isolation studies using *in vivo* models that support neural induction as an autonomous process [119]. The origin of NPB cells is also believed to arise from neural but not epidermal ectoderm [114, 116]. Altogether, the micropatterned hPS cell culture system reported here is useful for studying self-organizing principles involved in autonomous patterning and regionalization of neuroectoderm tissues.

In summary, I have utilized bioengineering tools such as microcontact printing to establish 2D colonies of hPS cells with defined shapes and sizes. Pre-patterned geometrical confinement induces emergent patterning of hPS cells, mimicking neuroectoderm regionalization during early neurulation. Specifically, under neural induction condition, hPS cells differentiate and gradually self-organize into a radial symmetrical pattern of NE and NPB cells, with NE cells localized at the colony center and NPB cells accumulating at the colony border. The hPS cell-based neural induction model could be leveraged for developing high-throughput toxicological studies and drug screening platforms for prevention and treatments of neural tube defects.

Chapter 3

Mechanics-Guided Cell Fate Patterning in a Human Pluripotent Stem Cell-Derived Neuroectoderm Model

The major content of this chapter is reproduced from my previously published paper: "Mechanics-guided embryonic patterning of neuroectoderm tissue from human pluripotent stem cells." in Nature Materials, 2018 [93].[†]

3.1 Introduction

One of the enduring mysteries of cell and developmental biology is tissue morphogenesis and patterning, where embryonic cells act in a coordinated fashion to shape the body plan of multicellular animals[120-124]. During early human development, embryonic cells continue to divide, differentiate and organize into embryonic structures through morphogenesis. Morphogenetic events generate local mechanical perturbation and are accompanied by changes in cell shape and force[123, 125]. It has been reported that mechanics plays an important role in

[†] Research presented in this chapter has received assistance from Dr. Yubing Sun (cell culture, design differentiation assay), Ms. Agnes Resto-Irizarry (imaging processing), and Dr. Koh Meng Aw Yong, Dr. Yi Zheng, Dr. Shinuo Weng, and Dr. Yue shao (qRT-PCR). I would also like to thank Dr. Jianping Fu for his supervision and Dr. Allen Liu for his comments on the research presented in this chapter.

various developmental events including anterior-posterior patterning[126], left-right patterning[127] and amnion development[128, 129]. Failure of stem cell differentiation and morphogenesis, likely associated with abnormal cellular mechanical property changes, can result in abnormal embryonic or fetal development and birth defects. For example, amniotic band syndrome (ABS), which could result in limb defects, may be caused by weak mechanical properties and rupture of amniotic sac or lack of amniotic fluid [130].

As a highly conserved developmental event crucial for nervous system formation, neural induction, for example, leads to differentiation of the ectoderm into a patterned tissue, containing the neural plate (NP) and the epidermal ectoderm separated by the neural plate border (NPB) [110, 131]. Classic embryological studies of neural induction have unraveled the importance of graded developmental signaling mediated by diffusible signals including bone morphogenetic proteins (BMPs) in neuroectoderm patterning [95, 117, 118]. However, neural induction, like any tissue-scale morphogenetic event, occurs within the milieu of biophysical determinants including changes in shape, number, position, and force of cells [94, 131]. For example, the ectoderm becomes thickened in the dorsal region to form pseudostratified, columnar neuroepithelial (NE) cells in the prospective NP domain. Yet, it remains undetermined how these tissue-scale morphogenetic changes work in concert with classic developmental signaling events mediated by diffusible biochemical signals for proper spatial regulations of cell fate patterning during neural induction, largely due to the lack of controllable in vitro models that are compatible to mechanical manipulation.

Here, to understand the role of mechanical cues in neuroectoderm patterning, leveraging the hPSC-based neural induction models that were reported in chapter 2, I implemented various

mechanical stimulation and characterization tools such as PDMS micropost array and cell stretching device in this in vitro neural induction model to study the interaction and crosstalk between mechanical cues and classic developmental signaling such as BMP signaling to regulate NE and NPB lineage bifurcation.

3.2 Materials and methods

3.2.1 Traction force measurement.

Traction force was analyzed using PDMS micropost arrays (PMAs) as described previously[105]. Briefly, PMAs were first prepared for cell attachment using microcontact printing to coat micropost top surfaces with vitronectin as described previously[105]. To quantify traction forces of micropatterned hPS cell colonies or single hPS cells, microcontact printing was used to define circular adhesive patterns of different sizes. PMAs were labeled with Δ^9-DiI (5 μg mL^{-1}; Invitrogen) in distilled water for 1 hr. After microcontact printing, protein adsorption to all PDMS surfaces not coated with vitronectin was prevented by incubating in 0.2% Pluronics F127 NF solution (BASF) for 30 min.

Live cell imaging was conducted using an inverted epifluorescence microscope (Zeiss Axio Observer Z1) enclosed in an environmental incubator (XL S1 incubator) maintaining cell culture at 37 °C and 5% CO_2. Images of micropost tops were recorded using a 40 × (for single cells) or 20 × (for cell colonies) objective (Carl Zeiss MicroImaging). All images were recorded at day 4 and were analyzed using a custom-developed MATLAB program (MathWorks), as described previously[132], to obtain traction force maps associated with each image. To determine average traction stress maps for micropatterned hPS cell colonies, individual traction force maps were first adjusted to the same size before being stacked together to obtain average

traction stress maps. To plot average traction stress as a function of distance from colony centroid, circular hPS cell colonies were first divided into 20 concentric zones with equal widths. The average traction stress in each concentric zone was then calculated and plotted against the mean distance of the concentric zone from colony centroid.

3.2.2 Microfluidic cell stretching device.

The microfluidic cell stretching device was comprised of a PDMS structural layer, a PDMS inlet block, and a glass coverslip. The PDMS structural layer, which contained a microfluidic network for applying pressures to simultaneously activate 64 pressurization compartments to induce PDMS membrane deformation, was fabricated using soft lithography. Briefly, PDMS prepolymer containing PDMS base monomer and curing agent (10:1 *w* / *w*) was spin coated on a silicon mold generated using conventional microfabrication techniques including photolithography and DRIE. The PDMS layer was thermally cured by baking at 110 °C for at least 24 hr before peeled from the silicon mold. An inlet for fluid connections was then punched into the PDMS structural layer using a 1 mm biopsy punch (Fisher Scientific). Both the coverslip and PDMS structural layer were briefly cleaned with 100% ethanol (Fisher Scientific) and blown dry under nitrogen before treated with air plasma (Plasma Prep II; SPI Supplies) and bonding together. Separately, another PDMS block was prepared, and an inlet for fluid connection was punched into the PDMS block with a 0.5 mm biopsy punch. After both treated with air plasma, the PDMS block and the PDMS structural layer were bonded together with their fluid inlets aligned manually. The competed microfluidic cell stretching device was baked at 110 °C for at least another 24 hr to ensure robust bonding between different layers.

To apply continuous stretching to the central zone of micropatterned hPS cell colonies, microcontact printing was performed to print circular adhesive patterns with a diameter of 400 μm onto the deformable PDMS membrane on top of pressurization compartments (with a diameter of 200 μm) in a custom designed microfluidic cell stretching device. To this end, a custom desktop aligner designed for fabrication of multilayer microfluidic devices was used[133]. Briefly, the vitronectin-coated PDMS stamp and the microfluidic cell stretching device were mounted onto the top and bottom layer holders of the aligner, respectively. Under inspection with a digital microscope, the X / Y / θ stage holding the bottom layer holder was adjusted for alignment of the PDMS stamp and the microfluidic cell stretching device. After alignment, the PDMS stamp was pressed to transfer vitronectin from the stamp to the deformable PDMS membrane on top of pressurization compartments.

Deionized water was injected into the microfluidic cell stretching device before applying pressure through a microfluidic pressure pump (AF1, Elveflow). Software (Elveflow Smart Interface) was used for programming the pressure pump for continuous cell stretching with a square-wave pattern (pulse width of 2 hr, period of 4 hr, and 50% duty cycle).

Detailed fabrication protocol is in **Appendix C**.

3.2.3 RNA isolation and quantitative reverse-transcription PCR (qRT-PCR) analysis.

Total RNA was isolated from cells using the RNeasy kit (Qiagen). Quantitative reverse-transcription PCR (qRT-PCR) was performed and monitored using a CFX Connect SYBR Green PCR Master Mix system (Bio-Rad). Human TBP primers were used as an endogenous control for relative quantifications. Primers are listed in **Appendix D**. Samples in which no expression was detected were given an arbitrary Ct value of 40. All analyses were performed with at least 3

biological replicates and 3 technical replicates. Relative expression levels were determined by calculating $2^{-\Delta\Delta Ct}$ with the corresponding s.e.m.

3.2.4 Pharmacological treatment.

Blebbistatin was used to inhibit actomyosin contractility. To this end, blebbistatin (10 μM in DMSO; Cayman Chemical) was supplemented to the culture medium from day 1 till cell fixation. To modulate BMP signaling, recombinant human BMP4 (25 ng mL^{-1}; R&D Systems) was supplemented to the neural induction medium.

3.2.5 Statistics.

Statistical analysis was performed using Excel (Microsoft). The significance between two groups was analyzed by a two-tailed Student *t*-test. In all cases, a *P* value of less than 0.05 was considered significant.

3.3 Results and discussion

Gradual accumulation of hPSCs at colony center (**Figure 2-3**) suggests cell rearrangement and dynamic morphogenetic processes. Indeed, micropatterned hPSC colonies stained for ZO-1 for visualization of cell-cell junctions revealed that at day 4 under the default neural induction condition, cells at the colony periphery displayed a greater projected area than at the central region (**Figure 3-1 a & b**). Compared with those at the colony center, cells at the colony periphery also displayed greater intracellular cytoskeletal contractility, as revealed by stronger staining for phosphorylated myosin and greater traction stress quantitated using PDMS micropost force sensors[105] (**Figure 3-1 a & c**). Supplementing neural induction medium with blebbistatin (10 μM), which inhibits myosin motor activity and thus cytoskeletal contractility,

effectively eliminated spatial differences in projected area or traction stress between colony peripheral and central regions at day 4 (**Figure 3-1 a-c**). Importantly, even though NE and NBP cells still appeared at day 9 under blebbistatin treatment, proper neuroectoderm regionalization was severely impaired, with abundant PAX3$^+$, ZIC1$^+$ and MSX1$^+$ NPB cells randomly distributed across entire colonies (**Figure 3-1 d**).

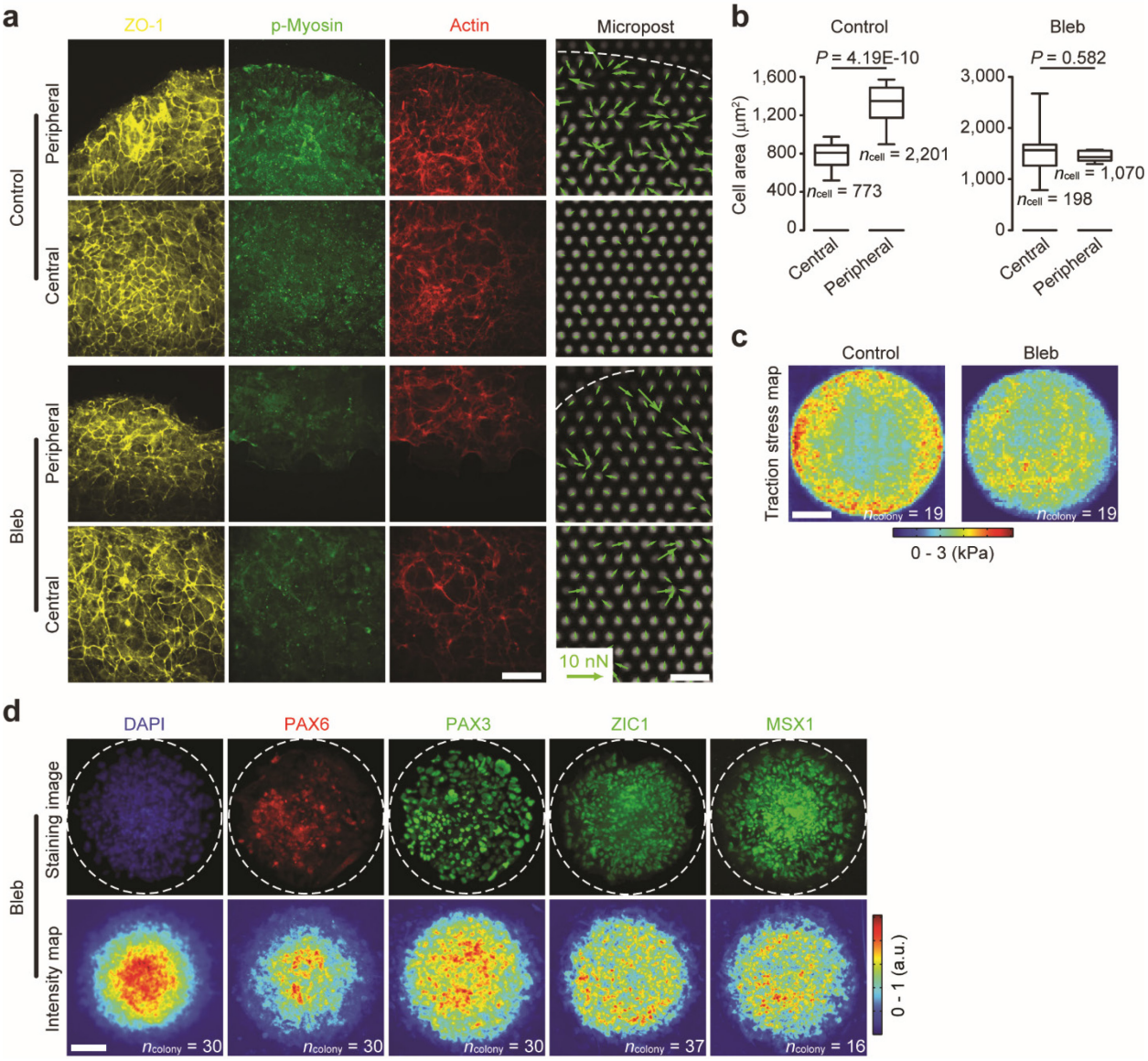

Figure 3-1 Self-organization of morphogenetic factors controls neuroectoderm patterning. **(a)** Representative fluorescence images showing staining for ZO-1, phosphorylated myosin (p-myosin)

and actin, as well as micropost sensors at the colony peripheral and central regions at day 4. hPS cells were cultured in neural induction medium supplemented with either DMSO (control) or blebbistatin (Bleb; 10 μM). Circular colonies were divided into 2 concentric zones ("central" *vs.* "peripheral") with equal widths. White dashed lines mark colony periphery. Traction force vectors were superimposed onto individual micropost force sensors. Experiments were repeated three times with similar results. Scale bars, 40 μm (fluorescence micrographs) and 10 μm (micropost images). (**b**) Box-and-whisker plots showing projected cell spreading area at day 4 under different conditions as indicated (box: 25 - 75%, bar-in-box: median, whiskers: 1% and 99%). Number of colonies analyzed were pooled from $n = 3$ independent experiments. *P* values were calculated using unpaired, two-sided Student's *t*-tests. (**c**) Maps showing spatial distribution of traction stress quantitated using micropost force sensors at day 4 under culture conditions as indicated (see **Methods**). Number of colonies analyzed were pooled from $n = 3$ independent experiments. Data were plotted as the mean. Scale bar, 100 μm. (**d**) Representative immunofluorescence micrographs and average intensity maps showing colonies at day 9 stained for PAX6, PAX3, ZIC1 and MSX1. DAPI counterstained nuclei. White dashed lines mark colony periphery. Experiments were repeated three times with similar results. Number of colonies analyzed were pooled from $n = 3$ independent experiments. Data in intensity maps were plotted as the mean. Scale bar, 100 μm.

Our results in **Figure 3-1** suggested critical roles of morphogenetic cues in mediating neuroectoderm patterning with proper regionalization. Neural induction *in vivo* has been shown to be mediated through graded BMP signaling [22, 95, 117, 118]. Specifically, this BMP signaling gradient provides positional information in the ectoderm, with high BMP activity promoting epidermal differentiation, low BMP for NP development, and intermediate BMP for NPB specification[22, 95, 117, 118]. Indeed, we observed strong correlations between spatial regulations of cell shape, cytoskeletal contractility and BMP activity at day 4 under the default neural induction condition. Most cells at the colony periphery showed prominent nuclear staining of phosphorylated SMAD 1/5 (p-SMAD 1/5), a downstream target of BMP-SMAD signaling, whereas much fewer cells at colony central area were p-SMAD 1/5 nuclear positive (**Figure 3-2**). Interestingly, blebbistatin treatment or plating cells at 5,000 cells cm^{-2} rescued BMP activity at colony central area on day 4 (**Figure 3-2**), consistent with their effects on promoting NPB differentiation at colony central region.

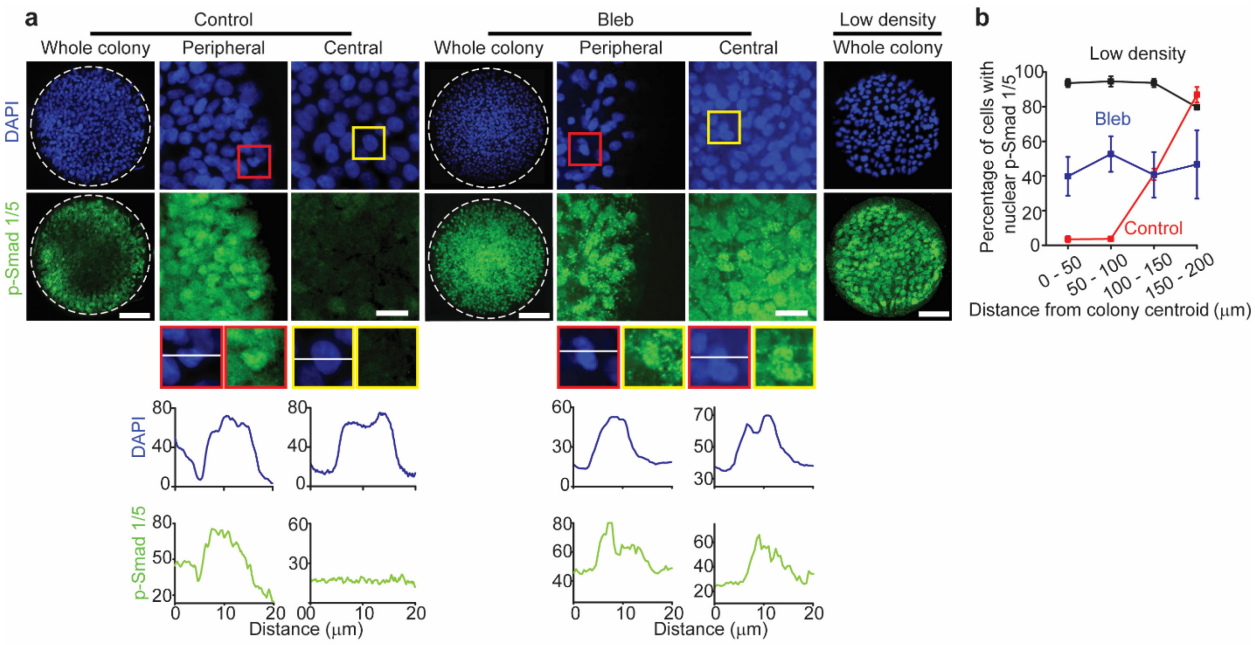

Figure 3-2 Mechanically guided emergent neuroectoderm patterning is mediated by BMP-Smad signaling. (**a**) Representative immunofluorescence images showing whole colonies or central and peripheral zones of micropatterned colonies at day 4 stained for phosphorylated Smad 1/5 (p-Smad 1/5) as indicated. DAPI counterstained nuclei. hPS cells were plated at either 20,000 cells cm^{-2} (control) or 5,000 cell cm^{-2} (low density) and were cultured in the neural induction medium supplemented with either DMSO or blebbistatin (Bleb) from day 1 - 4 as indicated. Red and yellow rectangles highlight selected peripheral and central regions of colonies, respectively, where fluorescence intensities of DAPI and p-Smad 1/5 were measured along white solid lines drawn across these selected areas. Scale bars, 100 μm (whole colony) and 40 μm (peripheral and central zones). (**b**) Percentage of cells with nuclear p-Smad 1/5 as a function of distance from colony centroid under different culture conditions as indicated. Based on the distance of nuclei from colony centroid, cells were grouped into 4 concentric zones with equal widths as indicated. Data were obtained from images in **a** and plotted as the mean ± s.e.m.

To specifically examine the functional roles of cell shape and cytoskeletal contractility in regulating BMP activation, microcontact printing was applied to obtain patterned circular single hES cells with prescribed spreading areas. Of note, cytoskeletal contractility of patterned single hES cells correlated positively with spreading area (**Figure 3-3**). Importantly, the percentage of patterned single hES cells with dominant nuclear staining of p-SMAD 1/5 also increased with spreading area (**Figure 3-3**). Furthermore, qRT-PCR analysis revealed greater expression levels of BMP target genes *MSX1*, *ID1*, and *ID3* in patterned single hES cells with greater spreading

areas (**Figure 3-4 a-c**). Similar observations regarding BMP target genes were also obtained when seeding hES cells on vitronectin-coated flat PDMS surfaces at different plating densities to effectively modulate spreading area and cytoskeletal contractility (**Figure 3-4 d-f**).

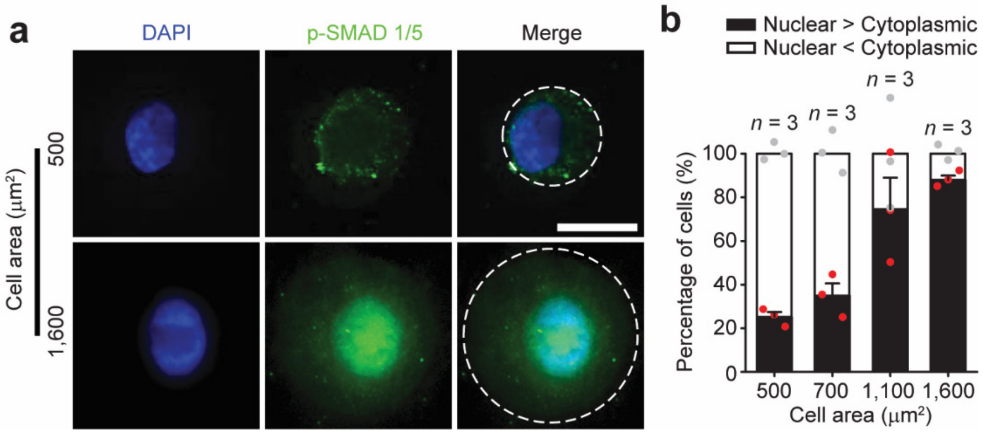

Figure 3-3 BMP-SMAD activity is dependent on cell shape. **(a)** Representative immunofluorescence micrographs showing patterned circular single hPS cells with defined spreading areas (500 μm^2 *vs.* 1,600 μm^2) stained for p-SMAD 1/5. White dashed lines mark cell shape. Scale bar, 20 μm. Experiments were repeated three times with similar results. (**b**) Bar plot showing percentages of cells with dominant nuclear or cytoplasmic p-SMAD 1/5 as a function of cell spreading area. $n = 3$ independent experiments. Data were plotted as the mean ± s.e.m.

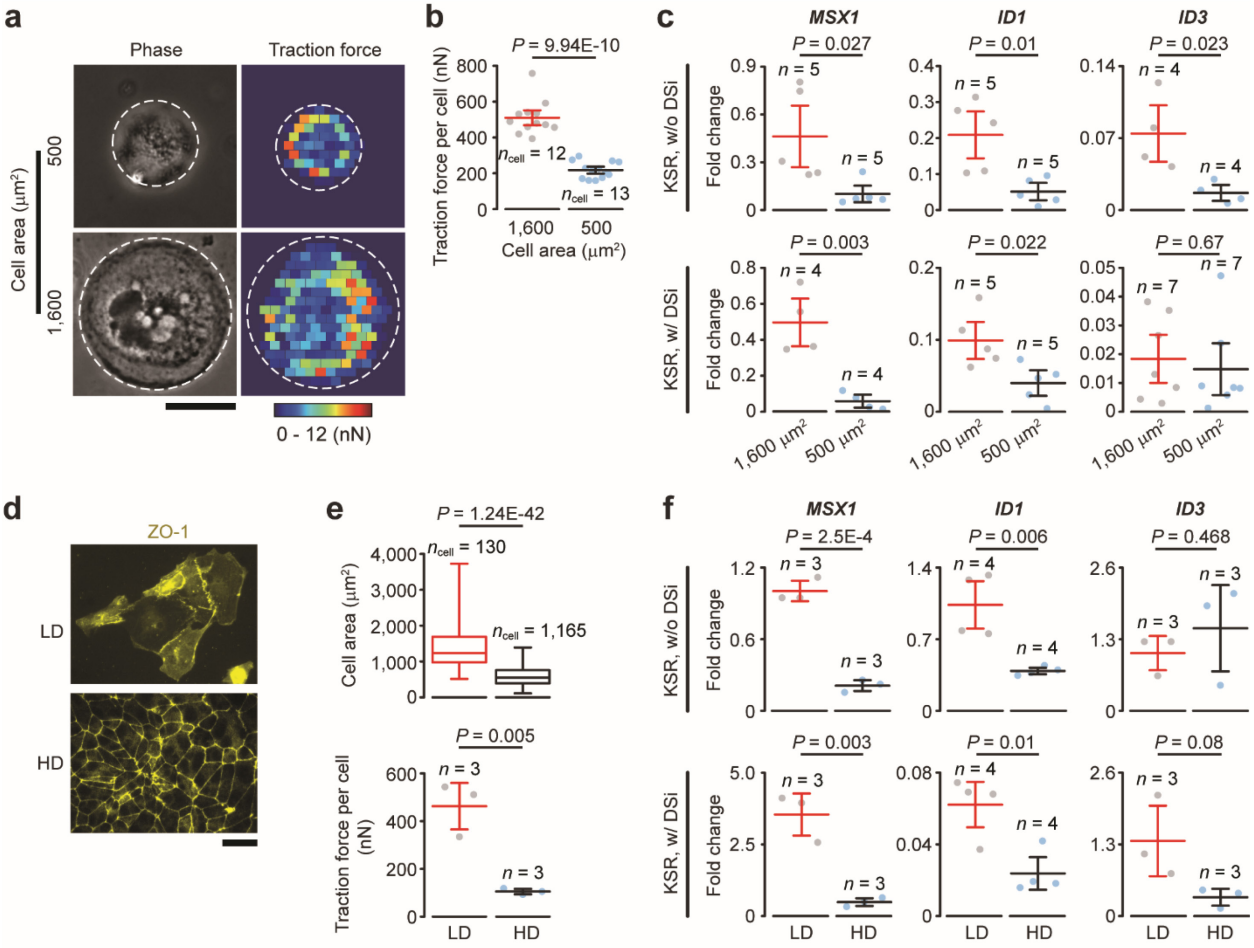

Figure 3-4 Traction force and expression of BMP target genes depend on cell spreading area. (**a**) Representative phase contrast images and traction force maps of micropatterned circular single hPS cells with defined spreading areas (500 μm^2 *vs.* 1,600 μm^2). hPS cells were patterned on flat PDMS surfaces (for immunofluorescence and qRT-PCR analyses) or PDMS micropost arrays (for traction force measurements). Scale bar, 20 μm. Experiments were repeated twice with similar results. (**b**) Dot plots showing traction force per cell as a function of cell spreading area. Data were pooled from $n = 2$ independent experiments. Error bars, mean ± s.e.m. (**c**) Dot plots showing expression of BMP4 target genes *MSX1*, *ID1*, and *ID3* as a function of cell spreading area. Error bars, the mean ± s.e.m. (**d**) Representative immunofluorescence micrographs showing hPS cells seeded on vitronectin coated coverslips stained for ZO-1. hPS cells were plated at either 200,000 cells cm^{-2} (high density, or HD) or 10,000 cell cm^{-2} (low density, or LD). Scale bar, 20 μm. Experiments were repeated three times with similar results. (**e**) Box-and-whisker plot showing projected cell area (box: 25-75%, bar-in-box: median, and whiskers: 1% and 99%) and dot blot showing traction force per cell as a function of cell seeding density. Error bars in dot plot, the mean ± s.e.m. Data were pooled from $n = 3$ independent experiments. (**f**) Dot plots showing expression of BMP4 target genes *MSX1*, *ID1*, and *ID3* as a function of cell seeding density. Error bars, the mean ± s.e.m. For **c** & **f**, cells were cultured in KSR medium supplemented with or without the dual Smad inhibitors (DSi) for 6 hr before RNA collection. All *P* values were calculated using unpaired, two-sided Student's *t*-tests.

To further investigate the causal link between cell shape and mechanical force and neuroectoderm patterning, a custom designed microfluidic cell stretching device was developed and implemented for stretching central regions of micropatterned hES cell colonies (**Figure** 3-5) [134]. Continuous stretching with a square-wave pattern (pulse width of 2 hr and period of 4 hr) and a 100% stretch amplitude was applied starting from day 2 under the default neural induction condition (**Figure 3-6**). Indeed, mechanical stretching enhanced cytoskeletal contractility at colony central region, as reflected by stronger staining of phosphorylated myosin and actin filaments, as compared to unstretched controls (**Figure 3-5**). Furthermore, stretching of colony central area effectively rescued nuclear p-SMAD 1/5 and thus BMP activity at colony central region (**Figure 3-5**). By day 8, a significant number of $PAX3^+$ NPB cells were evident at colony center, whereas NE differentiation was completely inhibited there (**Figure 3-5**). Together, these results unambiguously demonstrate that cell shape and mechanical force can directly activate BMP-SMAD signaling and thus repress NE but promote NPB differentiation. Our data strongly support that mechanical self-organization during emergent neuroectoderm patterning can effectively provide instructive signals to guide genetic and cell fate patterning at the level of individual cells and consequently strengthen spatial patterning of NE and NPB cells.

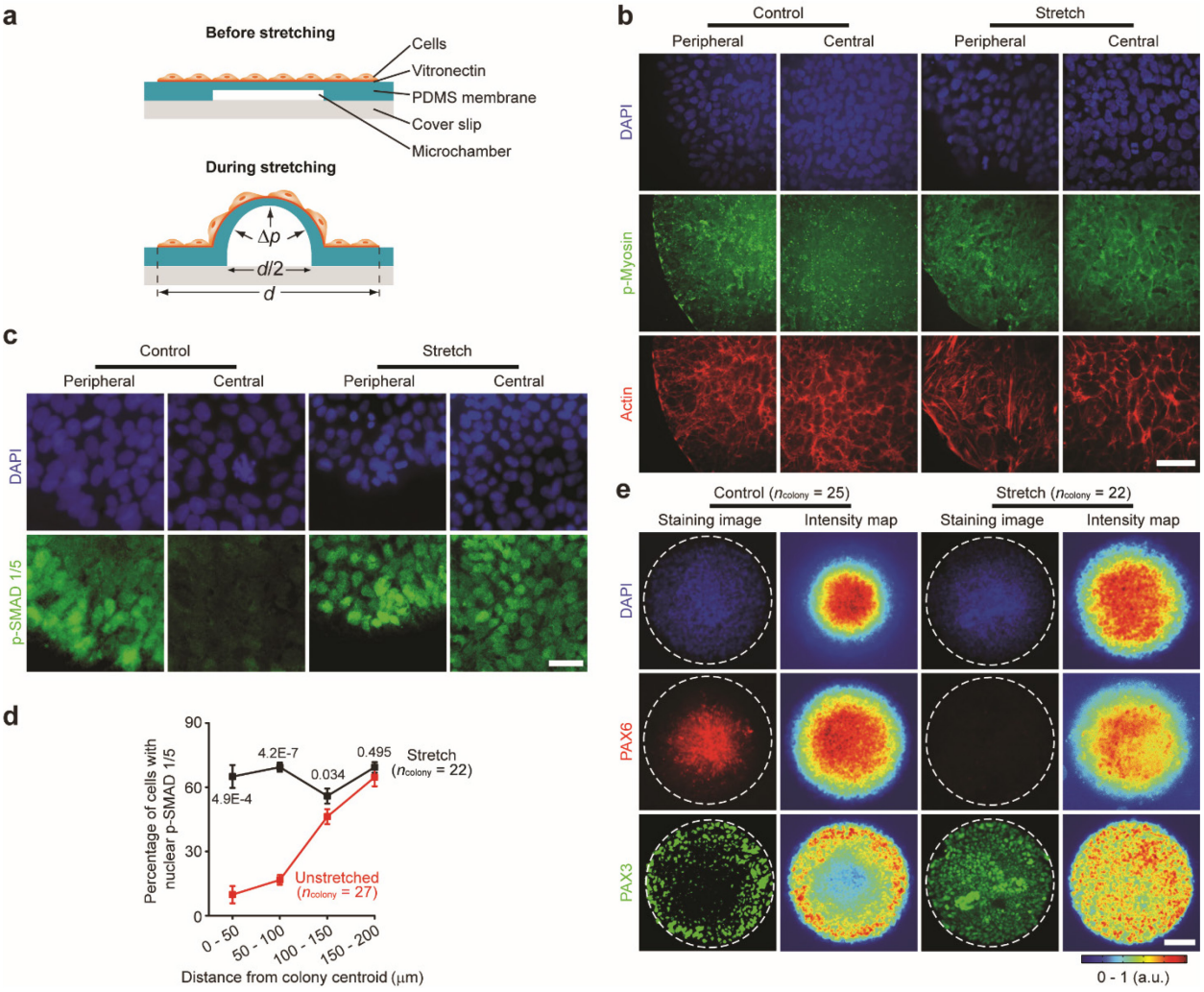

Figure 3-5 Mechanical force is sufficient for activating BMP-SMAD signaling and inducing neural plate border cell differentiation. (**a**) Schematic of a microfluidic device to apply stretching forces to central zones of micropatterned hPS cell colonies. (**b**) Representative fluorescence micrographs showing central and peripheral zones of unstretched (control) and stretched (stretch) micropatterned colonies at day 4 stained for phosphorylated myosin (p-myosin) and actin. DAPI counterstained nuclei. Scale bar, 40 μm. Experiments were repeated three times with the similar results. (**c**) Representative immunofluorescence images showing central and peripheral zones of unstretched (control) and stretched (stretch) micropatterned colonies at day 4 stained for phosphorylated SMAD 1/5 (p-SMAD 1/5). DAPI counterstained nuclei. Scale bar, 40 μm. Experiments were repeated four times with similar results. (**d**) Percentage of cells with nuclear p-SMAD 1/5 as a function of distance from colony centroid under stretch and unstretched control conditions as indicated. Based on distance of nuclei from colony centroid, cells were grouped into 4 concentric zones with equal widths as indicated. Number of colonies analyzed were pooled from $n = 4$ independent experiments. Data were plotted as the mean ± s.e.m. P values were calculated between stretch and unstretched control conditions using unpaired, two-sided Student's t-tests. (**e**) Representative immunofluorescence micrographs and average intensity maps showing unstretched (control) and stretched (stretch) colonies at day 8 stained for PAX6 and PAX3. DAPI

counterstained nuclei. White dashed lines mark colony periphery. Experiments were repeated three times with similar results. Number of colonies analyzed were pooled from $n = 3$ independent experiments. Data in intensity maps were plotted as the mean. Scale bar, 100 μm.

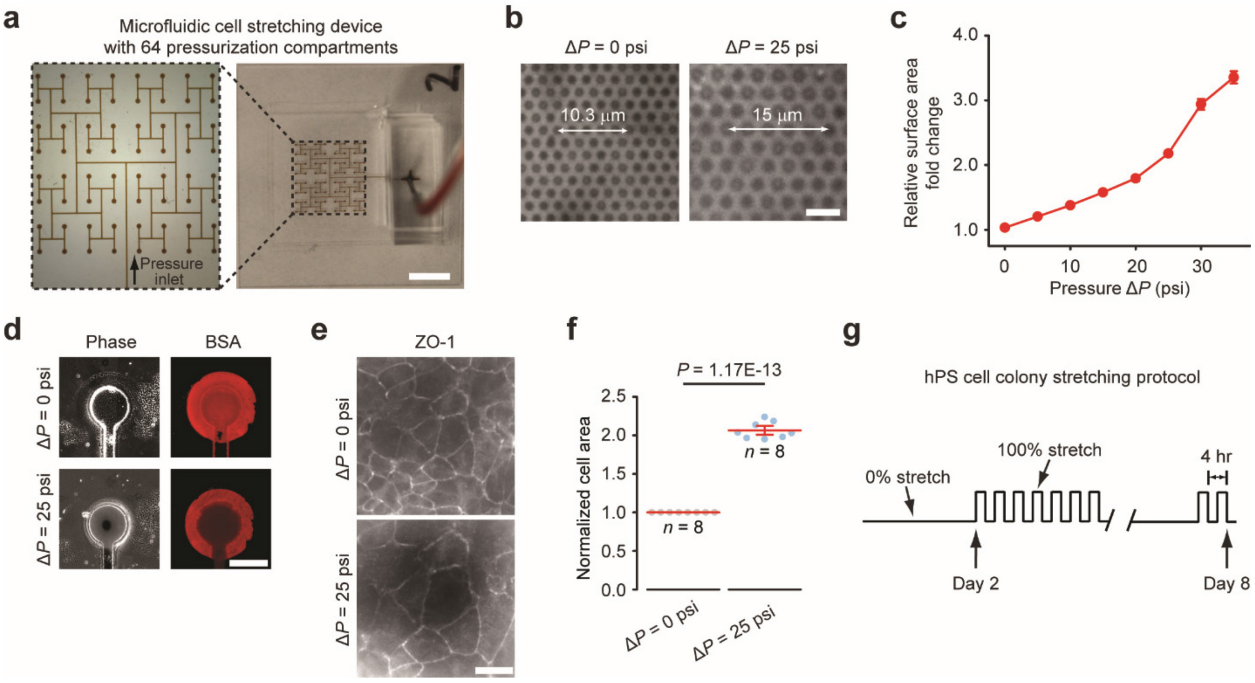

Figure 3-6 Microfluidic cell stretching device. (**a**) Photograph of the device including a microfluidic network to apply regulated pressures to simultaneously activate 64 pressurization compartments (200 μm in diameter) to induce PDMS membrane deformation and, consequently, mechanical stretching of hPS cells cultured on top of PDMS membranes. Scale bar, 5 mm. (**b**) Fluorescent images of fiducial markers on the PDMS membrane before and during stretching with $\Delta P = 25$ psi. Scale bar, 5 μm. (**c**) Plot of relative PDMS membrane surface area fold change as a function of ΔP. ΔP of 25 psi was used to achieve a 100% stretch amplitude. $n = 5$ independent experiments. Data were plotted as the mean ± s.e.m. (**d**) Phase contrast and fluorescent images showing a circular adhesive island with a diameter of 400 μm aligned and printed on top of the microfluidic pressurization compartment. For visualization, fluorescently labeled BSA was used for printing adhesive islands. Scale bar, 200 μm. (**e**) Immunofluorescence micrographs showing hPS cells seeded on the deformable PDMS membrane before and during cell stretching with $\Delta P =$ 25 psi. hPS cells were plated on day 0 at 20,000 cells cm^{-2}, and were stained at day 4 for ZO-1 before stretching. Scale bar, 30 μm. (**f**) Dot plot showing normalized cell area before and during stretching with $\Delta P = 25$ psi. $n = 8$ independent experiments. Error bars, the mean ± s.e.m. P values were calculated using unpaired, two-sided Student's t-tests. (**g**) hPS cell colony stretching protocol. Continuous stretching with a square-wave pattern (pulse width of 2 hr and period of 4 hr) and a 100% stretch amplitude was applied to the central zone of hPS cell colonies starting from day 2.

We next modified neural induction medium to further elucidate the role of BMP signaling in guiding neuroectoderm patterning. Specifically, modulating LDN concentration in

neural induction medium resulted in a dose-dependent BMP signaling response. With high-dose LDN (1 μM), BMP-SMAD signaling was completely repressed across entire colonies at day 4 (**Figure 3-7**). Without LDN supplementation, most cells across entire colonies showed prominent nuclear p-SMAD 1/5 at day 4, consistent with BMP activity-inducing properties of the KnockOut Serum Replacement (KSR) medium used in the default neural induction condition[135] (**Figure 3-7**). The results suggest that cell shape and contractility regulated cells' response to BMP signaling in micropatterned colony. BMP signaling was dependent on cell shape and contractility, under a proper LDN dosage (500 nM), large cells at colony periphery could respond to BMP signaling in KSR and activate pSmad1/5, while small cells at colony center are less sensitive and thus couldn't activate BMP signaling.

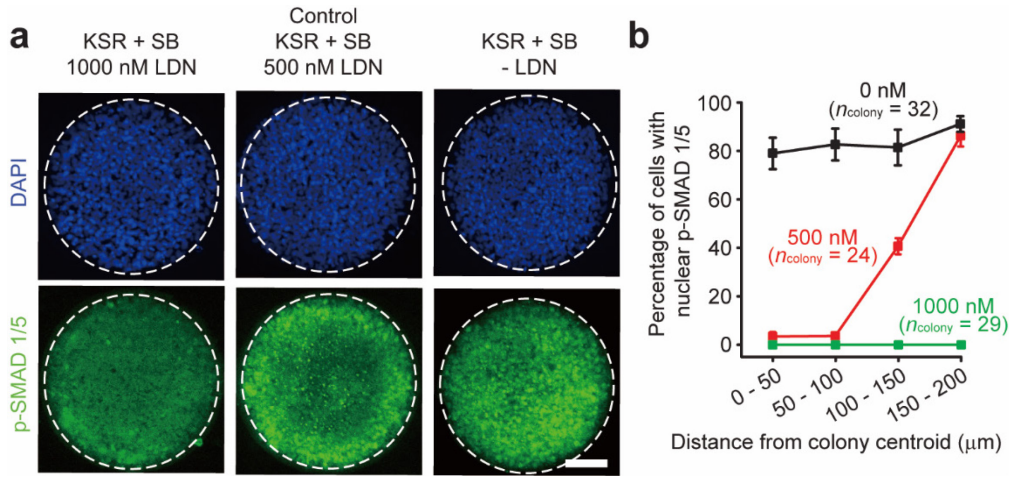

Figure 3-7 Effect of LDN dosage on graded SMAD activation in micropatterned hPS cell colonies. (**a**) Representative immunofluorescence images showing micropatterned hPS cell colonies at day 4 stained for phosphorylated SMAD 1/5 (p-SMAD 1/5). DAPI counterstained nuclei. hPS cells were plated on day 0 at 20,000 cells cm^{-2} onto circular adhesive islands with a diameter of 400 μm. Cells were cultured in neural induction medium with different LDN concentrations as indicated. Scale bar, 100 μm. (**b**) Percentage of cells with nuclear p-SMAD 1/5 as a function of distance from colony centroid under different LDN concentrations as indicated. Based on distance of nuclei from colony centroid, cells were grouped into 4 concentric zones with equal widths as indicated. Number of colonies analyzed were pooled from $n = 2$ independent experiments. Data were plotted as the mean ± s.e.m.

Similarly, replacing LDN with BMP4 (25 ng mL^{-1}) in neural induction medium, a condition that promotes BMP signaling, induced prominent nuclear accumulation of p-SMAD 1/5 across entire colonies (**Figure 3-8 a&b**). Consequently, by day 9 at colony center, NE differentiation was completely inhibited, whereas NPB differentiation was drastically promoted (**Figure 3-8 c**). In distinct contrast, replacing KSR serum in the default neural induction condition with chemically defined Essential 6^{TM} medium, a condition that does not promote BMP signaling[136], inhibited nuclear localization of p-SMAD 1/5 at day 4 and promoted NE differentiation at day 9 across entire colonies (**Figure 3-8 a&b**). Consistently, NPB differentiation across entire colonies by day 9 was completely suppressed (**Figure 3-8 c**).

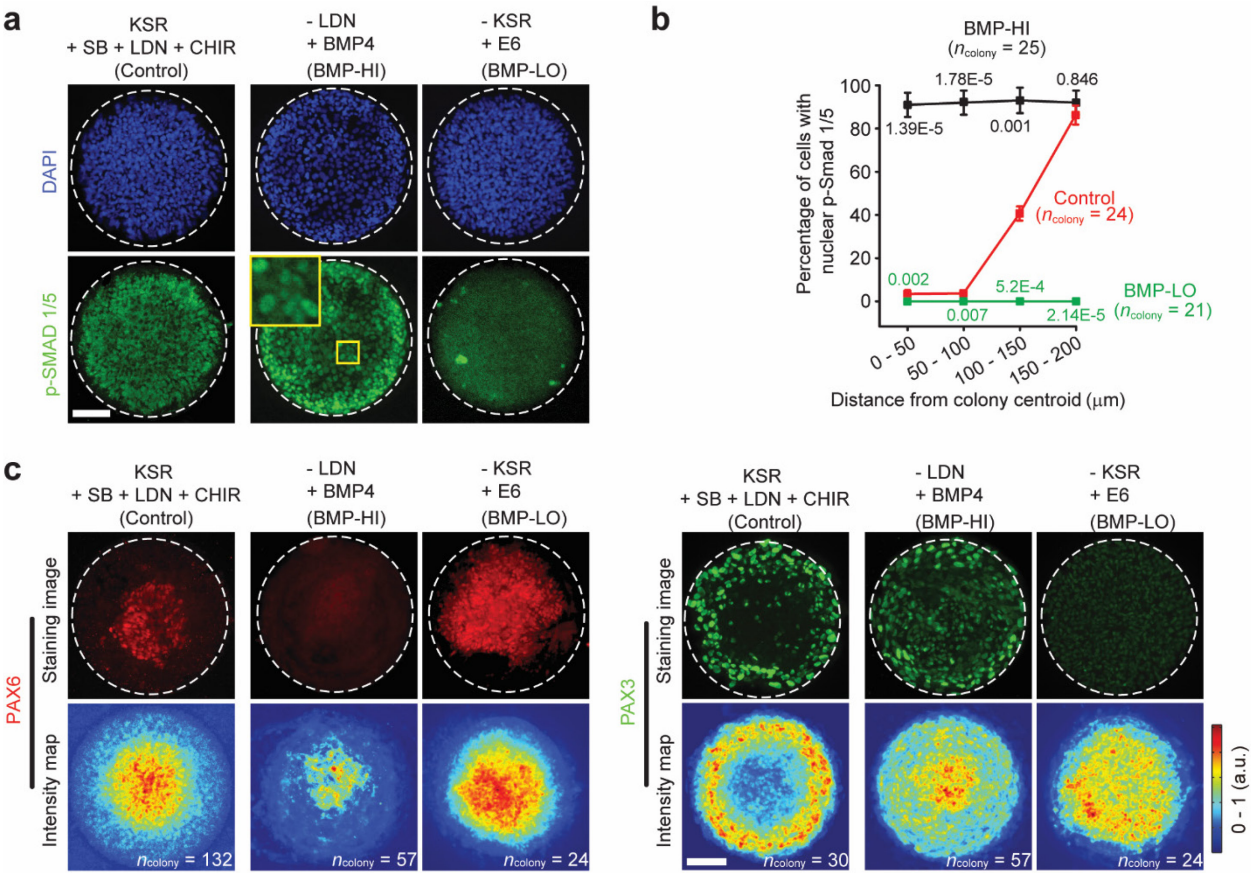

Figure 3-8 BMP-SMAD signaling is required for mechanically guided neuroectoderm patterning. (**a**) Representative immunofluorescence images showing colonies at day 4 stained for

phosphorylated SMAD 1/5 (p-SMAD 1/5). The default neural induction condition (control) was modified as following: - LDN / + BMP4, LDN was replaced with BMP4 (BMP-HI); - KSR / + E6: KSR was replaced with E6 (BMP-LO). CHIR was kept in culture protocols for both BMP-HI and BMP-LO conditions. Zoomed-in image shows a magnified view of colony central area. Scale bar, 100 μm. Experiments were repeated three times with similar results. (**b**) Percentage of cells with nuclear p-SMAD 1/5 as a function of distance from colony centroid. Number of colonies analyzed were pooled from $n = 3$ independent experiments. Data represent the mean ± s.e.m. *P* values were calculated between BMP-HI *vs.* control and BMP-LO *vs.* control using unpaired, two-sided Student's *t*-tests. (**c**) Representative fluorescence micrographs and average intensity maps showing colonies at day 9 stained for PAX6 and PAX3. Scale bar, 100 μm. Experiments were repeated three times with similar results. Number of colonies analyzed were pooled from $n = 3$ independent experiments. Data in intensity maps represent the mean.

We further seeded hES cells on flat PDMS surfaces uniformly coated with vitronectin at a low (5,000 cell cm^{-2}) or high (50,000 cell cm^{-2}) density conditions. Consistent with our previous data, the high density condition significantly down-regulated expression of NPB markers *PAX3* and *SOX9* compared with the low density condition (**Figure 3-9**). However, exogenously activating BMP by supplementing BMP4 (25 ng mL^{-1}) effectively rescued both *PAX3* and *SOX9* expression (**Figure 3-9**). Altogether, our data suggest that morphogenetic cues during emergent neuroectoderm patterning may function upstream of BMP-SMAD signaling to regulate its transcriptional activation (**Figure 3-10**). Geometrical confinement leads to self-organization of morphogenetic factors including cell shape and contractility. Increased cell shape and contractile force at colony periphery result in nuclear accumulation and transcriptional activation of p-SMAD 1/5, which in turn up-regulates NPB specifier genes including *PAX3*, *SOX9* and *SOX10*. Confined cell shape with limited contractile force at colony center leads to nuclear exclusion of p-SMAD 1/5 and NE differentiation. Modulating cell shape by mechanical stretching or geometrical confinement can thus mediate BMP signaling to regulate neuroectoderm patterning. Exogenous BMP activation can rescue inhibitory effects of confined cell shape (or small cell spreading area) and impaired cytoskeletal contractile force on BMP signaling.

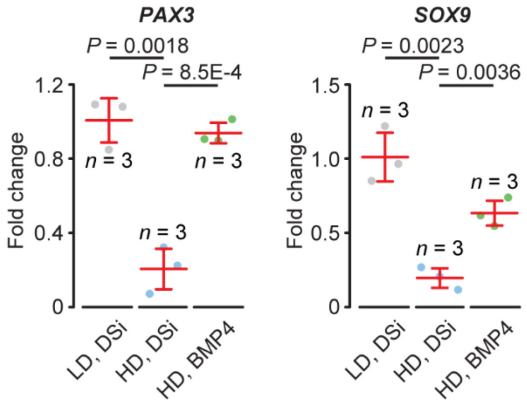

Figure 3-9 Dot plots showing qRT-PCR analysis of neural plate border (NPB) markers *PAX3* and *SOX9*. Human TBP primers were used as an endogenous control for relative quantifications. hPS cells were plated on coverslips uniformly coated with vitronectin at either 10,000 cell cm^{-2} (low density, or LD) or 50,000 cell cm^{-2} (high density, or HD), and RNAs were collected at day 9. Default neural induction protocol was modified as following: for DSi, CHIR was not added to the medium; for BMP4, LDN was replaced with BMP4 (25 ng mL^{-1}) and CHIR was not added to medium. $n = 3$ independent experiments. Error bars, the mean ± s.e.m. *P* values were calculated using unpaired, two-sided Student's *t*-tests.

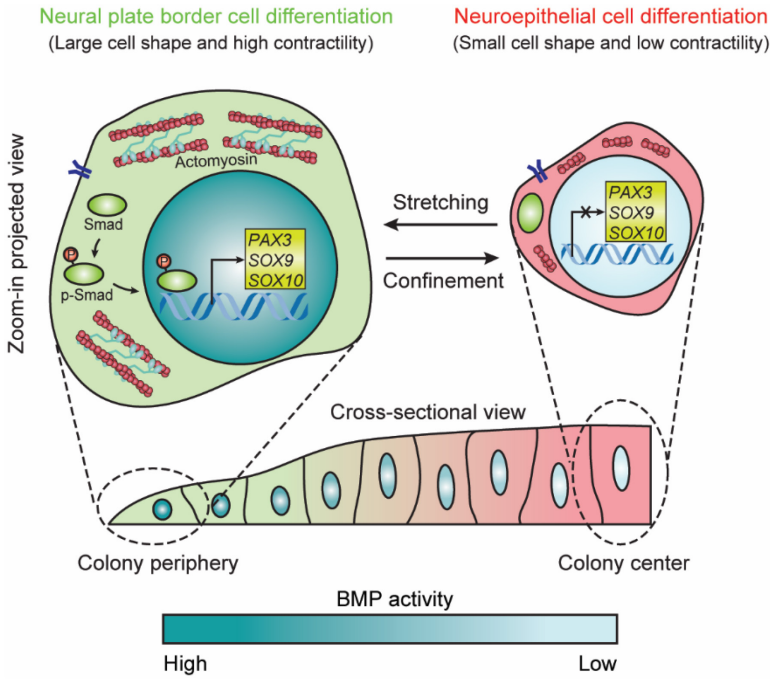

Figure 3-10 Cell shape and contractility regulates BMP-SMAD signaling and dictates NE and NPB cell fate lineage commitment during neuroectoderm patterning. Geometrical confinement leads to self-organization of morphogenetic factors. Increased cell shape and contractile force at colony periphery result in nuclear accumulation and transcriptional activation of p-SMAD 1/5, which in turn up-regulates NPB specifier genes including *PAX3*, *SOX9* and *SOX10*. Confined cell shape with limited contractile force at colony center leads to nuclear exclusion of p-SMAD 1/5 and NE

differentiation. Modulating cell shape by mechanical stretching or geometrical confinement can thus mediate BMP signaling to regulate neuroectoderm patterning.

Our data, together with others[81, 113, 137-139], highlight the dependence of emergent fate patterning of hPS cell colonies on both colony geometry and cell density. Etoc *et al.* have recently reported a cell density-dependent mechanism for graded BMP signaling involving subcellular lateralization of BMP receptors and diffusion of endogenous NOGGIN[138]. To explore whether subcellular lateralization of BMP receptors was involved in our neuroectoderm developmental model, tight-junction integrity was disrupted during neural induction by a brief calcium depletion followed by incubation with Y-27632 (20 μM), a ROCK (Rho-associated protein kinase) inhibitor, a condition known to prevent tight junction formation[138, 140] (**Figure 3-11).** Such treatment has been shown to allow intercellular diffusion of apically delivered TGF-β ligands to bind basolateral receptors and thus restore downstream SMAD activity in high-density epithelial monolayers[138, 140]. However, under conditions that disrupted cell-cell contacts, proper neuroectoderm patterning was still achieved at day 9 in micropatterned colonies (**Figure 3-11**), supporting the hypothesis that subcellular lateralization of BMP receptors was unlikely to be responsible for establishing graded BMP signaling in our neuroectoderm model.

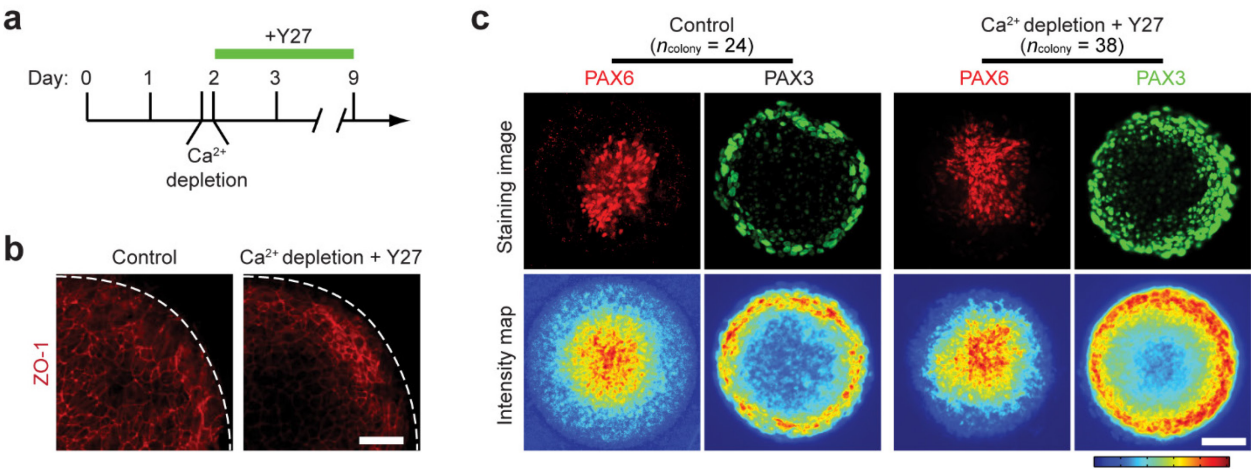

Figure 3-11 Tight-junction integrity is not required for neuroectoderm patterning in micropatterned hPS cell colonies. (**a**) Tight-junction disruption protocol. Tight junction integrity was disrupted during neural induction by 20 min calcium depletion followed by incubation with ROCK inhibitor Y-27632 (Y27; 20 μM). Specifically, calcium depletion was conducted by treating cells with 2 mM EGTA in Hank's balanced salt solution without calcium or magnesium ($HBSS^-$) for 20 min. (**b**) Representative confocal images showing ZO-1 staining at apical surfaces of micropatterned colonies at day 4. It is notable that ZO-1 staining became diminished at the colony central region under the tight-junction disruption condition. Experiments were repeated twice with similar results. Scale bar, 50 μm. (**c**) Representative immunofluorescence images and average intensity maps showing colonies at day 9 stained for PAX6 and PAX3 under control and tight-junction disruption conditions as indicated. Scale bar, 100 μm. Experiments were repeated twice with similar results. Number of colonies analyzed were pooled from $n = 2$ independent experiments. Data in intensity maps were plotted as the mean.

In this work, we demonstrate that autonomous patterning of neuroectoderm tissue with proper NP and NPB regionalization emerges *de novo* as the tissue physically takes shape and self-assembles in pre-patterned geometrical confinements. Self-organization of morphogenetic cues, including cell shape and cytoskeletal contractility, could directly feedback to mediate BMP activity and thus dictate spatial regulations of NE and NPB lineage commitments during neuroectoderm patterning. Colony geometry can directly influence patterning of cell signaling and cell-cell communication through regulatory mechanisms involving dynamic morphogenetic cues and diffusible signals[81, 113, 137-139]. Such signaling crosstalk in confined geometries involving both biophysical and biochemical determinants may play an important role in

controlling patterning networks to ensure the remarkable robustness and precision of tissue self-organization *in vivo*[120-124]. We envision that hPS cell-based developmental models including the one presented in this work can facilitate future efforts in generating theoretical frameworks that integrate knowledge at the mechanical, cellular and gene-regulatory levels[81, 113, 137-139]. Future mechanistic investigations of tissue mechanics-guided neuroectoderm patterning will therefore help advance fundamental understanding of neural development and disease. The hPS cell-based neural induction model could be leveraged for developing high-throughput toxicological studies and drug screening platforms for prevention and treatments of neural tube defects.

Chapter 4

Dorsal-Ventral Patterned Neural Cyst from Human Pluripotent Stem Cells in a Neurogenic Niche

The major content of this chapter is reproduced from my previously published paper: "Dorsal-ventral patterned neural cyst from human pluripotent stem cells in a neurogenic niche" in Science Advances, 2019 [141].‡

4.1 Introduction

After neural induction, the NP folds toward the dorsal side of the embryo and fuses to form the NT. The posterior region of the NT gives rise to the spinal cord, whereas the anterior region becomes the brain, which together comprise the central nervous system (CNS). A very important process during neurulation is the progressive specification of the NT along the dorsal-ventral (DV) axis, DV patterning of the NT [5, 142], which leads to the differentiation of distinct classes of neuronal progenitor cells located at defined positions within the NT. In recent years,

‡ Research presented in this chapter has received assistance from Dr. Yuanyuan Zheng (cell culture, design and perform differentiation assay), Ms. Agnes Resto-Irizarry (imaging processing). I would also like to thank Dr. Yue Shao, Dr. Yi Zheng, and Dr. Zida Li for their comments and Dr. Jianping Fu for his supervision on the research presented in this chapter.

tremendous progress has been achieved in understanding the molecular mechanism(s) of DV patterning of the NT using model organisms. Allocation of neuronal fate in the NT is directed by secreted inductive factors (*i.e.*, morphogens) expressed in local surrounding tissues [5, 142]. Thus, the position of progenitor cells in the NT influences cell fate by defining the identity and concentration of inductive signals to which they are exposed. However, in the ultimate quest to understand the mechanism(s) of human NT development with the goal to prevent and treat developmental defects in the human CNS, studies using model systems remain suboptimal, given significant interspecies divergence [143]. This limitation is further compounded by limited accessibility to the *in utero* post-implantation mammalian embryo for experimental studies.

Human pluripotent stem cells (hPSCs) have been successfully utilized for modelling post-implantation human embryonic development [81, 137, 144]. These stem cell-based human development models provide promising experimental systems to study early neural development in humans, as neural cells derived *in vitro* from hPSCs display molecular and functional properties compatible to those in the developing embryonic brain [145]. Technological advances in three-dimensional (3D) hPSC cultures have further led to the development of self-organized, multicellular neuronal tissues, termed brain organoids, that resemble the cerebral cortex, midbrain, and many other brain regions [146]. Importantly, a 3D, DV patterned NT model has recently been reported in a pioneering work with mouse ESCs [147, 148]. However, progress in generating a stem cell-based, DV patterned human NT model has been limited. A recent work shows 3D induction of dorsal, intermediate and ventral spinal cord-like tissues from hPSCs in a free-floating cell aggregate culture system [149]. However, this work falls short in demonstrating fully organized patterning of spinal cord-like tissues along the DV axis. The apical surface of spinal cord-like tissues derived in this work faces outside external environments [149], distinctly

different from the NT *in vivo*. Together, it remains elusive whether hPSCs can be utilized to generate a human NT development model with full DV patterning. Together, it remains unknown whether hPSCs can be utilized to generate a human NT development model with full DV patterning.

In this chapter, I report a biomimetic 3D culture system mimicking the *in vivo* neurogenic niche for the development of a hPSC-based, DV patterned human NT development model. The biomimetic 3D culture incorporates some key *in vivo* neurogenic niche elements [150], including a 3D basal lamina extracellular matrix (ECM) to provide a permissive extracellular environment and a soft tissue bed to reconstruct the mechanical environment provided by the ventricular surface and ECM for the neuroepithelium during neurulation. This 3D biomimetic culture system allows for convenient manipulations of dynamic interplays between chemical and biophysical signals that are critical for the cellular morphogenetic events and progressive neuronal fate specification during DV patterning of NT-like tissues derived from hPSCs. Development of the biomimetic 3D culture system, together with extrinsic exogenous biochemical signals delivered at precise timing and concentration, allows us to employ hPSCs to achieve the development of a human NT development model with DV patterning. Our hPSC-based *in vitro* NT development model provides a valuable experimental tool for the analysis of human NT development and will contribute to researches on NT-related diseases and potentially to drug discovery and regenerative medicine.

4.2 Materials and methods

4.2.1 Cell culture.

hESC line H9 (WA09, WiCell; NIH registration number: 0062), H1 (WA01, WiCell; NIH registration number: 0043) and 1196a hiPSC line (from the University of Michigan Pluripotent Stem Cell Core33) were cultured under a standard feeder-free condition in mTeSR1 medium (STEMCELL Technologies) with daily medium exchange. Cells were passaged every 5 d using dispase (STEMCELL Technologies) and the STEMPRO EZPassage Disposable Stem Cell Passaging Tool (Invitrogen). Cell pellets re-suspended in mTeSR1 were transferred onto a 6-well tissue culture plate (BD Biosciences) pre-coated with 1% lactate dehydrogenase-elevating virus (LDEV)-free hESC-qualified reduced growth factor basement membrane matrix Geltrex™ (Thermo Fisher Scientific). All the cell lines used in this study had a passage number < P70, and it was authenticated as karyotypically normal by Cell Line Genetics. H9 hESC line was tested negative for mycoplasma contamination (LookOut Mycoplasma PCR Detection Kit, Sigma-Aldrich).

4.2.2 Fabrication of gel beds.

Geltrex™ gel bed was generated based on a "sandwich" scheme developed recently for inducing amniogenesis from hPSCs [81]. In brief, two 12-mm diameter round glass coverslips were treated with air plasma (Harrick Plasma) for 2 min. One of the coverslips, which was to be coated with the gel bed, was soaked in 0.1 mg mL-1 poly-(L-lysine) (PLL) solution (Sigma-Aldrich) for 30 min and then in 1% glutaraldehyde solution (Electron Microscopy Sciences) for another 30 min. The other coverslip was coated with 0.1 mg mL-1 poly-(L-lysine)-graft-poly-(ethylene glycol) (PLL-g-PEG; SuSoS) solution for 1 h. To obtain gel beds with nominal thickness of 20, 60, and 100 μm, undiluted Geltrex (10, 30 and 50 μL, respectively) was then sandwiched between the two coverslips on ice before being incubated at 37 °C for 30 min. The glass coverslip coated with the Geltrex gel bed was then gently separated from the PLL-g-PEG

coated coverslip, before being submerged in DMEM/F12 medium (Thermo Fisher Scientific) and incubated at 37 °C overnight before plating cells at the following day.

4.2.3 Neural induction.

hESC colonies were first treated with Accutase (Sigma-Aldrich) for 10 min at 37 °C. Cells were rinsed briefly with PBS before being collected, centrifuged and re-suspended in mTeSR1 containing the ROCK inhibitor Y27632 (10 μM, Tocris). Singly dissociated hESCs were plated onto coverslips at an initial cell seeding density of 50×10^3 cells cm^{-2} and cultured overnight. For Gel-2D and Gel-3D cultures, the coverslip was pre-coated with the Geltrex™ gel bed, whereas for Glass-2D and Glass-3D conditions, glass coverslips were pre-coated with 1% Geltrex solution for 1 h at room temperature. On the following day (day 1), culture medium was switched to fresh N2B27-based neural induction medium (see below). For Gel-3D and Glass-3D conditions, this neural induction medium contained 2% (*v* / *v*) Geltrex. Thereafter, fresh neural induction medium with or without 2% (*v* / *v*) Geltrex supplement was exchanged daily.

N2B27-based neural induction medium comprised Advance DMEM/F12 (Gibco) : Neurobasal medium (1 : 1; Gibco), 0.5× N2 (GIBCO), 0.5× B27 (GIBCO), 1× nonessential amino acids (GIBCO), 2 mM L-glutamine (GIBCO) and 0.1 mM b-mercaptoethanol (Sigma). N2B27-based neural induction medium further contained TGF-β pathway inhibitor SB431542 (SB, 10 μM; STEMCELL Technologies) and BMP inhibitor LDN193189 (LDN, 0.1 μM; STEMCELL Technologies).

To induce DV patterning of NE cysts, all-trans retinoic acid (RA, 1 μM; TEMCELL Technologies), recombinant human Sonic Hedgehog (SHH, 10 nM; PeproTech), were supplemented into neural induction medium from day 4. For motor neuron induction, the

following chemicals were added to neural induction medium day 12: 10 ng mL^{-1} brain-derived neurotrophic factor (BDNF; R&D systems), 10 ng mL^{-1} glial-derived neurotrophic factor (GDNF; PeproTech), 10 ng mL-1 ciliary neurotrophic factor (CNTF; PeproTech) 10 ng mL^{-1} insulin-like growth factor-1 (IGF-1; PeproTech), 1 μM cyclic adenosine monophosphate (cAMP; Sigma), and 0.2 μg mL^{-1} ascorbic acid (Sigma).

4.2.4 Immunocytochemistry.

Cystic tissues were fixed in 4% paraformaldehyde (PFA, Electron Microscopy Sciences) at room temperature for 1 h before being permeabilized with 0.1% sodium dodecyl sulfate (SDS, dissolved in PBS) solution at room temperature for 3 h. Cysts were then blocked in 10% goat serum solution (Thermo Fisher Scientific) or 4% donkey serum solution (Sigma) at 4 °C overnight. Immunostaining was performed in primary antibody solutions prepared in blocking buffer for 24 h at 4 °C. Cysts were then washed with PBS and incubated with goat or donkey-raised secondary antibodies at 4 °C for another 24 h. DAPI (Invitrogen) was used for counterstaining cell nuclei. All primary antibodies, their sources and dilutions are listed in **Appendix A**.

4.2.5 Confocal microscopy and image analysis.

Images were recorded using an Olympus 1×81 fluorescence microscope with a CSU-X1 spinning-disc unit (Yokogawa). 3D reconstructed cyst images were obtained using ImageJ (NIH).

4.2.6 Statistical analysis.

All data are shown as the mean ± s.e.m. Statistical analysis on the qRT-PCR data was performed using two-side unpaired student *t*-tests in Excel (Microsoft). $P < 0.05$ was considered statistically significant

4.3 Results

4.3.1 3D biomimetic culture for neuroepithelial cyst development

In the 3D biomimetic culture system, H9 hESCs were plated as single cells at 50×10^3 cells cm^{-2} onto a thick, soft gel bed of Geltrex (with thickness ≥ 100 μm, bulk Young's modulus ~ 900 Pa, coated on a glass coverslip), in mTeSR1 medium supplemented with the ROCK inhibitor Y27632 (**Figure 4-1 A**). At 24 h (day 1), a neurogenic environment was established by replacing mTeSR1 with a fresh neural induction medium comprising N2B27 supplemented with SB431542 (SB, TGF-β inhibitor) and LDN 193189 (LDN, BMP4 inhibitor) [151, 152] (**Figure 4-1 A**). To establish a 3D neural induction environment, 2% (*v* / *v*) Geltrex was further supplemented into the neural induction medium (hereinafter referred to as 'Gel-3D'; **Figure 4-1 A**). In Gel-3D condition, while undergoing neural conversion with PAX6 expression, hESCs self-assembled to form pseudostratified, multicellular cystic tissues enclosing a central lumen with the ZO-1 apical surface facing inward (**Figure 4-1 B**). We investigated the development of NE cysts in Gel-3D with different gel bed thicknesses (**Figure 4-1 A**). When the gel bed thickness decreased from 100 μm to 60 μm or 20 μm, which increased the effective substrate rigidity [128], although PAX6 expression was evident in all cysts, these cysts showed a flattened morphology with a jagged basal surface (**Figure 4-1 A**). In contrast, regular, spherical cystic tissues containing multilayered NE cells with smooth outside surfaces were evident in thick gel bed (100 μm). Altogether, our data suggest that matrix rigidity might be an important factor mediating the formation of spherical NE cystic tissues.

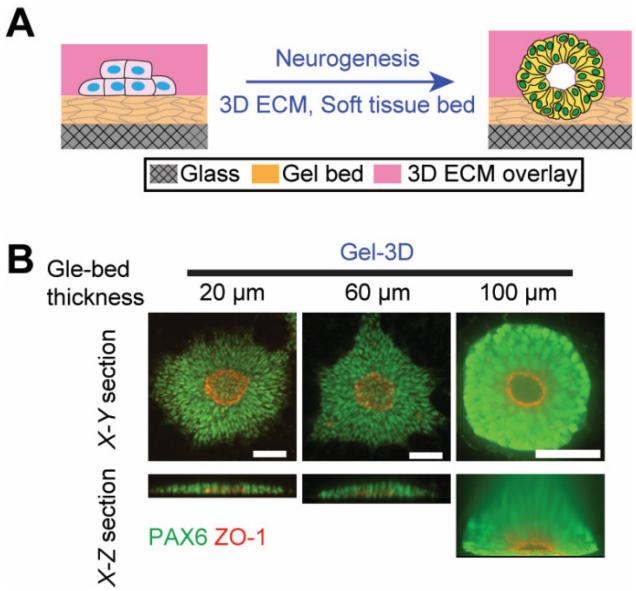

Figure 4-1 hESCs form neuroepithelial (NE) cysts in an engineered 3D neurogenic niche. (**A**) Schematic of neural induction in a 3D *in vitro* culture system comprising a gel bed and an ECM overlay (Gel-3D). (**B**) Confocal micrographs showing *X*-*Y* and *X*-*Z* sections of multicellular structures cultured in Gel-3D with varying gel bed thicknesses stained for PAX6 and ZO-1. DAPI counterstained nuclei. Scale bars, 50 μm.

Additional molecular characterizations were conducted for lumenal NE cysts derived from H9 hESCs in Gel-3D. In addition to PAX6, NE cysts showed strong expression of SOX2 and NESTIN, another two neuroectodermal markers, at day 8. Neither SOX17, a definitive endoderm marker, nor BRACHYURY, CDX2 or EOMES, which are primitive streak and mesodermal markers, was detectable at day 8 (**Figure 4-2**), excluding mesoderm or endoderm lineages in Gel-3D.

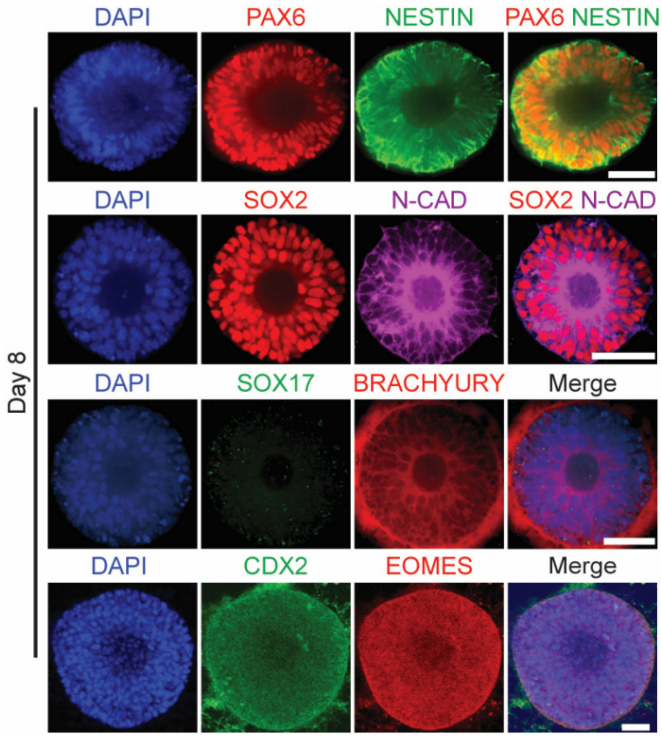

Figure 4-2 Molecular characterizations for neuroepithelial cysts. Representative cystic tissues in Gel-3D at day 8 stained for PAX6, NESTIN, SOX2, N-CAD, SOX17, BRACHYURY, CDX2 and EOMES as indicated. DAPI counterstained nuclei. Scale bars, 50 μm.

4.3.2 Dorsal-ventral patterning of neuroepithelial cysts

To determine whether Gel-3D could support DV patterning of NE cysts, we culture hESCs in neural induction condition for 18 days, with RA (1 μM) and SHH (10 nM) supplemented into neural induction medium from day 4 to day 9 (**Figure 4-3 A**). Indeed, with RA and SAG, a small portion of NE cysts (22 ± 3.06%) displayed the key architectural feature of DV patterning at day 18, with ventral progenitor domains aligned adjacent to an induced floor plate (FP) region (**Figure 4-3 B&C**). Specifically, in these patterned NE cysts, a single FOXA2+ FP domain emerged asymmetrically at one pole of the cyst (**Figure 4-3 B**). Adjacent to the FP, two NKX2.2+ p3 progenitor domains emerged in a symmetrical fashion (**Figure 4-3 B**). Two OLIG2+ pMN domains also simultaneously emerged dorsal to the two NKX2.2+ p3 domains, respectively (**Figure 4-3 B**). Importantly, by day 18, PAX3+ dorsal NE cells became detectable

and were restricted to the opposite pole of the OLIG2+ pMN domain (**Figure 4-3 B**), suggesting successful DV patterning of NE cysts under RA and SAG stimulation.

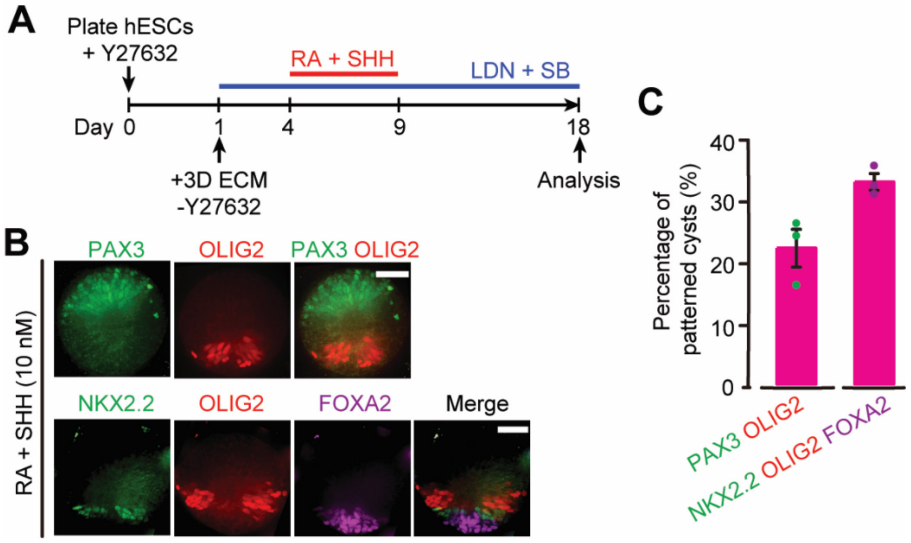

Figure 4-3 Self-organized, emergent dorsal-ventral patterning of neuroepithelial cysts in Gel-3D. (**A**) Schematic of patterning of NE cysts with RA and SHH from day 4 to day 9. (**B&C**) Representative confocal micrographs showing RA/SHH-treated NE cysts at day 18 stained for dorsal and ventral markers as indicated (B). C plots percentages of different patterned cysts. Data in C&F represent the mean ± s.e.m. A total of 150 cysts was pooled from $n = 3$ independent experiments under RA/SHH conditions. Scale bars, 50 μm.

We confirmed that spherical PAX6+ NE cysts containing single central lumens could be derived from H1 hESC line and a hiPSC line (1196a) in Gel-3D under neural induction condition by day 8 (**Figure 4-4**). With RA and 10 nM SHH treatment from day 4 to day 9, proper DV patterned NE cysts were also achieved using H1 hESC line and 1196a hiPSC line in Gel-3D at day 18 (**Figure 4-4**).

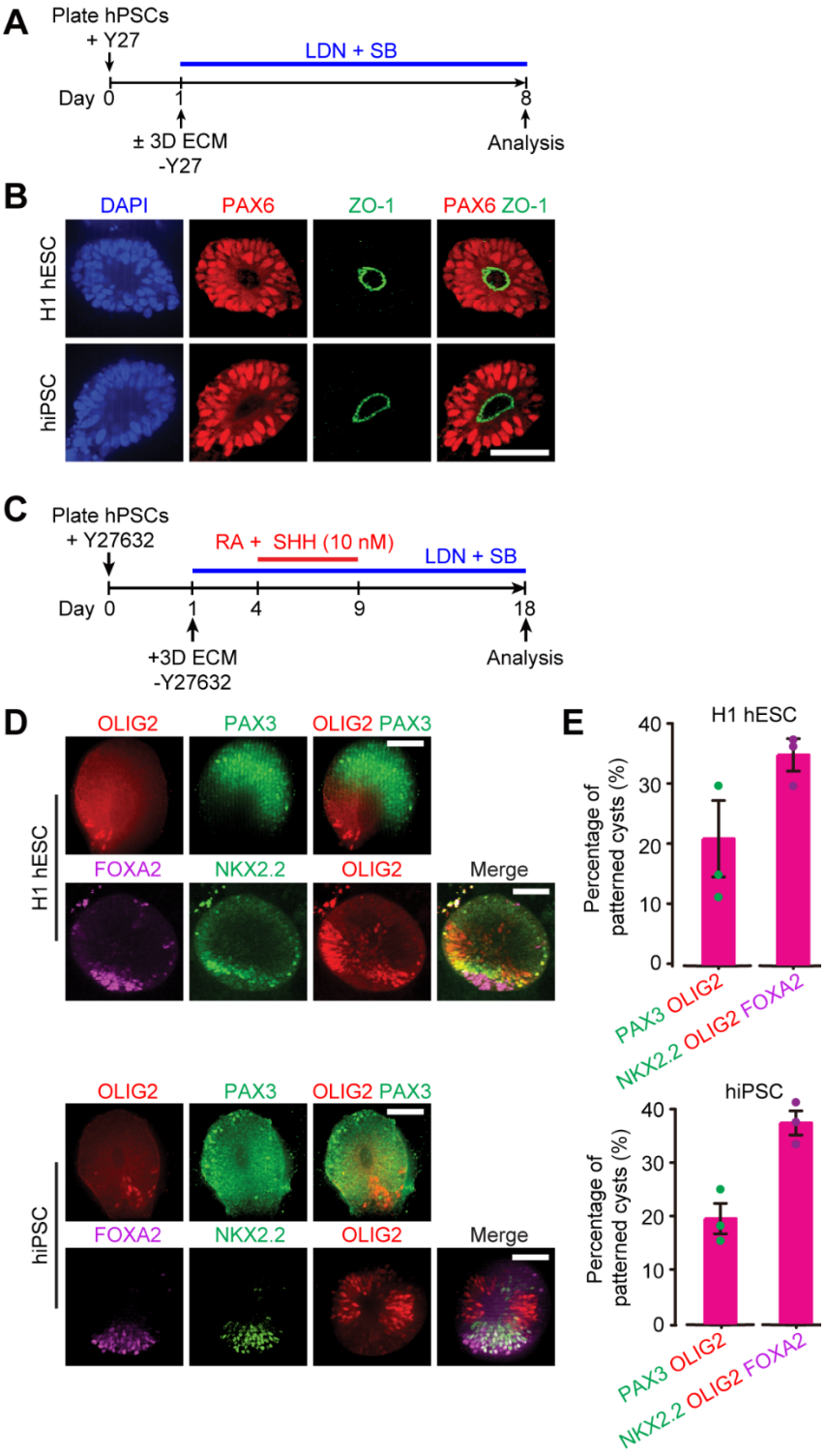

Figure 4-4 Dorsal-ventral patterning of neuroepithelial cysts from multiple hPSC lines in Gel-3D. (**A**) Schematic of neural induction protocol in Gel-3D. (**B**) Representative confocal micrographs showing NE cysts generated from H1 hESC line and 1196a hiPSC line at day 8 stained for PAX6 and ZO-1. DAPI counterstained nuclei. (**C**) Schematic of patterning of NE cysts with RA and SHH from day 4 to day 9. (**D**) Representative confocal micrographs showing RA/SHH-treated NE cysts

from H1 hESC line and 1196a hiPSC line at day 18 stained for dorsal and ventral markers as indicated. (**E**) Percentages of different patterned cysts derived from H1 hESC line and 1196a hiPSC line. Data represent the mean ± s.e.m. For H1 hESC line, n_{cyst} = 118 and 124 for PAX3/OLIG2 staining and NKX2.2/OLIG2/FOXA2 staining, respectively. For 1196a hiPSC line, n_{cyst} = 142 and 134 for PAX3/OLIG2 staining and NKX2.2/OLIG2/FOXA2 staining, respectively. n = 3 independent experiments. Scale bars in B and D, 50 μm.

We next examined expression of other lineage markers associated with different ventral NT domains in NE cysts obtained under treatment with RA and 10 nM SHH (**Figure 4-5**). DBX1 (marker for p0 domain), DBX2 (marker for p0 and p1 domains), or NKX6.2 (marker for p1 domain) was not detectable at day 18 (data not shown). It is likely that induction of these more dorsally localized domains might require other morphogen signals such as BMP or WNT, which are secreted by tissues adjacent to the NT *in vivo*. Interestingly, around 20% of NE cysts showed localized expression of NKX6.1 (**Figure 4-5**), a marker for the p3, pMN and p2 domains [67, 153]. The OLIG2+ pMN domain enclosed in the NKX6.1+ domain was observed in 22.27% ± 4.24% of NE cysts (**Figure 4-5**). We further observed mutually exclusive expression of NKX6.1 domain and FOXA2 domain in 13.6% ± 2.86% of NE cysts (**Figure 4-5**).

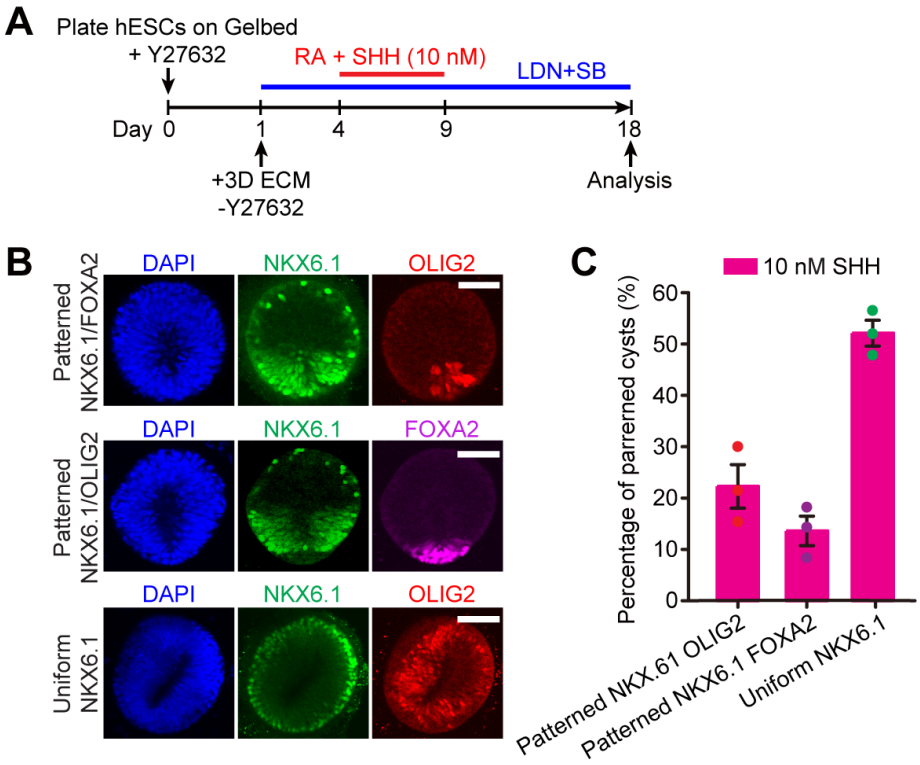

Figure 4-5 NKX6.1 expression in ventral patterned neuroepithelial cysts in Gel-3D. (**A**) Schematic of patterning of neuroepithelial (NE) cysts with RA and SHH from day 4 to day 9. (**B**) Representative confocal micrographs showing RA/SHH-treated NE cysts at day 18 stained for NKX6.1, OLIG2 and FOXA2. Scale bars, 50 μm. (**C**) Percentages of different patterned cysts. Data represent the mean ± s.e.m. n_{cyst} = 153 from n = 3 independent experiments.

4.3.3 Progressive dorsal-ventral patterning of neuroepithelial cysts

We next studied dynamic, progressive DV patterning of NE cysts by tracking spatiotemporal expression of dorsal and ventral markers, with NE cysts stimulated with RA (1 μM) and SHH (10 nM) from day 4 to day 9 (**Figure 4-6**). At day 9, all NE cysts contained PAX3+ dorsal cells but without any OLIG2+ pMN progenitor cells detectable (**Figure 4-6 A&B**). OLIG2+ cells started to emerge at day 12 in cyst regions where PAX3 expression was absent (**Figure 4-6 A**). From day 14 to day 18, the percentage of NE cysts containing OLIG2+ cells continued to increase, whereas the PAX3 domain continuously became more restricted

(**Figure 4-6 A**). In a subset of NE cysts where OLIG2+ cells emerged as a cluster (the putative pMN domain) towards the prospective ventral pole of the cyst, concurrent, progressive restriction of the PAX3+ domain towards the opposite dorsal pole was evident (**Figure 4-6 A**), suggesting dynamic progression of DV patterning regulated by RA and SHH through dual effects on ventralization and antagonizing dorsalization [6]. PAX3-OLIG2 DV polarity was established in 3.33% ± 1.33% of cysts at day 12, and this value increased at day 14 and day 16 and reached 26.52 ± 5.34% at day 18 (**Figure 4-6 A&B**).

We next tracked NKX2.2 and FOXA2 expression. At day 9, NKX2.2 was not detectable; but 65.35 % ± 2.79% NE cysts contained sparsely distributed FOXA2+ FP progenitor cells (**Figure 4-6 C&D**). At day 12, NKX2.2 remained undetectable; however, the percentage of NE cysts containing FOXA2+ cells decreased to 26.67% ± 1.76% (**Figure 4-6 C&D**). Notably, FOXA2+ cells appeared as a cluster (the putative FP domain) at the presumptive ventral pole at day 12 (**Figure 4-6 C&D**). NKX2.2 became detectable from day 14 onwards, and its expression was evident only in cysts containing FOXA2+ cells (there was < 4% cysts containing only NKX2.2+ cells at day 14; **Figure 4-6 C&D**). Importantly, 17.62% ± 2.23% of NE cysts at day 14 displayed localized NKX2.2 domains dorsal to the FOXA2+ FP region (**Figure 4-6 C&D**), suggesting dynamic patterning of ventral domains. The percentage of such ventral patterned NE cysts increased to 46.18% ± 1.95% at day 18 (**Figure 4-6 C&D**).

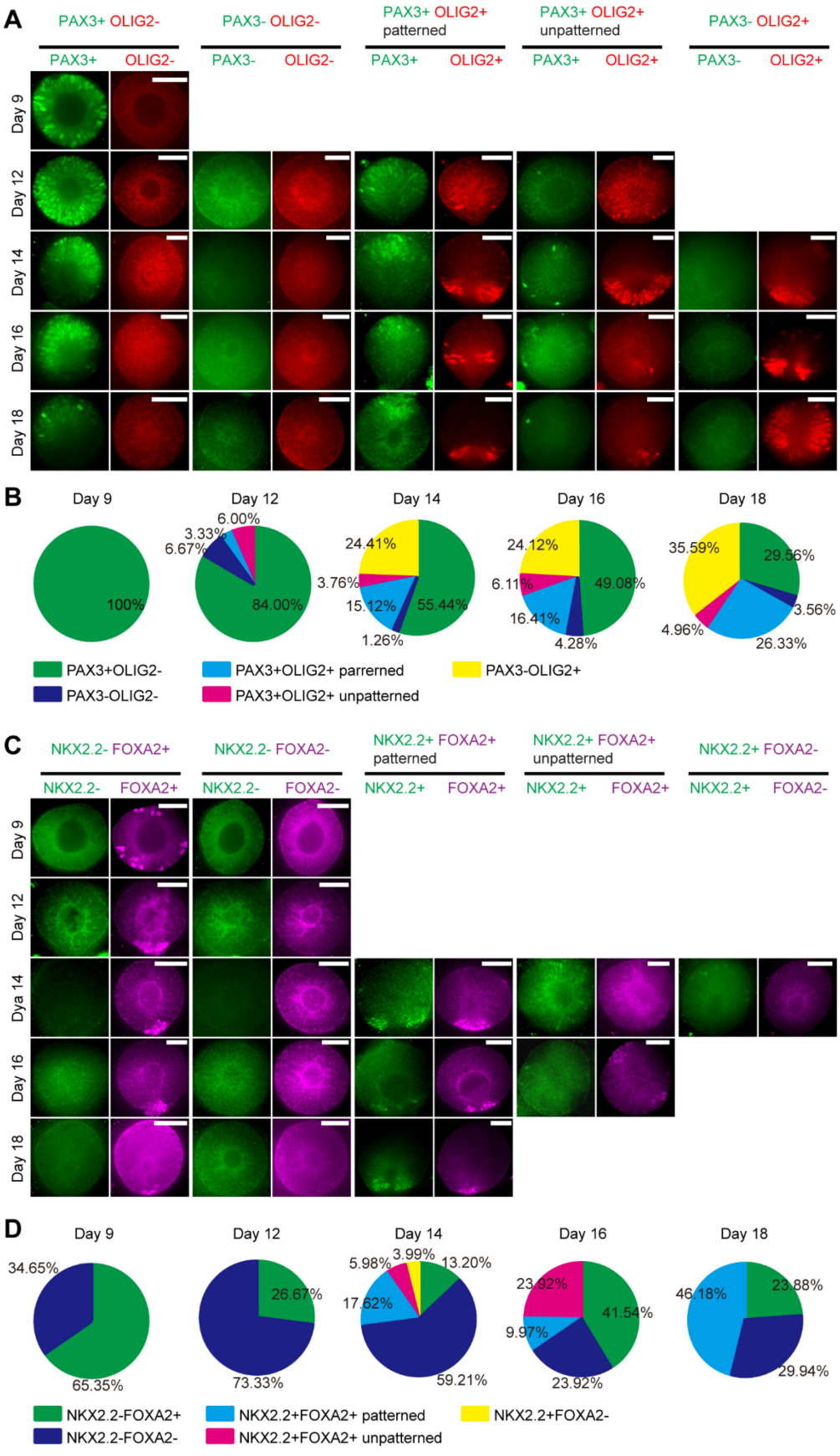
A
PAX3+ OLIG2-
PAX3- OLIG2-
PAX3+ OLIG2+ patterned
PAX3+ OLIG2+ unpatterned
PAX3- OLIG2+
PAX3+
OLIG2-
PAX3-
OLIG2-
PAX3+
OLIG2+
PAX3+
OLIG2+
PAX3-
OLIG2+
Day 9
Day 12
Day 14
Day 16
Day 18
B
Day 9
Day 12
Day 14
Day 16
Day 18
100%
6.00%
3.33%
6.67%
84.00%
24.41%
3.76%
15.12%
55.44%
1.26%
24.12%
6.11%
49.08%
16.41%
4.28%
35.59%
29.56%
3.56%
4.96%
26.33%
PAX3+OLIG2-
PAX3+OLIG2+ parrerned
PAX3-OLIG2+
PAX3-OLIG2-
PAX3+OLIG2+ unpatterned
C
NKX2.2- FOXA2+
NKX2.2- FOXA2-
NKX2.2+ FOXA2+ patterned
NKX2.2+ FOXA2+ unpatterned
NKX2.2+ FOXA2-
NKX2.2-
FOXA2+
NKX2.2-
FOXA2-
NKX2.2+
FOXA2+
NKX2.2+
FOXA2+
NKX2.2+
FOXA2-
Day 9
Day 12
Dya 14
Day 16
Day 18
D
Day 9
Day 12
Day 14
Day 16
Day 18
34.65%
65.35%
26.67%
73.33%
5.98%
3.99%
13.20%
17.62%
59.21%
23.92%
41.54%
9.97%
23.92%
46.18%
23.88%
29.94%
NKX2.2-FOXA2+
NKX2.2+FOXA2+ patterned
NKX2.2+FOXA2-
NKX2.2-FOXA2-
NKX2.2+FOXA2+ unpatterned

Figure 4-6 Dynamics of dorsal-ventral patterning of neuroepithelial cysts in Gel-3D. (**A**) Representative confocal micrographs showing cysts stained for PAX3 and OLIG2 at different days as indicated. (**B**) Pie charts showing percentages of different types of cysts at different days as indicated. Cysts were grouped into 5 categories as indicated (PAX3+OLIG2-, PAX3-OLIG2-, PAX3+OLIG2+ patterned, PAX3+OLIG2+ unpatterned, PAX3-OLIG2+). (**C**) Representative confocal micrographs showing cysts stained for NKX2.2 and FOXA2 at different days as indicated. (**D**) Pie charts showing percentages of different types of cysts at different days as indicated. Cysts were grouped into 5 categories as indicated (NKX2.2-FOXA2+, NKX2.2-FOXA2-, NKX2.2+FOXA2+ patterned, NKX2.2+FOXA2+ unpatterned, NKX2.2+FOXA2-). Data in B & D represent the mean. A total of 150 cysts was counted from $n = 3$ independent experiments at each time point. Scale bars in A & C, 50 μm.

4.3.4 Dorsal-ventral patterning of neuroepithelial cysts is dependent on RA concentration and duration

We next examined the role of RA in the DV patterning of NE cysts. When only 1 μM RA was supplemented in neural induction medium from day 4 to day 9, 28.19% ± 2.31% of NE cysts achieved proper ventral patterning at day 18, with two NKX2.2+ p3 domains positioned dorsal to a single FOXA2+ FP domain (**Figure 4-7 A&B**). However, only 1.95% ± 0.05% of NE cysts showed PAX3-OLIG2 DV polarity, with PAX3+ dorsal cells located at the opposite pole of the OLIG2+ pMN domain (**Figure 4-6 A&B**). When RA concentration was reduced to 0.1 μM, no patterned NE cyst was detectable (**Figure 4-6 A&B**). When stimulation with 1 μM RA was prolonged from day 4 to day 18, no patterned NE cyst was detectable either at day 18 (**Figure 4-6 C**). FOXA2+ FP progenitor cells appeared uniformly at the cyst basal surface (**Figure 4-6 C**). With treated with 0.1 μM RA from Day 4 to day 18, 8.86% ± 1.18% of NE cysts showed PAX3-OLIG2 DV polarity (**Figure 4-6 C&D**). However, ventral patterning of NE cysts was not achieved, as even though OLIG2+ pMN domains adjacent to FOXA2+ FP domain was evident in 27.08% ± 4.45% of NE cysts, the NKX2.2 p3 domain was not detectable in any cyst (**Figure 4-6 C&D**). These results suggest that prolonged global RA stimulation might not be optimal for

DV patterning. Together, these data suggest that optimal DV patterning of NE cysts depends on both RA concentration and the timing and duration of RA stimulation.

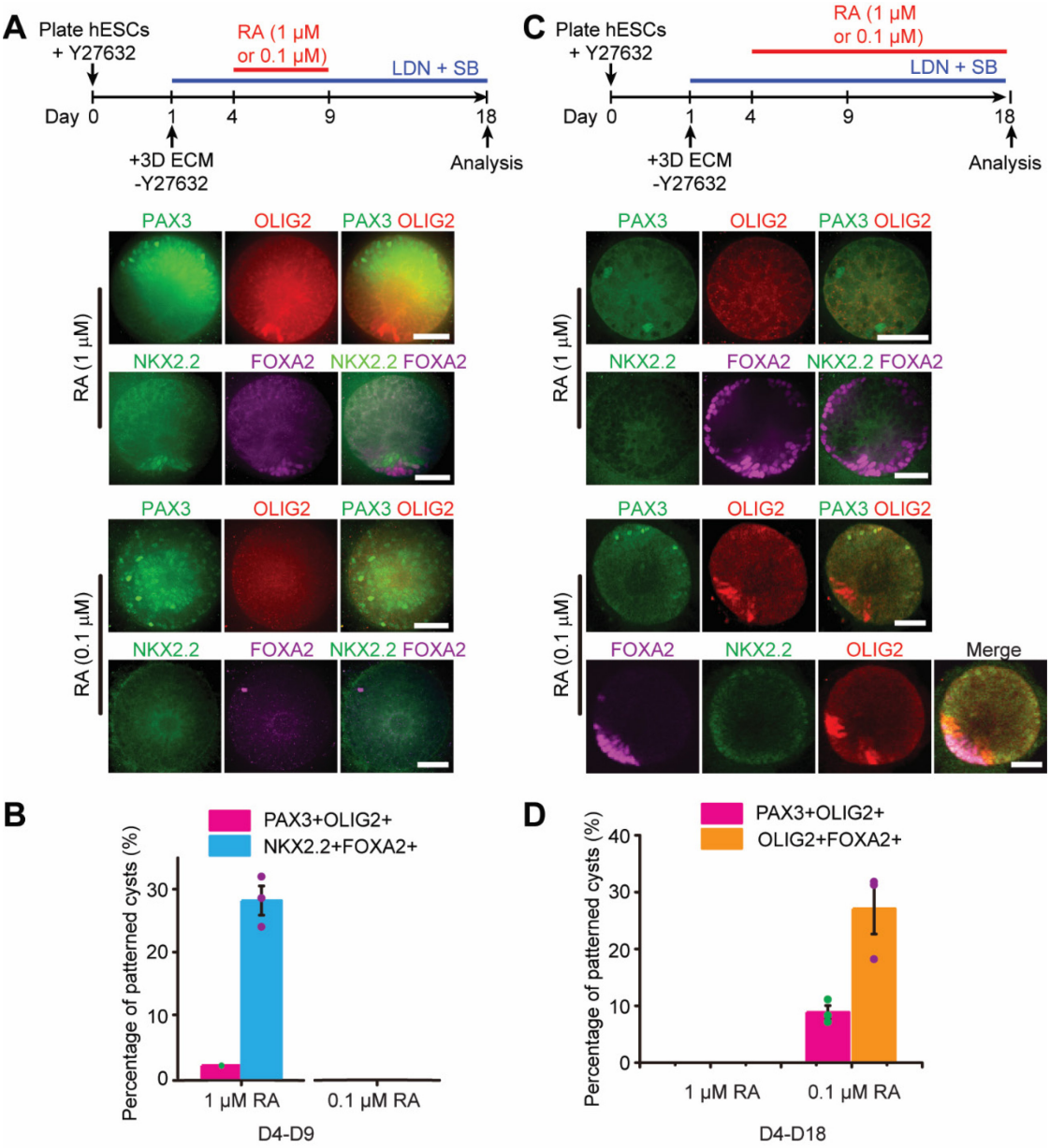

Figure 4-7 Independent effects of RA and SHH on patterning of neuroepithelial (NE) cysts in Gel-3D. (**A**) Effect of RA stimulation (1 μM or 0.1 μM) alone from day 4 to day 9. Representative confocal micrographs show cysts at day 18 stained for dorsal and ventral markers as indicated. (**B**) Percentages of different patterned cysts as a function of RA dose. Data represent the mean ± s.e.m. A total of 150 cysts was counted from $n = 3$ independent experiments at each RA dose. (**C**) Effect of RA stimulation (1 μM or 0.1 μM) alone from day 4 to day 18. Representative confocal micrographs show cysts at day 18 stained for dorsal and ventral markers as indicated. (**D**)

Percentages of different patterned cysts as a function of RA dose. Data represent the mean ± s.e.m. 50 cysts were counted from each independent experiment. $n = 3$ independent experiments at each RA dose. Scale bars in A & C, 50 μm.

4.3.5 Generation of motor neurons from neuroepithelial cysts

After DV patterning of the NT, different progenitor domains of the NT will continue to develop and specify region-specific neuronal subtypes in each domain. The OLIG2+ pMN domain will give rise to MNs, which are localized at the ventral part of NT in vivo. We thus sought to specify OLIG2+ pMN progenitor cells in NE cysts into MNs. To this end, We added neurotrophic factors BDNF (brain-derived neurotrophic factor; 10 ng mL^{-1}), GDNF (glial-derived neurotrophic factor; 10 ng mL^{-1}), CNTF (ciliary neurotrophic factor, 10 ng mL^{-1}), IGF-1 (insulin-like growth factor-1; 10 ng mL^{-1}), cAMP (cyclic adenosine monophosphate; 1 μM) and AA (ascorbic acid; 0.2 μg mL^{-1}) into neural induction medium from day 12 onwards (**Figure 4-8 A**). BDNF is a member of neurotrophin family and is required for the differentiation and survival of specific neuronal subpopulations [154]. GDNF increases proliferation of MN progenitor cells, promotes neuronal differentiation and survival [155]. CNTF is important for the survival of MNs[156]. IGF-1 has been shown to promote differentiation and survival of MNs [157]. When these growth factors are used together *in vitro*, they have been shown to be effective in driving hPSC-derived neural progenitor cells into MNs [158]. Excitingly, at day 25, about 17% of NE cysts contained HB9+ and ISLET1/2+ MNs at the cyst basal region adjacent to the OLIG+ pMN domain (**Figure 4-8 B&C**), suggesting that HB9+ and ISLET1/2+ MNs were developed from the pMN domain in NE cysts.

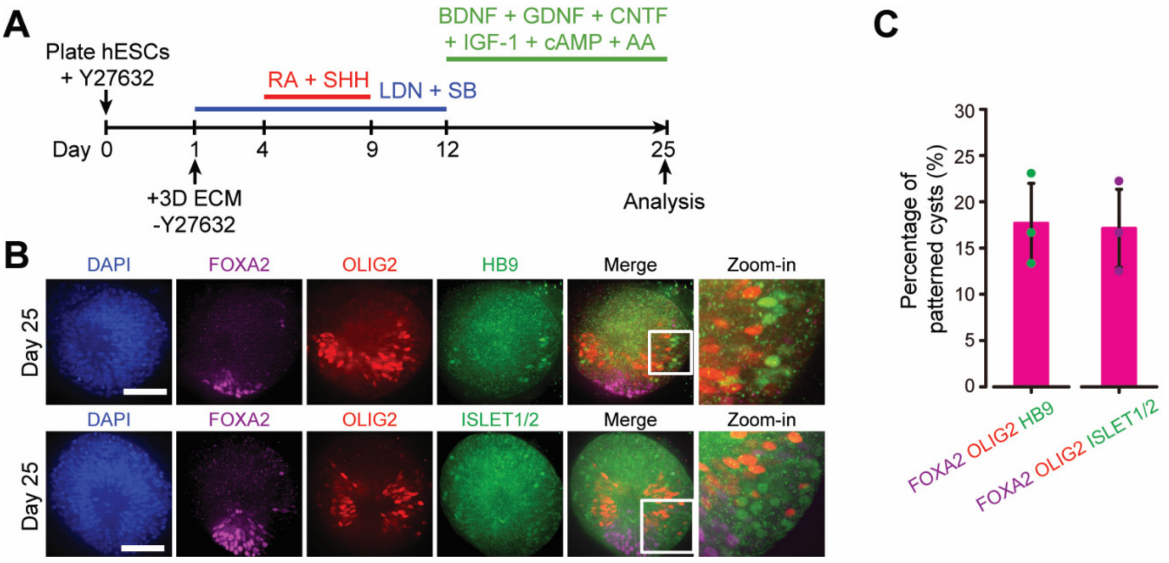

Figure 4-8 Induction of spinal motor neurons (MNs) from neuroepithelial (NE) cysts in Gel-3D. (A&B) Induction of spinal MNs with RA and SHH supplemented from day 4 to day 9 and neurotrophic factors brain-derived neurotrophic factor (BDNF), glial-derived neurotrophic factor (GDNF), ciliary neurotrophic factor (CNTF), insulin-like growth factor-1 (IGF-1), cyclic adenosine monophosphate (cAMP) and ascorbic acid (AA) from day 12 to day 25. Representative confocal micrographs in F show cysts at day 25 stained for FOXA2, OLIG2, HB8 and ISLET1/2. DAPI counterstained nuclei. The zoomed-in image shows a magnified view of the area highlighted by the white square. Scale bars, 50 µm. (C) Percentage of different patterned cysts. Data represent the mean ± s.e.m. ncyst = 126 and 134 for HB9 staining and ISLET1/2 staining, respectively. n = 3 independent experiments.

4.4 Discussion

As the embryonic precursor to the CNS, the NT generates distinct classes of neuronal progenitor cells located at defined positions within the NT through intricate patterning events. Considerable progress has been made in determining the signaling activities and genetic networks that control region-specific neuronal fate patterning in the NT [5, 142, 159]. It is now appreciated that acquisition of a specific neuronal fate depends on the position of precursor NE cells within the NT, which defines their exposure to inductive morphogens that gradually constrain their developmental potential in each local domain. Morphogens instructing DV patterning of the NT include WNTs, BMPs and SHH, with WNT and BMP emanated from the

dorsal ectoderm and roof plate favoring dorsal identities and SHH secreted from the notochord inducing ventral identity [5, 142, 159]. In this work, we have established the neurogenic Gel-3D culture that promotes hPSCs to self-organize into spherical, lumenal NE cysts, mimicking the development of the NT tissue *in vivo*. The intrinsic lumenogenic property of hPSCs prompt the cells to undergo lumenogenesis in Gel-3D to form a central apical lumen [160]. Under the neural induction environment, hPSCs in the lumenal cyst exit pluripotency and progress long the neural lineage while continuing to divide. By day 9, NE cysts emerge in Gel-3D, featuring a single central lumen with correct apicobasal polarity, displaying interkinetic nuclear migration and pseudostratification, and expressing early neuroectodermal markers including PAX6, SOX2, SOX1, NESTIN and N-CAD. NE cysts at day 9 appear to correspond to an early stage of the neural plate formation in the dorsal ectoderm germ layer. Our data show that both ECM dimensionality and matrix rigidity are critical extracellular microenvironmental factors for proper development of NE cysts from hESCs. In particular, a 3D culture environment is required for the development of 3D cystic NE tissues enclosing a central lumen.

Under proper DV patterning conditions, NE cells within lumenal cysts differentiate into region-specific progenitors in discrete local domains and achieve cell fate patterning along the DV axis. Importantly, progressive development of NE cysts features sequential emergence of neural progenitor domains, with the ventral FP, P3 and pMN domains emerging progressively in discrete, non-overlapping regions and the PAX3+ dorsal territory progressively restricted to the opposite, prospective dorsal pole. The OLIG2+ pMN domain in DV patterned NE cysts can be further specified into ISLET1/2+HB9+ MNs.

In the Gel-3D culture, DV patterning of hESC-derived NE cysts appears to initiate after removal of exogenous morphogen signals. This observation may be related to the hysteresis

property of SHH signaling, in which intracellular SHH signaling remains active after withdrawal of exogenous morphogens [161]. Previous studies using mouse NT explants suggest that the transcriptional network for ventral patterning of the NT can produce hysteresis, providing NE cells in the NT with a memory of SHH signaling even when extracellular signaling gradients recede [162]. Our data further suggest a role of intracellular SHH signaling in the ventralizing effect of RA. This observation is consistent with previous studies of the effect of RA on NE tissues derived from mouse ESCs, which have shown induction of SHH by RA administration and consequently expression of ventral NT markers [147]. *In vivo*, both the notochord and FP secrete RA [159], and it has been suspected that RA may act as a permissive signal for SHH-mediated ventral patterning of the NT [147]. Thus, it is likely that supplementation of RA in our system promotes SHH signaling, which in turn induces the specification of FOXA2+ FP progenitor cells.

It remains puzzling how global applications of exogenous morphogens lead to the formation of a local FOXA2+ FP domain. Our temporal immunofluorescence data suggest that at the initial phase of DV patterning, FOXA2+ FP progenitor cells emerge in a scattered fashion at the basal surface of NE cysts. Soon thereafter, FOXA2 expression become restricted to a local, prospective FP region at the putative ventral pole of NE cysts. This observation suggests a likely involvement of a self-enhancing activator/inhibitor signaling system, leading to a single localized FP region formation. This hypothesis remains to be validated in the future.

In this work, we have successfully derived DV patterned NT-like tissues from hPSCs. Nonetheless, it remains a significant challenge (and thus a future goal) to obtain NT-like tissues containing all progenitor domains along the DV axis. *In vivo*, DV patterning of the NT involves multiple morphogen gradients emanated from neighboring signaling centers located at different

anatomical regions. Our current Gel-3D system applies global administrations of exogenous morphogens. It remains a future goal to integrate neural induction of hPSCs with advanced microfluidic systems to introduce well defined, dynamic parallel and antiparallel morphogen gradients to achieve full DV patterning of NT-like tissues. Our DV patterned NT development model offers great opportunities for experimental control of key parameters and quantitative measurements, providing a significantly advantageous experimental platform for advancing our understanding of the emergent self-organizing principles and patterning mechanisms that provide robustness and reliability to NT DV patterning, a long-standing question in biology. Patterned NT-like tissues derived from hPSCs are also useful for the development of stem-cell based regenerative therapies, disease models and screening applications for diagnosis, prevention and treatment of neurological disorders resulted from impairments of the development and growth of the CNS system.

Chapter 5

Conclusion, Perspective, and Future Work

5.1 Summary of thesis

In this dissertation, I leveraged the developmental potential and self-organization property of hPS cells in conjunction with 2D and 3D bioengineering tools to achieve the development of spatially patterned multicellular tissues that mimic certain aspects of human neural induction and DV patterning of the NT.

In chapter 2 and 3, I utilized bioengineering tools such as microcontact printing to establish 2D colonies of hPS cells with defined shapes and sizes. Pre-patterned geometrical confinement induces emergent patterning of hPS cells, mimicking neuroectoderm regionalization during early neurulation. Specifically, hPS cells differentiate and gradually self-organize into a radial symmetrical pattern of NE and NPB cells, with NE cells localized at the colony center and NPB cells accumulating at the colony border. Mechanistic investigations reveal that while hPS cells respond to neural induction signals, they self-organize and display graded mechanical properties, including cell shape and contractile force, along the colony radial axis. Self-organization of cell shape and cytoskeletal contractility feedbacks to regulate graded BMP activity and thus instruct neuroepithelial (NE) / neural plate border (NPB) patterning. This work provides evidence of tissue mechanics-guided neuroectoderm patterning and establishes a

tractable model to study signaling crosstalk involving both biophysical and biochemical determinants in neuroectoderm patterning. The hPS cell-based neural induction model could be leveraged for developing high-throughput toxicological studies and drug screening platforms for prevention and treatments of neural tube defects.

In chapter 4, I established the neurogenic Gel-3D culture that promotes hPSCs to self-organize into spherical, lumenal NE cysts, mimicking the development of the NT tissue *in vivo*. Under proper DV patterning conditions, NE cells within lumenal cysts differentiate into region-specific progenitors in discrete local domains and achieve cell fate patterning along the DV axis. Importantly, progressive development of NE cysts features sequential emergence of neural progenitor domains, with the ventral FP, P3 and pMN domains emerging progressively in discrete, non-overlapping regions and the PAX3+ dorsal territory progressively restricted to the opposite, prospective dorsal pole. The OLIG2+ pMN domain in DV patterned NE cysts can be further specified into ISLET1/2+HB9+ MNs. Our DV patterned NT development model offers great opportunities for experimental control of key parameters and quantitative measurements, providing a significantly advantageous experimental platform for advancing our understanding of the emergent self-organizing principles and patterning mechanisms that provide robustness and reliability to NT DV patterning, a long-standing question in biology.

5.2 Future work

5.2.1 Mechanobiology of in vitro human neuroectoderm development

In this dissertation, I clearly demonstrated that mechanical cues including cell shape and contractility regulates the cell fate decision during in vitro neuroectoderm development by regulating BMP-SMAD signaling. I am interested in investigating the mechano-regulation of

BMP signaling in the tissue level. YAP/TAZ is mechanosensitive transcriptional regulator that respond to mechanical cues such as extracellular matrix rigidity, cell spread area, and cytoskeletal contractility by dynamically shuttling in and out of the nucleus [163-165]. Specifically, active YAP/TAZ localizes in the nucleus of mechanosensitive adherent cells seeded on rigid substrates, whereas YAP/TAZ moves out of the nucleus and remains in the cytoplasm for cells cultured on soft substrates. In parallel, mechanosensitive adherent cells cultured on large micropatterned adhesive islands exhibit greater cytoskeletal contractile force and nuclear localization of YAP/TAZ, whereas cells confined to small adhesive islands show limited cytoskeletal contractile force and inactive YAP/TAZ retained in the cytoplasm. Importantly, neurogenic differentiation of hPSCs has been shown to be sensitive to substrate rigidity and dependent on Hippo/YAP signaling. Soft substrate promoted NE differentiation of hPSCs and cytoplasmic retention of YAP/TAZ [165, 166]. TAZ knockdown induced NE differentiation on rigid culture dish [167]. Given the prevalence of cell spreading area and contractility in regulating YAP/TAZ activity, as well as the fact that Smad nuclear/cytoplasmic shuttling and neurogenic differentiation is regulated by YAP/TAZ activity, it is worthy of studying in the future if YAP/TAZ plays a key role in regulating the mechanosensitive BMP activity in the neuroectoderm model.

5.2.2 Defined co-culture platform to study the tissue interaction in regulating neuroectoderm patterning

The NPB is located at the boundary of the neural plate and non-neural ectoderm and will give rise to future neural crest cells and placodes. Studies from model animals showed that NPB induction is through the interaction of NP/NNE or NP/mesoderm through the gradients of inductive signals such as NNE-secreted BMP and WNT and paraxial/intermediate mesoderm-

secreted FGF [116, 168]. The requirement of these signaling for NPB specification seems species-specific. For example, in chick, induction of NPB required an early activation of WNT signaling followed by later activation of BMP signaling [55]. In contrast, in *Xenopus*, WNT signals need to be inhibited for NPB induction [65].

The neuroectoderm model reported in chapter 2 leverages the autonomous self-organization properties of hPSCs to form spatially organized NP and NBP cells. Although endogenous BMP4 or NOGGIN gradients were excluded in regulating NP/NPB patterning in neuroectoderm model, it's unclear whether chemical gradients such as BMP, FGF and WNT gradients can also induce spatial patterning of cell fate during neural induction, and whether cell shape and force act downstream of biochemical gradient or work independently to determine lineage specification. It's interesting to develop a micro-engineering platform that could generate radial chemical gradients in the micropatterned colony. This can be achieved by incorporating micropatterned micro-pore array with the multi-layer microfluidic device. We can fabricate micro-pores (~ 0.2 μm diameter) in a circular micropattern (400 μm diameter) array format in a PDMS membrane, with micro-pores only in the periphery of the circular micropattern. Thus, by culturing the micropattern hPSC colony (400 μm diameter) on the membrane and align peripheral region of hPSC colony above the micro-pore, we could generate the chemical gradients in the micropatterned hPSC colony by providing the chemicals underneath the membrane. We could also modulate the mechanical environment by changing the membrane stiffness. Using such integrative platform with the capability to modulate chemical and mechanical environment, we could perform quantitative analysis of the interactions between biochemical and biomechanical cues in neural development.

To study the tissue-tissue interaction between NP and NNE, a defined co-culture platform, which could control the position of NNE and NP cells derived from hPSCs in a reproducible manner, is required. Micropatterning-based co-culture platforms by using PDMS stencils or micro-contact printing are very promising to generate such in vitro ectoderm models by precisely plating NNE cells in a concentric ring-shaped colony surrounding micropatterned neuroectoderm cells [169]. Integration of co-culture platforms with biosensors targeting intracellular chemical signaling activity could provide a strategy to map and investigate the signaling dynamics during NC induction. I envision controllable and reproducible co-culture platforms that could advance our understanding of human NPB development by dissecting tissue interactions at the molecular and signaling levels.

Recently, Toh and colleagues have reported another micropatterned ectoderm patterning model that further incorporates mesoendoderm lineages with neuroepithelial cells and displays morphogenetic events resembling NP folding (SSRN doi: 10.2139/ssrn.3231850). A short mesoendoderm induction followed by neuroectoderm induction allows hPS cells at the colony border to differentiate into mesoendoderm cells and cells at the colony center to differentiate into NE cells. Apical constriction, marked by enriched ACTIN and p-MYOSIN at apical surfaces, induces tissue folding at the colony border toward colony center. A critical role of mesoendoderm cells involving TGF-β signaling is identified for folding of micropatterned ectoderm tissues. How TGF-β signaling regulates tissue folding was not studied in this work. Although border of the micropatterned colony folded, cells at the edge of folded tissue didn't fuse together and form hollow sphere. In vertebrate, neural tube fusion involves the formation of filopodia or lamellipodia from NPB or NNE, which serves as the first attachment points during neural tube folding [4]. In this study, the tip of folded structures was T^+ mesoderm cells and no

actin-rich structures were formed in these cells. To model neural tube closure, it is interesting to co-culture our neuroectoderm model with hPSC-derived mesoderm cells and study if the NPB cells could induce neural tube folding and closure.

5.2.3 High-throughput neural teratogenicity testing system based on hPSC-derived in vitro neuroectoderm model

Birth defect is a structural defect in the body due to abnormal embryonic or fetal development, which affects one in every 33 babies in the United States[170]. As an example, neural tube defects are induced by the incidence that the neural tube fails to close by the end of first month of pregnancy and affect 300,000 births each year worldwide [171]. Though the specific causes of these birth defects are largely unknown, it is clear that the occurrence is related to genetic predisposition as well as environmental factors, including exposure to teratogenic agents especially through medications [171]. For example, thalidomide, which is a immunomodulatory drug used as treatment of certain cancers, caused about 10000 cases of malformation of limbs in 1950s due to its usage during pregnancy [172]. It is therefore necessary to have methods that can assess the toxicological safety and evaluate chemical-induced teratogenicity of chemical agents.

In addition to animal embryo models, human pluripotent stem (hPSs) cells have the potential to generate teratogenic testing models using human-derived tissues in vitro. Indeed, by leveraging hPSCs technology, Kameoka et al. reported the teratogen screening by directing the neural differentiation of hPSCs [173]. Colleoni et al. reported that the generation of neural rosettes through embryoid body can be used as a neural teratogenicity assay [174]. Neural progenitor cells have also been used by Breier et al. for teratogen screening [175]. However,

these studies simply used hPS cell differentiated neural cells, failing to mimic key structures and processes during neural development, compromising applicability of their finding to human development.

A number of transcription factors are implicated for regulating NT closure, including Pax3 and Zic genes. Pax3, which is expressed in the NPB during neural tube folding, plays a crucial role during NT closure; Pax3 mutant mouse embryos display spina bifida [176]. Several Zic family proteins such as Zic2, Zic3 and Zic5 are implicated in NT closure. Loss of function of Zic2 and Zic3 disrupts NT closure in mice, leading to variable defects [177, 178].

In the future, this neuroectoderm model with Pax6+ NE cells in the colony center and Pax3+ and ZIC1+ NPB cells in the colony periphery could be leveraged to develop a high throughput neural teratogenicity assay which can capture both biochemical and morphological changes during neuroectoderm formation in detail under potential teratogen treatment. The candidate features to examine include the expression and band width of Pax3 and Zic1. The first step is to validate the assay's efficacy to differentiate teratogenic reagents (valproic acid, thalidomide, and mianserin) and non-teratogenic reagents (penicillin G and folic acid). By collecting large amounts of data on teratogens, we could use machine learning to assess the teratogenic potential of drugs with unknown teratogenic effect.

5.2.4 Controllable modeling of dorsal-ventral patterning of human neural tube

Current in vitro DV patterned neural tube models rely on autonomous cell differentiation and spontaneous symmetry breaking in a homogenous cellular environment, so efficiency of generating DV patterned neural cysts is low and fully organized cell fate patterning of neural cysts with all domains along DV axis has not been achieved. Vertebrate neural tube DV

patterning is controlled by morphogen gradients such as BMP and SHH gradients emanating from epidermis and notochord. In ventral neural tube development, cell fate patterning is dictated by both concentration and duration of SHH exposure[77]. How these two parameters influence cell fate decision during ventral neural tube patterning remains unclear. Controllable and reproducible stem cell-based in vitro models are needed to understand how graded signaling gradient is interpreted. Microfluidics, due to its ability to generate chemical gradients in a controllable manner, can serve as ideal tools for modeling neural tube DV patterning. We have recently developed a microfluidic embryological model that recapitulates key landmarks during human post-implantation development[82]. Development of novel microfluidic devices that are capable to precisely control size and position of NE cysts and generate antiparallel BMP and SHH gradients could lead to DV patterned neural cysts in a reproducible manner. Integration of such microfluidic neural tube DV model with lineage or signaling reporter cell lines and live-cell imaging could advance our understanding of interaction of BMP and SHH gradient in determining gene expression in molecular, cellular and tissue level.

5.3 Conclusion and perspective

In the dissertation, I developed hPS cell-based, neural development models simulating neural induction and NT DV patterning. In conjunction with lineage and signaling reporter lines, these models will offer promising trackable systems to study pattern formation, morphogenesis, cell differentiation, and growth. These models are also useful for elucidating intracellular signaling dynamics and gene regulatory networks and their cross-talk with mechanotransduction during embryonic development and for studying classic developmental biology questions, such as symmetry breaking, scaling and induction. In principle, these synthetic models can be

integrated with multi-well plate formats to achieve highly parallelized assays compatible with existing automation workflows and screening infrastructure. By employing advanced bioengineering approaches to control dynamic cell-cell and cell-extracellular matrix interactions and soluble environments, new models of neural development, such as those simulating neural fold development and their fusion into the NT and AP / DV patterning of the NT, will likely emerge in the coming years. Successful development of these new models will hinge on refined understanding of the intricate interactions and interdependencies between soluble factors and insoluble biophysical signals and their roles in progressive neural development. It is also important to recognize that embryonic development is a long-term process in which dynamic changes of cell-cell and cell-extracellular matrix interactions abound. How we can generate in vitro culture environments to mimic the dynamic nature and complexity of the in vivo neurogenic niche remains a significant challenge.

The existing stem cell-based neural development models largely rely on the autonomous self-organizing property of human PS cells to form patterned multicellular structures de novo through spontaneous symmetry breaking. It can be envisioned that different bioengineering strategies can be incorporated into this emerging area to provide precise controls of different aspects of cell culture microenvironments. These bioengineering tools, which span different scales, from molecular to cellular to organ levels, allow researchers to generate dynamic culture environments, with the molecular, structural, hydrodynamic, and mechanical cues well controlled in conjunction with their spatial and temporal levels and combinations. Some of the techniques have already been successfully implemented in the examples discussed above, including microcontact printing and synthetic hydrogels. Others useful for controlling dynamic chemical signals and their gradients, intracellular signaling, and cell-cell interactions, such as

microfluidics, optogenetics, and bioengineered tissue co-culture systems, are expected to find important applications in this area, by triggering symmetry breaking and providing dynamic chemical signals to induce the development of local signaling centers critical for progressive cell fate specification and tissue patterning. Another important area we expect new discoveries from these synthetic models is the study of feedback regulation by morphogenetic cues (such as geometric confinement, cell polarity, cell shape, and cytoskeletal contractility) on classic developmental signaling pathways to promote the robustness of embryonic patterning and tissue morphogenesis during neural development.

I conclude this dissertation by discussing how advanced bioengineering tools would enable generation of new model of neural development. (1) Microfluidics. The existing models only allow temporal control of introduction of chemical factors. Microfluidics can serve as ideal tools to provide spatiotemporal control of chemical factor introduction. Development of novel microfluidic devices capable to precisely control colony position and generate morphogen gradients could lead to new models of neural development such as AP / DV patterning of NT. (2) Synthetic biomaterials. Currently, the NT in vitro models are grown in a 3D environment in Matrigel, a poorly defined animal-derived matrices, and this causes variation of the outcomes from different batches. Synthetic hydrogel with tunable ECM compositions and mechanical properties would be beneficial to provide highly controllable cellular environment. Defined hydrogel would also allow us to study the role of individual ECM components in different stages of neural development. (3) Co-culture platform. A defined co-culture platform, which could control the position of different cell types differentiated from hPS cells in a reproducible manner, is desired to study the tissue-tissue interaction during neural development. For example, co-culture of NE cells with NNE cells or mesoderm cells could answer some key questions of NC

induction such as complex signaling crosstalk between NP and NNE/mesoderm to induce NC. Micropatterning-based co-culture platforms by using PDMS stencils or micro-contact printing are very promising to generate such system by precisely controlling spatiotemporal distribution of two or more cell types [179]. (4) Colony shape control. While micropatterning have been used to control colony shape and size, it is challenging to precisely control the tissue size and shape in a 3D environment. In the future, controlling tissue size and shape by integrating 3D culture with geometrical confinement using micro-contact printing or micro-wells could generate more homogeneous NE cysts and complex in vitro tissues with different shapes such as tubular structure to model NT development.

Appendices

Appendix A

General cell biology assays

Cell culture

H1 hES cell line (WA01, WiCell; NIH registration number: 0043) was cultured on mitotically inactive mouse embryonic fibroblasts (MEFs; GlobalStem) using growth medium containing contained DMEM/F12 (GIBCO), 20% KnockOut Serum Replacement (KSR; GIBCO), 0.1 mM β-mercaptoethanol (GIBCO), 2 mM glutamax (GIBCO), 1% non-essential amino acids (GIBCO), and 4 ng mL^{-1} human recombinant basic fibroblast growth factor (bFGF; GlobalStem). Cell culture medium is replenished every day.

H1 hES cells were passaged every 5 d using the STEMPRO EZPassage Disposable Stem Cell Passaging Tool (Invitrogen). Before passaging, differentiated cells were removed manually using a modified pasteur pipette under a stereomicroscope (Olympus). Cells were rinsed briefly with PBS and treated with TrypLE Select (Invitrogen) for 2 min to release MEFs. Cells were rinsed briefly again with PBS before all cells, including hES cells and remaining MEFs, were collected using a cell scraper (BD Biosciences). To remove contaminating MEFs, all cells were transferred onto a 60-mm tissue culture dish (BD Biosciences) coated with gelatin (Sigma) and

incubated for 45 min. MEFs would attach to the dish while hES cells still remained in suspension. hES cells in suspension were collected and centrifuged, and the resulting cell pellet was re-dispersed in growth medium supplemented with Y27632 (10 μM; Enzo Life Sciences) before cell seeding. For passaging H9 hES and hiPS cells, cells were digested using TrypLE Select before cell seeding.

hESC line H9 (WA09, WiCell; NIH registration number: 0062) and 1196a hiPSC line (from the University of Michigan Pluripotent Stem Cell Core33) were cultured under a standard feeder-free condition in mTeSR1 medium (STEMCELL Technologies) with daily medium exchange. Cells were passaged every 5 d using dispase (STEMCELL Technologies) and the STEMPRO EZPassage Disposable Stem Cell Passaging Tool (Invitrogen). Cell pellets re-suspended in mTeSR1 were transferred onto a 6-well tissue culture plate (BD Biosciences) pre-coated with 1% lactate dehydrogenase-elevating virus (LDEV)-free hESC-qualified reduced growth factor basement membrane matrix Geltrex^{TM} (Thermo Fisher Scientific). All the cell lines used in this study had a passage number < P70, and it was authenticated as karyotypically normal by Cell Line Genetics. H9 hESC line was tested negative for mycoplasma contamination (LookOut Mycoplasma PCR Detection Kit, Sigma-Aldrich).

All protocols for the use of hPS cell lines have been approved by the Human Pluripotent Stem Cell Research Oversight Committee at the University of Michigan. All the cell lines used in this study had a passage number < P70 and were authenticated as karyotypically normal by Cell Line Genetics. All cell lines were tested negative for mycoplasma contamination (LookOut Mycoplasma PCR Detection Kit, Sigma-Aldrich).

Immunocytochemistry

For immunocytochemistry for 2D cell cultures, cells were fixed with 4% paraformaldehyde (Electron Microscopy Sciences) for 15 min and then permeabilized with 0.1% Triton X-100 (Roche Applied Science) for 20 min at room temperature. Primary antibodies were used and detected by goat-anti mouse Alexa Fluor 488 and/or goat-anti rabbit Alexa Fluor 546 secondary antibodies for 1 hour at room tmperature. To visualize nuclei, cells were stained with 4,6-diamidino-2- phenylindole (DAPI; Invitrogen). Samples were then labeled with goat-raised secondary antibodies (1:500) at room temperature for another hour.

For immunocytochemistry for 3D cell culture, Cystic tissues were fixed in 4% paraformaldehyde (PFA, Electron Microscopy Sciences) at room temperature for 1 h before being permeabilized with 0.1% sodium dodecyl sulfate (SDS, dissolved in PBS) solution at room temperature for 3 h. Cysts were then blocked in 10% goat serum solution (Thermo Fisher Scientific) or 4% donkey serum solution (Sigma) at 4 °C overnight. Immunostaining was performed in primary antibody solutions prepared in blocking buffer for 24 h at 4 °C. Cysts were then washed with PBS and incubated with goat or donkey-raised secondary antibodies at 4 °C for another 24 h. DAPI (Invitrogen) was used for counterstaining cell nuclei.

RNA isolation and quantitative reverse-transcription PCR (qRT-PCR) analysis

Total RNA was isolated from cells using RNeasy kit (Qiagen). Quantitative reverse-transcription PCR (qRT-PCR) was performed and monitored using a CFX Connect SYBR Green PCR Master Mix system (Bio-Rad). Human TBP primers were used as an endogenous control for relative quantifications. Samples in which no expression was detected were given an arbitrary Ct value of 40. All analyses were performed with at least 3 biological replicates and 3

technical replicates. Relative expression levels were determined by calculating $2^{-\Delta\Delta Ct}$ with the corresponding s.e.m.

Appendix B

List of primary antibodies

Table B-1 List of primary antibodies used for the immunocytochemistry

Protein	Vendor	Catalog number	Dilution
ZO-1	Invitrogen	33-9100	1:50 (ICC)
PAX6	Abcam	ab78545	1:200 (ICC)
PAX6	Covance	PRB-278P	1:500 (ICC)
PAX3	Novus	NBP1-32944	1:200 (ICC)
PAX3	R&D Systems	MAB2457-SP	1:200 (ICC)
ZIC1	Novus	NB600-488	1:200 (ICC)
MSX1	Novus	NBP2-30052	1:200 (ICC)
p- SMAD 1/5	Millipore	AB3848	1:100 (ICC)
p-MLC	Cell Signaling	3671S	1:50 (ICC)
GAPDH	Santa-Cruz Biotechnology	sc-25778	1:200 (WB)
N-CADHERIN	Abcam	ab12221	1:100 (ICC)
E-CADHERIN	BD Biosciences	610181	1:100 (ICC)
SOX10	Cell Signaling	89356S	1:100 (ICC)
AP2α	Santa-Cruz Biotechnology	sc-12726	1:100 (ICC)
SOX2	Stemgent	09-0024	1:500 (ICC)
NESTIN	Santa Cruz Biotech.	sc-23927	1:500 (ICC)

SOX1	Millipore	AB15766	1:200 (ICC)
OCT4	Santa Cruz Biotech.	sc-5279	1:200 (ICC)
OLIG2	Santa Cruz Biotech.	sc-48817	1:500 (ICC)
OLIG2	R&D Systems	AF2418-SP	1:200 (ICC)
NKX2.2	DSHB	74.5A5	1:200 (ICC)
FOXA2	Santa Cruz Biotech.	sc-101060	1:100 (ICC)
FOXA2	Seven Hills Bioreagents	WRAB-1200	1:500 (ICC)
FOXA2	R&D Systems	AF2400-SP	1:500 (ICC)
NKX6.1	DSHB	F55A12	1:200 (ICC)
ISLET1/2	Santa Cruz Biotech.	sc-30200	1:100 (ICC)
HB9	Santa Cruz Biotech.	sc-22542	1:100 (ICC)
βIII-TUBULIN	BioLegend	MRB-435P	1:1000 (ICC)
MAP2	Sigma Aldrich	M1406-.2ML	1:500 (ICC)
BRACHYURY	Santa Cruz Biotech.	sc-374321	1:50 (ICC)
SOX17	R&D System	AF1924	1:50 (ICC)
CDX2	Biogenex	MU392A-5UC	1:100 (ICC)
EOMES	Abcam	ab23345	1:100 (ICC)

Appendix C

Cell stretching assay

B1. Silicon master fabrication

1. Photolithography

1.1. Spin coat photoresist SPR220 on silicon wafer for 1 min and soft bake at 110 ℃ for 3 min using ACS 200 cluster tool.

1.2. Exposure the photoresist for 12 seconds using MA/BA-6 Mask/Bond Aligner.

1.3. Develop the photoresist using AZ 300 Developer for 40 seconds using ACS 200 cluster tool.

2. Deep reactive ion etching (DRIE)

2.1. Etch the silicon wafer with spin coated photoresist using STS Pegasus 4 for 12 min. The etching depth is around 60 μm.

2.2. Strip the residual photoresist using YES Plasma Stripper

3. Silicon master silanization

3.1. Oxygen plasma treat silicon master for 1.5 min to activate surface.

3.2. Place silicon master in a dessicator and spread 100 µl Silane (tridecafluoro- 1, 1, 2, 2,-tetrahydrooctyl)-1-trichlorosilane (Sigma Aldrich) in the dessicator.

3.3. Vacuum chamber to evaporate silane and coat silicon master with silane for 3 hours.

B2. Stretching device fabrication

The microfluidic cell stretching device was comprised of a PDMS structural layer, a PDMS inlet block, and a glass coverslip. The PDMS structural layer contained a microfluidic network for applying pressures to simultaneously activate 64 pressurization compartments to induce PDMS membrane deformation, was fabricated using soft lithography.

1. Device fabrication

1.1. PDMS prepolymer containing PDMS base monomer and curing agent (10:1 *w* / *w*) was spin coated on silicon master for 500 rpm, 30 seconds and then 900 rpm, 90 seconds. The PDMS layer was thermally cured by baking at 110 °C for at least 24 hr

1.2. before peeled off from the silicon mold. An inlet for fluid connections was then punched into the PDMS structural layer using a 1 mm biopsy punch (Fisher Scientific). Both the coverslip and PDMS structural layer were briefly cleaned with 100% ethanol (Fisher Scientific) and blown dry under nitrogen before treated with air plasma (Plasma Prep II; SPI Supplies) and bonding together.

1.3. Another PDMS block was prepared, and an inlet for fluid connection was punched into the PDMS block with a 0.5 mm biopsy punch. After both treated with air plasma, the

PDMS block and the PDMS structural layer were bonded together with their fluid inlets aligned manually.

1.4. The competed microfluidic cell stretching device was baked at 110 °C for at least another 24 hr to ensure robust bonding between different layers.

2. Microcontact printing

To apply continuous stretching to the central zone of micropatterned hPS cell colonies, microcontact printing was performed to print circular adhesive patterns with a diameter of 400 μm onto the deformable PDMS membrane on top of pressurization compartments (with a diameter of 200 μm) in a custom designed microfluidic cell stretching device. To this end, a custom desktop aligner designed for fabrication of multilayer microfluidic devices was used[133].

2.1 Vitronectin-coated PDMS stamp and the microfluidic cell stretching device were mounted onto the top and bottom layer holders of the aligner, respectively.

2.2 Under inspection with a digital microscope, the X / Y / θ stage holding the bottom layer holder was carefully adjusted for alignment of the PDMS stamp and the microfluidic cell stretching device. After alignment, the PDMS stamp was gently pressed to transfer vitronectin from the stamp to the deformable PDMS membrane on top of pressurization compartments.

B3. Cell stretching assay

Deionized water was injected into the microfluidic cell stretching device before applying pressure through a microfluidic pressure pump (AF1, Elveflow). Software (Elveflow Smart Interface) was used for programming the pressure pump for continuous cell stretching with a square-wave pattern (pulse width of 2 hr, period of 4 hr, and 50% duty cycle).

Appendix D

List of qRT-PCR primers

Table D-1 List of primers used for the qRT-PCR analysis.

Gene	Forward	Reverse
MSX1	AGGTTGAAGGGACCTCTCTCTTA	CTTCCAAAGGGATGTTTGAGAGC
ID1	CAGCCAGTCGCCAAGAAT	ACAGACAGCGCACCACCT
ID3	CTTAGCCAGGTGGAAATCCTACA	CTCGGCTGTCTGGATGGGAA
PAX3	TACAGGTCTGGTTTAGCAAC	GATCTGACACAGCTTGTGGA
SOX9	GCTCTGGAGACTTCTGAACGAGA	GAAGATGGCGTTGGGGGAGAT
TBP	TGCCCGAAACGCCGAATATAATC	GTCTGGACTGTTCTTCACTCTTGG

References

1. Solnica-Krezel, L., *Conserved patterns of cell movements during vertebrate gastrulation.* Current biology, 2005. **15**(6): p. R213-R228.
2. Ozair, M.Z., C. Kintner, and A.H. Brivanlou, *Neural induction and early patterning in vertebrates.* Wiley Interdisciplinary Reviews: Developmental Biology, 2013. **2**(4): p. 479-498.
3. Patthey, C. and L. Gunhaga, *Signaling pathways regulating ectodermal cell fate choices.* Experimental cell research, 2014. **321**(1): p. 11-16.
4. Nikolopoulou, E., et al., *Neural tube closure: cellular, molecular and biomechanical mechanisms.* Development, 2017. **144**(4): p. 552-566.
5. Jessell, T.M., *Neuronal specification in the spinal cord: inductive signals and transcriptional codes.* Nature Reviews Genetics, 2000. **1**(1): p. 20.
6. Le Dreau, G. and E. Marti, *Dorsal-ventral patterning of the neural tube: a tale of three signals.* Dev Neurobiol, 2012. **72**(12): p. 1471-81.
7. Wilson, L. and M. Maden, *The mechanisms of dorsoventral patterning in the vertebrate neural tube.* Developmental biology, 2005. **282**(1): p. 1-13.
8. Greene, N.D. and A.J. Copp, *Neural tube defects.* Annual review of neuroscience, 2014. **37**: p. 221-242.
9. Jin, Y., et al., *The relationship between autism spectrum disorder and melatonin during fetal development.* Molecules, 2018. **23**(1): p. 198.
10. Roizen, N.J. and D. Patterson, *Down's syndrome.* The Lancet, 2003. **361**(9365): p. 1281-1289.
11. Spemann, H. and H. Mangold, *Induction of embryonic primordia by implantation of organizers from a different species. 1923.* International Journal of Developmental Biology, 2003. **45**(1): p. 13-38.
12. Beddington, R., *Induction of a second neural axis by the mouse node.* Development, 1994. **120**(3): p. 613-620.
13. Storey, K.G., et al., *Neural induction and regionalisation in the chick embryo.* Development, 1992. **114**(3): p. 729-741.
14. Nieuwkoop, P.D., *Activation and organization of the central nervous system in amphibians. Part III. Synthesis of a new working hypothesis.* Journal of Experimental Zoology, 1952. **120**(1): p. 83-108.
15. Slack, J. and D. Forman, *An interaction between dorsal and ventral regions of the marginal zone in early amphibian embryos.* Development, 1980. **56**(1): p. 283-299.
16. Hemmati-Brivanlou, A. and D.A. Melton, *A truncated activin receptor inhibits mesoderm induction and formation of axial structures in Xenopus embryos.* Nature, 1992. **359**(6396): p. 609.
17. Dale, L. and C.M. Jones, *BMP signalling in early Xenopus development.* Bioessays, 1999. **21**(9): p. 751-760.

18. Hawley, S., et al., *Disruption of BMP signals in embryonic Xenopus ectoderm leads to direct neural induction.* Genes & development, 1995. **9**(23): p. 2923-2935.
19. Xu, R.-H., et al., *A dominant negative bone morphogenetic protein 4 receptor causes neuralization in Xenopus ectoderm.* Biochemical and biophysical research communications, 1995. **212**(1): p. 212-219.
20. Grunz, H. and L. Tacke, *Neural differentiation of Xenopus laevis ectoderm takes place after disaggregation and delayed reaggregation without inducer.* Cell differentiation and development, 1989. **28**(3): p. 211-217.
21. Wilson, P.A. and A. Hemmati-Brivanlou, *Induction of epidermis and inhibition of neural fate by Bmp-4.* Nature, 1995. **376**(6538): p. 331.
22. Wilson, P.A., et al., *Concentration-dependent patterning of the Xenopus ectoderm by BMP4 and its signal transducer Smad1.* Development, 1997. **124**(16): p. 3177-3184.
23. Suzuki, A., N. Ueno, and A. Hemmati-Brivanlou, *Xenopus msx1 mediates epidermal induction and neural inhibition by BMP4.* Development, 1997. **124**(16): p. 3037-3044.
24. Fainsod, A., H. Steinbeisser, and E. De Robertis, *On the function of BMP‐4 in patterning the marginal zone of the Xenopus embryo.* The EMBO Journal, 1994. **13**(21): p. 5015-5025.
25. Sasai, Y., et al., *Regulation of neural induction by the Chd and Bmp-4 antagonistic patterning signals in Xenopus.* Nature, 1995. **376**(6538): p. 333.
26. Hemmati-Brivanlou, A., O.G. Kelly, and D.A. Melton, *Follistatin, an antagonist of activin, is expressed in the Spemann organizer and displays direct neuralizing activity.* Cell, 1994. **77**(2): p. 283-295.
27. Lamb, T.M., et al., *Neural induction by the secreted polypeptide noggin.* Science, 1993. **262**(5134): p. 713-718.
28. Smith, J.L. and G.C. Schoenwolf, *Notochordal induction of cell wedging in the chick neural plate and its role in neural tube formation.* Journal of experimental zoology, 1989. **250**(1): p. 49-62.
29. Davidson, B.P., et al., *Impact of node ablation on the morphogenesis of the body axis and the lateral asymmetry of the mouse embryo during early organogenesis.* Developmental biology, 1999. **211**(1): p. 11-26.
30. Streit, A. and C.D. Stern, *Mesoderm patterning and somite formation during node regression: differential effects of chordin and noggin.* Mechanisms of development, 1999. **85**(1-2): p. 85-96.
31. Streit, A. and C.D. Stern, *Establishment and maintenance of the border of the neural plate in the chick: involvement of FGF and BMP activity.* Mechanisms of development, 1999. **82**(1-2): p. 51-66.
32. Faure, S., et al., *Endogenous patterns of BMP signaling during early chick development.* Developmental biology, 2002. **244**(1): p. 44-65.
33. Launay, C., et al., *A truncated FGF receptor blocks neural induction by endogenous Xenopus inducers.* Development, 1996. **122**(3): p. 869-880.
34. Xu, R.-H., et al., *Studies on the role of fibroblast growth factor signaling in neurogenesis using conjugated/aged animal caps and dorsal ectoderm-grafted embryos.* Journal of Neuroscience, 1997. **17**(18): p. 6892-6898.

35. Hardcastle, Z., A.D. Chalmers, and N. Papalopulu, *FGF-8 stimulates neuronal differentiation through FGFR-4a and interferes with mesoderm induction in Xenopus embryos.* Current Biology, 2000. **10**(23): p. 1511-1514.
36. Linker, C. and C.D. Stern, *Neural induction requires BMP inhibition only as a late step, and involves signals other than FGF and Wnt antagonists.* Development, 2004. **131**(22): p. 5671-5681.
37. Delaune, E., P. Lemaire, and L. Kodjabachian, *Neural induction in Xenopus requires early FGF signalling in addition to BMP inhibition.* Development, 2005. **132**(2): p. 299-310.
38. Streit, A., et al., *Initiation of neural induction by FGF signalling before gastrulation.* Nature, 2000. **406**(6791): p. 74.
39. Wilson, S.I., et al., *An early requirement for FGF signalling in the acquisition of neural cell fate in the chick embryo.* Current Biology, 2000. **10**(8): p. 421-429.
40. Pera, E.M., et al., *Integration of IGF, FGF, and anti-BMP signals via Smad1 phosphorylation in neural induction.* Genes & development, 2003. **17**(24): p. 3023-3028.
41. Wilson, S., et al., *The status of Wnt signalling regulates neural and epidermal fates in the chick embryo.* Nature, 2001. **411**(6835): p. 325.
42. Puelles, L., et al., *Correlation of a chicken stage 4 neural plate fate map with early gene expression patterns.* Brain research reviews, 2005. **49**(2): p. 167-178.
43. Le Douarin, N., N.M. LeDouarin, and C. Kalcheim, *The neural crest*. 1999: Cambridge university press.
44. Thomas, S., et al., *Human neural crest cells display molecular and phenotypic hallmarks of stem cells.* Human molecular genetics, 2008. **17**(21): p. 3411-3425.
45. Betters, E., et al., *Analysis of early human neural crest development.* Developmental biology, 2010. **344**(2): p. 578-592.
46. Goulding, M., et al., *Pax‐3, a novel murine DNA binding protein expressed during early neurogenesis.* The EMBO journal, 1991. **10**(5): p. 1135-1147.
47. Jostes, B., C. Walther, and P. Gruss, *The murine paired box gene, Pax7, is expressed specifically during the development of the nervous and muscular system.* Mechanisms of development, 1990. **33**(1): p. 27-37.
48. Hill, R.E., et al., *A new family of mouse homeo box-containing genes: molecular structure, chromosomal location, and developmental expression of Hox-7.1.* Genes & Development, 1989. **3**(1): p. 26-37.
49. Mancilla, A. and R. Mayor, *Neural Crest Formation inXenopus laevis: Mechanisms ofXslugInduction.* Developmental biology, 1996. **177**(2): p. 580-589.
50. Selleck, M. and M. Bronner-Fraser, *Origins of the avian neural crest: the role of neural plate-epidermal interactions.* Development, 1995. **121**(2): p. 525-538.
51. Bonstein, L., S. Elias, and D. Frank, *Paraxial-Fated Mesoderm Is Required for Neural Crest Induction inXenopusEmbryos.* Developmental biology, 1998. **193**(2): p. 156-168.
52. Marchant, L., et al., *The inductive properties of mesoderm suggest that the neural crest cells are specified by a BMP gradient.* Developmental biology, 1998. **198**(2): p. 319-329.
53. Monsoro-Burq, A.-H., R.B. Fletcher, and R.M. Harland, *Neural crest induction by paraxial mesoderm in Xenopus embryos requires FGF signals.* Development, 2003. **130**(14): p. 3111-3124.

54. Basch, M.L., M. Bronner-Fraser, and M.I. García-Castro, *Specification of the neural crest occurs during gastrulation and requires Pax7.* Nature, 2006. **441**(7090): p. 218.
55. Patthey, C., T. Edlund, and L. Gunhaga, *Wnt-regulated temporal control of BMP exposure directs the choice between neural plate border and epidermal fate.* Development, 2009. **136**(1): p. 73-83.
56. Patthey, C., L. Gunhaga, and T. Edlund, *Early development of the central and peripheral nervous systems is coordinated by Wnt and BMP signals.* PLoS One, 2008. **3**(2): p. e1625.
57. Faure, S., et al., *Endogenous patterns of TGFbeta superfamily signaling during early Xenopus development.* Development, 2000. **127**(13): p. 2917-2931.
58. Nguyen, V.H., et al., *Ventral and lateral regions of the zebrafish gastrula, including the neural crest progenitors, are established by abmp2b/swirlPathway of genes.* Developmental biology, 1998. **199**(1): p. 93-110.
59. Tríbulo, C., et al., *Regulation of Msx genes by a Bmp gradient is essential for neural crest specification.* Development, 2003. **130**(26): p. 6441-6452.
60. Tucker, J.A., K.A. Mintzer, and M.C. Mullins, *The BMP signaling gradient patterns dorsoventral tissues in a temporally progressive manner along the anteroposterior axis.* Developmental cell, 2008. **14**(1): p. 108-119.
61. LaBonne, C. and M. Bronner-Fraser, *Neural crest induction in Xenopus: evidence for a two-signal model.* Development, 1998. **125**(13): p. 2403-2414.
62. Hong, C.-S., B.-Y. Park, and J.-P. Saint-Jeannet, *Fgf8a induces neural crest indirectly through the activation of Wnt8 in the paraxial mesoderm.* Development, 2008. **135**(23): p. 3903-3910.
63. Monsoro-Burq, A.-H., E. Wang, and R. Harland, *Msx1 and Pax3 cooperate to mediate FGF8 and WNT signals during Xenopus neural crest induction.* Developmental cell, 2005. **8**(2): p. 167-178.
64. Logan, C.Y. and R. Nusse, *The Wnt signaling pathway in development and disease.* Annu. Rev. Cell Dev. Biol., 2004. **20**: p. 781-810.
65. Steventon, B. and R. Mayor, *Early neural crest induction requires an initial inhibition of Wnt signals.* Developmental biology, 2012. **365**(1): p. 196-207.
66. Stuhlmiller, T.J. and M.I. García-Castro, *FGF/MAPK signaling is required in the gastrula epiblast for avian neural crest induction.* Development, 2012. **139**(2): p. 289-300.
67. Dessaud, E., A.P. McMahon, and J. Briscoe, *Pattern formation in the vertebrate neural tube: a sonic hedgehog morphogen-regulated transcriptional network.* Development, 2008. **135**(15): p. 2489-2503.
68. Liem Jr, K.F., et al., *Dorsal differentiation of neural plate cells induced by BMP-mediated signals from epidermal ectoderm.* Cell, 1995. **82**(6): p. 969-979.
69. Lyons, K.M., B.L. Hogan, and E.J. Robertson, *Colocalization of BMP 7 and BMP 2 RNAs suggests that these factors cooperatively mediate tissue interactions during murine development.* Mechanisms of development, 1995. **50**(1): p. 71-83.
70. Lee, K.J., P. Dietrich, and T.M. Jessell, *Genetic ablation reveals that the roof plate is essential for dorsal interneuron specification.* Nature, 2000. **403**(6771): p. 734.
71. Liem Jr, K.F., G. Tremml, and T.M. Jessell, *A role for the roof plate and its resident TGFβ-related proteins in neuronal patterning in the dorsal spinal cord.* Cell, 1997. **91**(1): p. 127-138.

72. Timmer, J.R., C. Wang, and L. Niswander, *BMP signaling patterns the dorsal and intermediate neural tube via regulation of homeobox and helix-loop-helix transcription factors.* Development, 2002. **129**(10): p. 2459-2472.
73. Jeong, J. and A.P. McMahon, *Growth and pattern of the mammalian neural tube are governed by partially overlapping feedback activities of the hedgehog antagonists patched 1 and Hhip1.* Development, 2005. **132**(1): p. 143-154.
74. Ribes, V. and J. Briscoe, *Establishing and interpreting graded Sonic Hedgehog signaling during vertebrate neural tube patterning: the role of negative feedback.* Cold Spring Harbor perspectives in biology, 2009. **1**(2): p. a002014.
75. Stamataki, D., et al., *A gradient of Gli activity mediates graded Sonic Hedgehog signaling in the neural tube.* Genes & development, 2005. **19**(5): p. 626-641.
76. Lei, Q., et al., *Transduction of graded Hedgehog signaling by a combination of Gli2 and Gli3 activator functions in the developing spinal cord.* Development, 2004. **131**(15): p. 3593-3604.
77. Dessaud, E., et al., *Interpretation of the sonic hedgehog morphogen gradient by a temporal adaptation mechanism.* Nature, 2007. **450**(7170): p. 717-20.
78. Nakano, T., et al., *Self-formation of optic cups and storable stratified neural retina from human ESCs.* Cell stem cell, 2012. **10**(6): p. 771-785.
79. Lancaster, M.A., et al., *Cerebral organoids model human brain development and microcephaly.* Nature, 2013. **501**(7467): p. 373.
80. Warmflash, A., et al., *A method to recapitulate early embryonic spatial patterning in human embryonic stem cells.* Nature methods, 2014. **11**(8): p. 847.
81. Shao, Y., et al., *A pluripotent stem cell-based model for post-implantation human amniotic sac development.* Nature Communications, 2017. **8**(1): p. 208.
82. Zheng, Y., et al., *Controlled modelling of human epiblast and amnion development using stem cells.* Nature, 2019. **573**(7774): p. 421-425.
83. Tao, Y. and S.-C. Zhang, *Neural subtype specification from human pluripotent stem cells.* Cell stem cell, 2016. **19**(5): p. 573-586.
84. Karzbrun, E., et al., *Human brain organoids on a chip reveal the physics of folding.* Nature physics, 2018. **14**(5): p. 515.
85. Qian, X., H. Song, and G.-l. Ming, *Brain organoids: advances, applications and challenges.* Development, 2019. **146**(8): p. dev166074.
86. Eiraku, M., et al., *Self-organized formation of polarized cortical tissues from ESCs and its active manipulation by extrinsic signals.* Cell stem cell, 2008. **3**(5): p. 519-532.
87. Qian, X., et al., *Brain-region-specific organoids using mini-bioreactors for modeling ZIKV exposure.* Cell, 2016. **165**(5): p. 1238-1254.
88. Meinhardt, A., et al., *3D reconstitution of the patterned neural tube from embryonic stem cells.* Stem cell reports, 2014. **3**(6): p. 987-999.
89. Ranga, A., et al., *Neural tube morphogenesis in synthetic 3D microenvironments.* Proceedings of the National Academy of Sciences, 2016. **113**(44): p. E6831-E6839.
90. Ogura, T., et al., *Three-dimensional induction of dorsal, intermediate and ventral spinal cord tissues from human pluripotent stem cells.* Development, 2018. **145**(16): p. dev162214.
91. Muguruma, K., et al., *Self-organization of polarized cerebellar tissue in 3D culture of human pluripotent stem cells.* Cell reports, 2015. **10**(4): p. 537-550.

92. Sakaguchi, H., et al., *Generation of functional hippocampal neurons from self-organizing human embryonic stem cell-derived dorsomedial telencephalic tissue.* Nature communications, 2015. **6**: p. 8896.
93. Xue, X., et al., *Mechanics-guided embryonic patterning of neuroectoderm tissue from human pluripotent stem cells.* Nature materials, 2018. **17**: p. 633-641.
94. Vijayraghavan, D.S. and L.A. Davidson, *Mechanics of neurulation: From classical to current perspectives on the physical mechanics that shape, fold, and form the neural tube.* Birth Defects Research, 2017. **109**(2): p. 153-168.
95. Munoz-Sanjuan, I. and A.H. Brivanlou, *Neural induction, the default model and embryonic stem cells.* Nature Reviews Neuroscience, 2002. **3**(4): p. 271-280.
96. Liu, A. and L.A. Niswander, *Bone morphogenetic protein signalling and vertebrate nervous system development.* Nature Reviews Neuroscience, 2005. **6**(12): p. 945.
97. Britton, G., et al., *A novel self-organizing embryonic stem cell system reveals signaling logic underlying the patterning of human ectoderm.* bioRxiv, 2019: p. 518803.
98. Haremaki, T., et al., *Self-organizing neuruloids model developmental aspects of Huntington's disease in the ectodermal compartment.* Nature biotechnology, 2019. **37**(10): p. 1198-1208.
99. Martyn, I., A.H. Brivanlou, and E.D. Siggia, *A wave of WNT signaling balanced by secreted inhibitors controls primitive streak formation in micropattern colonies of human embryonic stem cells.* Development, 2019. **146**(6): p. dev172791.
100. Martyn, I., et al., *Self-organization of a human organizer by combined Wnt and Nodal signalling.* Nature, 2018. **558**(7708): p. 132.
101. Tewary, M., et al., *High-throughput micropatterning platform reveals Nodal-dependent bisection of peri-gastrulation–associated versus preneurulation-associated fate patterning.* PLoS biology, 2019. **17**(10).
102. Tewary, M., et al., *A stepwise model of reaction-diffusion and positional information governs self-organized human peri-gastrulation-like patterning.* Development, 2017. **144**(23): p. 4298-4312.
103. Villa-Diaz, L.G., et al., *Synthetic polymer coatings for long-term growth of human embryonic stem cells.* Nature biotechnology, 2010. **28**(6): p. 581.
104. Villa-Diaz, L.G., et al., *Synthetic polymer coatings for long-term growth of human embryonic stem cells.* Nature Biotechnology, 2010. **28**(6): p. 581-583.
105. Fu, J.P., et al., *Mechanical regulation of cell function with geometrically modulated elastomeric substrates.* Nature Methods, 2010. **7**(9): p. 733-736.
106. Braam, S.R., et al., *Recombinant vitronectin is a functionally defined substrate that supports human embryonic stem cell self-renewal via αVβ5 integrin.* Stem Cells, 2008. **26**(9): p. 2257-2265.
107. Chambers, S.M., et al., *Highly efficient neural conversion of human ES and iPS cells by dual inhibition of Smad signaling.* Nat. Biotechnol., 2009. **27**(3): p. 275-280.
108. Mica, Y., et al., *Modeling neural crest induction, melanocyte specification, and disease-related pigmentation defects in hESCs and patient-specific iPSCs.* Cell reports, 2013. **3**(4): p. 1140-1152.
109. Tchieu, J., et al., *A modular platform for differentiation of human PSCs into all major ectodermal lineages.* Cell Stem Cell, 2017. **21**(3): p. 399-410.

110. Schroeder, T.E., *Neurulation in Xenopus laevis. An analysis and model based upon light and electron microscopy.* Journal of Embryology and Experimental Morphology, 1970. **23**(2): p. 427-462.
111. Hong, C.S. and J.P. Saint-Jeannet, *The activity of Pax3 and Zic1 regulates three distinct cell fates at the neural plate border.* Molecular Biology of the Cell, 2007. **18**(6): p. 2192-2202.
112. Sun, Y., et al., *Hippo/YAP-mediated rigidity-dependent motor neuron differentiation of human pluripotent stem cells.* Nature Materials, 2014. **13**(6): p. 599-604.
113. Ma, Z., et al., *Self-organizing human cardiac microchambers mediated by geometric confinement.* Nature Communications, 2015. **6**: p. 7413.
114. Sauka-Spengler, T. and M. Bronner-Fraser, *A gene regulatory network orchestrates neural crest formation.* Nature Reviews Molecular Cell Biology, 2008. **9**(7): p. 557-568.
115. Walther, C. and P. Gruss, *PAX-6, a murine paired box gene, is expressed in the developing CNS.* Development, 1991. **113**(4): p. 1435-1449.
116. Milet, C. and A.H. Monsoro-Burq, *Neural crest induction at the neural plate border in vertebrates.* Developmental Biology, 2012. **366**(1): p. 22-33.
117. Stern, C.D., *Neural induction: Old problem, new findings, yet more questions.* Development, 2005. **132**(9): p. 2007-2021.
118. Bier, E. and E.M. De Robertis, *BMP gradients: A paradigm for morphogen-mediated developmental patterning.* Science, 2015. **348**(6242).
119. Moury, J.D. and G.C. Schoenwolf, *Cooperative model of epithelial shaping and bending during avian neurulation: autonomous movements of the neural plate, autonomous movements of the epidermis, and interactions in the neural plate/epidermis transition zone.* Developmental Dynamics, 1995. **204**(3): p. 323-37.
120. Wozniak, M.A. and C.S. Chen, *Mechanotransduction in development: A growing role for contractility.* Nature Reviews Molecular Cell Biology, 2009. **10**(1): p. 34-43.
121. Keller, R., *Physical biology returns to morphogenesis.* Science, 2012. **338**(6104): p. 201-203.
122. Heller, E. and E. Fuchs, *Tissue patterning and cellular mechanics.* Journal of Cell Biology, 2015. **211**(2): p. 219-231.
123. Chan, C.J., C.-P. Heisenberg, and T. Hiiragi, *Coordination of morphogenesis and cell-fate specification in development.* Current Biology, 2017. **27**(18): p. R1024-R1035.
124. Gilmour, D., M. Rembold, and M. Leptin, *From morphogen to morphogenesis and back.* Nature, 2017. **541**(7637): p. 311-320.
125. Lecuit, T. and P.-F. Lenne, *Cell surface mechanics and the control of cell shape, tissue patterns and morphogenesis.* Nature reviews Molecular cell biology, 2007. **8**(8): p. 633.
126. Hiramatsu, R., et al., *External mechanical cues trigger the establishment of the anterior-posterior axis in early mouse embryos.* Developmental cell, 2013. **27**(2): p. 131-144.
127. Chien, Y.-H., et al., *Mechanical strain determines cilia length, motility, and planar position in the left-right organizer.* Developmental cell, 2018. **45**(3): p. 316-330. e4.
128. Shao, Y., et al., *Self-organized amniogenesis by human pluripotent stem cells in a biomimetic implantation-like niche.* Nature Materials, 2017. **16**(4): p. 419-+.
129. Vianello, S. and M.P. Lutolf, *Understanding the mechanobiology of early mammalian development through bioengineered models.* Developmental cell, 2019. **48**(6): p. 751-763.

130. Walter Jr, J.H., L.R. Goss, and A.T. Lazzara, *Amniotic band syndrome.* The Journal of foot and ankle surgery, 1998. **37**(4): p. 325-333.
131. Colas, J.-F. and G.C. Schoenwolf, *Towards a cellular and molecular understanding of neurulation.* Developmental Dynamics, 2001. **221**(2): p. 117-145.
132. Weng, S., et al., *Mechanosensitive subcellular rheostasis drives emergent single-cell mechanical homeostasis.* Nat Mater, 2016.
133. Li, X., et al., *Desktop aligner for fabrication of multilayer microfluidic devices.* Review of Scientific Instruments, 2015. **86**(7): p. 075008.
134. Michielin, F., et al., *Microfluidic-assisted cyclic mechanical stimulation affects cellular membrane integrity in a human muscular dystrophy in vitro model.* RSC Advances, 2015. **5**(119): p. 98429-98439.
135. Xu, R.-H., et al., *Basic FGF and suppression of BMP signaling sustain undifferentiated proliferation of human ES cells.* Nature Methods, 2005. **2**: p. 185-190.
136. Lippmann, E.S., M.C. Estevez-Silva, and R.S. Ashton, *Defined human pluripotent stem cell culture enables highly efficient neuroepithelium derivation without small molecule inhibitors.* Stem Cells, 2014. **32**(4): p. 1032-1042.
137. Warmflash, A., et al., *A method to recapitulate early embryonic spatial patterning in human embryonic stem cells.* Nature Methods, 2014. **11**(8): p. 847-854.
138. Etoc, F., et al., *A balance between secreted inhibitors and edge sensing controls gastruloid self-organization.* Developmental Cell, 2016. **39**(3): p. 302-315.
139. Tewary, M., et al., *A stepwise model of reaction-diffusion and positional-information governs self-organized human peri-gastrulation-like patterning.* Development, 2017. **144**: p. 4298-4312.
140. Nallet-Staub, F., et al., *Cell density sensing alters TGF-β signaling in a cell-type-specific manner, independent from Hippo pathway activation.* Developmental Cell, 2015. **32**(5): p. 640-651.
141. Zheng, Y., et al., *Dorsal-ventral patterned neural cyst from human pluripotent stem cells in a neurogenic niche.* Science Advances, 2019. **5**(12): p. eaax5933.
142. Briscoe, J. and S. Small, *Morphogen rules: Design principles of gradient-mediated embryo patterning.* Development, 2015. **142**(23): p. 3996-4009.
143. Juriloff, D.M. and M.J. Harris, *Mouse models for neural tube closure defects.* Hum Mol Genet, 2000. **9**(6): p. 993-1000.
144. Xue, X., et al., *Mechanics-guided embryonic patterning of neuroectoderm tissue from human pluripotent stem cells.* Nature Materials, 2018. **17**: p. 633-641.
145. Itsykson, P., et al., *Derivation of neural precursors from human embryonic stem cells in the presence of noggin.* Mol Cell Neurosci, 2005. **30**(1): p. 24-36.
146. Lancaster, M.A., et al., *Cerebral organoids model human brain development and microcephaly.* Nature, 2013. **501**(7467): p. 373-9.
147. Meinhardt, A., et al., *3D reconstitution of the patterned neural tube from embryonic stem cells.* Stem Cell Reports, 2014. **3**(6): p. 987-999.
148. Ranga, A., et al., *Neural tube morphogenesis in synthetic 3D microenvironments.* Proc Natl Acad Sci U S A, 2016. **113**(44): p. E6831-E6839.
149. Ogura, T., et al., *Three-dimensional induction of dorsal, intermediate and ventral spinal cord tissues from human pluripotent stem cells.* Development, 2018. **145**(16).

150. Paridaen, J.T. and W.B. Huttner, *Neurogenesis during development of the vertebrate central nervous system.* EMBO Rep, 2014. **15**(4): p. 351-64.
151. Sun, Y., et al., *Hippo/YAP-mediated rigidity-dependent motor neuron differentiation of human pluripotent stem cells.* Nat Mater, 2014. **13**(6): p. 599-604.
152. Chambers, S.M., et al., *Highly efficient neural conversion of human ES and iPS cells by dual inhibition of SMAD signaling.* Nature Biotechnology, 2009. **27**(3): p. 275-80.
153. Briscoe, J., et al., *A homeodomain protein code specifies progenitor cell identity and neuronal fate in the ventral neural tube.* Cell, 2000. **101**(4): p. 435-445.
154. Faravelli, I., et al., *Motor neuron derivation from human embryonic and induced pluripotent stem cells: experimental approaches and clinical perspectives.* Stem Cell Research & Therapy, 2014. **5**.
155. Minichiello, L. and R. Klein, *TrkB and TrkC neurotrophin receptors cooperate in promoting survival of hippocampal and cerebellar granule neurons.* Genes & Development, 1996. **10**(22): p. 2849-2858.
156. Schaller, S., et al., *Novel combinatorial screening identifies neurotrophic factors for selective classes of motor neurons.* Proceedings of the National Academy of Sciences, 2017. **114**(12): p. E2486-E2493.
157. Bardy, C., et al., *Neuronal medium that supports basic synaptic functions and activity of human neurons in vitro.* Proceedings of the National Academy of Sciences of the United States of America, 2015. **112**(25): p. E3312-E3312.
158. Cortes, D., et al., *Transgenic GDNF positively influences proliferation, differentiation, maturation and survival of motor neurons produced from mouse embryonic stem cells.* Frontiers in Cellular Neuroscience, 2016. **10**.
159. Kiecker, C. and A. Lumsden, *The role of organizers in patterning the nervous system.* Annu Rev Neurosci, 2012. **35**: p. 347-67.
160. Taniguchi, K., et al., *Lumen formation is an intrinsic property of isolated human pluripotent stem cells.* Stem Cell Reports, 2015. **5**(6): p. 954-962.
161. Harfe, B.D., et al., *Evidence for an expansion-based temporal Shh gradient in specifying vertebrate digit identities.* Cell, 2004. **118**(4): p. 517-528.
162. Balaskas, N., et al., *Gene regulatory logic for reading the Sonic Hedgehog signaling gradient in the vertebrate neural tube.* Cell, 2012. **148**(1-2): p. 273-84.
163. Dupont, S., et al., *Role of YAP/TAZ in mechanotransduction.* Nature, 2011. **474**(7350): p. 179-183.
164. Halder, G., S. Dupont, and S. Piccolo, *Transduction of mechanical and cytoskeletal cues by YAP and TAZ.* Nature reviews Molecular cell biology, 2012. **13**(9): p. 591-600.
165. Sun, Y., et al., *Hippo/YAP-mediated rigidity-dependent motor neuron differentiation of human pluripotent stem cells.* Nature materials, 2014. **13**(6): p. 599.
166. Musah, S., et al., *Substratum-induced differentiation of human pluripotent stem cells reveals the coactivator YAP is a potent regulator of neuronal specification.* Proceedings of the National Academy of Sciences, 2014. **111**(38): p. 13805-13810.
167. Varelas, X., et al., *TAZ controls Smad nucleocytoplasmic shuttling and regulates human embryonic stem-cell self-renewal.* Nature cell biology, 2008. **10**(7): p. 837.
168. Sakai, D. and Y. Wakamatsu, *Regulatory mechanisms for neural crest formation.* Cells Tissues Organs, 2005. **179**(1-2): p. 24-35.

169. Kaji, H., et al., *Engineering systems for the generation of patterned co-cultures for controlling cell-cell interactions.* Biochim Biophys Acta, 2011. **1810**(3): p. 239-50.
170. Control, C.f.D. and Prevention, *Update on overall prevalence of major birth defects--Atlanta, Georgia, 1978-2005.* MMWR. Morbidity and mortality weekly report, 2008. **57**(1): p. 1.
171. Christianson, A., C.P. Howson, and B. Modell, *March of Dimes: global report on birth defects, the hidden toll of dying and disabled children.* March of Dimes: global report on birth defects, the hidden toll of dying and disabled children., 2005.
172. Kim, J.H. and A.R. Scialli, *Thalidomide: the tragedy of birth defects and the effective treatment of disease.* Toxicological Sciences, 2011. **122**(1): p. 1-6.
173. Kameoka, S., et al., *A high-throughput screen for teratogens using human pluripotent stem cells.* toxicological sciences, 2013. **137**(1): p. 76-90.
174. Colleoni, S., et al., *Characterisation of a neural teratogenicity assay based on human ESCs differentiation following exposure to valproic acid.* Current medicinal chemistry, 2012. **19**(35): p. 6065-6071.
175. Breier, J.M., et al., *Development of a high-throughput screening assay for chemical effects on proliferation and viability of immortalized human neural progenitor cells.* Toxicological Sciences, 2008. **105**(1): p. 119-133.
176. Epstein, D.J., M. Vekemans, and P. Gros, *Splotch (Sp2H), a mutation affecting development of the mouse neural tube, shows a deletion within the paired homeodomain of Pax-3.* Cell, 1991. **67**(4): p. 767-774.
177. Carrel, T., et al., *The X-linked mouse mutation Bent tail is associated with a deletion of the Zic3 locus.* Human molecular genetics, 2000. **9**(13): p. 1937-1942.
178. Inoue, T., et al., *Mouse Zic5 deficiency results in neural tube defects and hypoplasia of cephalic neural crest derivatives.* Developmental biology, 2004. **270**(1): p. 146-162.
179. Kaji, H., et al., *Engineering systems for the generation of patterned co-cultures for controlling cell–cell interactions.* Biochimica et Biophysica Acta (BBA)-General Subjects, 2011. **1810**(3): p. 239-250.